

See discussions, stats, and author profiles for this publication at: <https://www.researchgate.net/publication/325987746>

On the light-activation of copper impurities in crystalline silicon: root cause analysis and applications for high-resolution imaging

Thesis · June 2018

CITATIONS

0

READS

71

1 author:



Alessandro Inglese

Broadcom Corporation

13 PUBLICATIONS 58 CITATIONS

[SEE PROFILE](#)

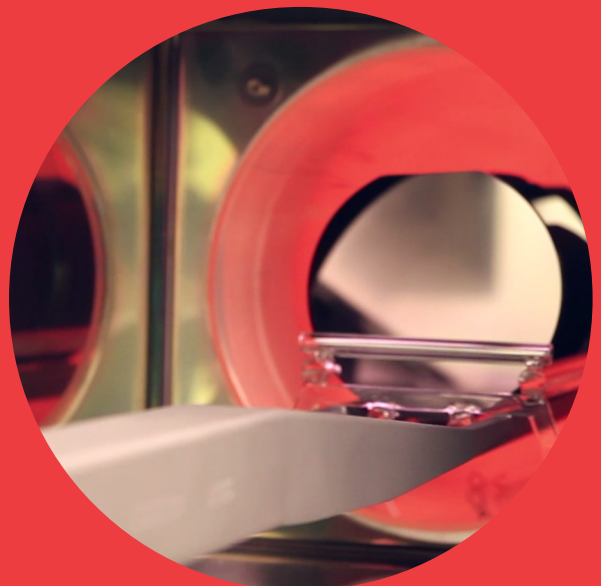
Some of the authors of this publication are also working on these related projects:



SolarX [View project](#)

On the light-activation of copper impurities in crystalline silicon: root cause analysis and applications for fast high-resolution imaging

Alessandro Inglese



A” Aalto University

DOCTORAL
DISSERTATIONS

On the light-activation of copper impurities in crystalline silicon: root cause analysis and applications for fast high-resolution imaging

Alessandro Inglese

A doctoral dissertation completed for the degree of Doctor of Science (Technology) to be defended, with the permission of the Aalto University School of Electrical Engineering, at a public examination held at the lecture hall AS1 of the school on 27th June 2018 at 12 noon.

Aalto University
School of Electrical Engineering
Department of Electronics and Nanoengineering
Electron Physics Group

Supervising professor

Prof. Hele Savin, Aalto University, Finland

Preliminary examiners

Dr. Ziv Hameiri, University of New South Wales, Australia

Dr. Stefan Rein, Fraunhofer ISE, Germany

Opponent

Dr. Ronald A.Sinton, Sinton Instruments Inc., USA

Aalto University publication series
DOCTORAL DISSERTATIONS 116/2018

© 2018 Alessandro Inglese

ISBN 978-952-60-8041-3 (printed)

ISBN 978-952-60-8042-0 (pdf)

ISSN 1799-4934 (printed)

ISSN 1799-4942 (pdf)

<http://urn.fi/URN:ISBN:978-952-60-8042-0>

Unigrafia Oy

Helsinki 2018

Finland

Publication orders (printed book):

alessandro.inglese@aalto.fi



441 697
Printed matter

Author

Alessandro Inglese

Name of the doctoral dissertation

On the light-activation of copper impurities in crystalline silicon: root cause analysis and applications for fast high-resolution imaging

Publisher School of Electrical Engineering**Unit** Department of Electronics and Nanoengineering**Series** Aalto University publication series DOCTORAL DISSERTATIONS 116/2018**Field of research** Semiconductor Technology**Manuscript submitted** 15 March 2018**Date of the defence** 27 June 2018**Permission to publish granted (date)** 21 May 2018**Language** English **Monograph** **Article dissertation** **Essay dissertation****Abstract**

In silicon-based devices copper (Cu) contamination is the cause of a variety of adverse effects, one of them being the so-called light-induced degradation (Cu-LID). This phenomenon results in the progressive reduction of minority carrier lifetime during light-soaking, thus becoming a particular issue in devices sensitive to this parameter, such as state-of-the-art silicon solar cells. The content of this dissertation elucidates various aspects of Cu-LID that have long remained unclear and examines the possibility of leveraging this knowledge to quantitatively detect copper impurities from carrier lifetime measurements.

First, experiments carried out on specimens featuring lightly doped phosphorus emitters provide insights into the effect of gettering on the strength of Cu-LID. It is found that in specimens with a phosphorus-diffused emitter significant suppression of Cu-LID is achievable through the addition of a slow cooling tail after high-temperature anneals. On the other hand, in another batch of differently processed specimens none of the tested gettering schemes results in the suppression of Cu-LID. Further investigations into this latter set of specimens indicate oxygen precipitation as the cause for the ineffectiveness of the gettering treatments.

The fact that relevant quantities of Cu may persist in the bulk region after phosphorus gettering treatments raises the need for deeper understanding into the mechanisms causing Cu-LID and development of fast and contactless methods for quickly detecting copper impurities in silicon substrates. In this dissertation, multiple evidence towards bulk Cu precipitation being the root-cause of Cu-LID is provided via (i) defect characterization based on the Shockley-Read-Hall theory, (ii) analysis of the experimental data in terms of a Schottky recombination model that specifically describes the effect of metallic precipitates on the carrier lifetime, (iii) modelling of the light-induced precipitation process and comparison of the simulation results with the existing experimental data. These findings also constitute the theoretical framework for the formulation of an imaging method that provides quantitative and spatially-resolved information on the distribution of Cu species across the silicon wafer. Such method relies on the acceleration of the degradation process through simultaneous illumination and low-temperature annealing and subsequent comparison of lifetime data with the values predicted by the aforementioned Schottky model. Examples of application of this approach to deliberately contaminated mono- and multicrystalline specimens are also discussed.

Keywords silicon, copper, light-induced degradation, gettering, defect characterization, imaging**ISBN (printed)** 978-952-60-8041-3**ISBN (pdf)** 978-952-60-8042-0**ISSN (printed)** 1799-4934**ISSN (pdf)** 1799-4942**Location of publisher** Helsinki**Location of printing** Helsinki**Year** 2018**Pages** 149**urn** <http://urn.fi/URN:ISBN:978-952-60-8042-0>

Preface

The research documented in this thesis was carried out at the Department of Electronics and Nanoengineering (formerly Department of Micro- and Nanosciences) between January 2014 and December 2017.

My deepest gratitude goes to my family, my dad (Riccardo), mum (Francesca) and sister (Arianna), who supported, encouraged and guided me throughout my studies. Without them this important milestone of my life would still be far ahead.

I wish to thank my co-authors for the precious support that they provided during manuscript preparations and reviews. In particular, I would like to acknowledge the help that I received from my colleague Dr. Henri Vahlman for the insightful discussions we had during coffee breaks. I am also grateful to Dr. Martin Schubert, Dr. Jonas Schön and Dr. Florian Schindler for their invaluable support during my short, yet extremely instructive, research visit at Fraunhofer ISE. I also wish to thank Dr. Tim Niewelt for the help with temperature-dependent lifetime measurements.

I am grateful to the members of the Electron Physics Group for the help they have all provided during the execution of this doctoral research. Particularly I am indebted to Dr. Antti Haarahiltunen for the invaluable inheritance we received from his previous research work, Dr. Ville Vähäniemi and Dr. Hannu Laine for their crucial advice with cleanroom work and all issues related to sample preparation.

Finally, I would like to acknowledge my supervisor Prof. Hele Savin for giving me the opportunity to live, work and professionally grow in this "exotic" country.

I am also grateful to Dr. Ronald A. Sinton (Sinton Instruments LLC) for accepting the invitation to act as opponent for this doctoral dissertation, to Dr. Stefan Rein (Fraunhofer ISE, Germany) and Dr. Ziv Hameiri (Univer-

sity of New South Wales, Australia) for pre-examining its content.

This thesis work has been completed thanks to the generous financial support from the Aalto ELEC doctoral school, which provided a large part of the budget, the Alfred Kordelin foundation, the European Research Council (ERC) and all industrial partners that also provided materials, technical support and advisory (SolarWorld Innovations GmbH, Okmetic Oyj, Topsil A/S, Fortum Oyj, Beneq Oy).

Regensburg, May 22, 2018,

Alessandro Inglese

Contents

Preface	v
Contents	vii
List of Publications	xi
Author's Contribution	xiii
1. Introduction	1
1.1 Background and research context	1
1.2 Research questions	2
1.3 Structure of this dissertation	3
2. Charge carrier recombination	5
2.1 Carrier generation, recombination and lifetime	5
2.2 Radiative recombination	6
2.3 Auger recombination	6
2.4 Shockley-Read-Hall (SRH) recombination	7
2.4.1 Influence of defect parameters on SRH recombination	8
2.4.2 Defect classification based on SRH parameters	10
2.5 Carrier recombination at extended defects	10
2.5.1 The Schottky model	11
2.5.2 Influence of doping and precipitate size/density on the recombination activity	13
2.6 Surface recombination	14
2.7 Calculation of the effective carrier lifetime	16
3. Copper in Silicon	17
3.1 Physical properties	17
3.1.1 Diffusivity	17

3.1.2 Solubility	18
3.2 Copper complexes and recombination activity	19
3.3 Copper-related light-induced degradation (Cu-LID)	21
4. Experimental methods for carrier lifetime measurements	25
4.1 Quasi-steady state photoconductance (QSSPC)	25
4.2 Microwave-photoconductance decay (μ -PCD)	28
4.3 Photoluminescence imaging (PL-I)	29
4.4 Surface photovoltaic (SPV)	32
5. Gettering of Cu impurities by phosphorus-doped regions	35
5.1 Phosphorus-gettering of Cu impurities	35
5.2 Sample preparation and experimental details	36
5.3 Cu-gettering by diffused emitters from POCl_3 source	38
5.4 Cu-gettering by ion-implanted emitters	39
5.4.1 Effect of bulk microdefects and oxygen precipitation on the Cu getterability	42
5.5 Implications towards silicon photovoltaics and microelectronics applications	43
6. Root cause analysis of Cu-LID	45
6.1 Defect characterization in terms of SRH recombination	45
6.1.1 Temperature dependence of capture cross sections and verification of previous fit results	47
6.1.2 Comparison with literature data	49
6.2 Defect characterization in terms of carrier recombination at extended metallic precipitates	50
6.2.1 Temperature dependence of precipitate-limited lifetime	52
6.3 Modeling Cu precipitation and comparison with fit results .	53
7. Fast detection and imaging of copper impurities in crystalline silicon	57
7.1 The problem of detecting Cu impurities in silicon	57
7.2 Accelerated Cu-LID	58
7.3 High-resolution imaging of Cu impurities by photoluminescence	60
7.3.1 Change in photoluminescence response during Cu-LID	60
7.3.2 Calibration and extraction of Cu-related lifetime . . .	61
7.3.3 Quantitative determination of Cu contamination levels	61
7.3.4 Applicability to multicrystalline silicon	64

8. Summary and outlook	67
References	69
Appendix: Schottky junction model	79
Publications	83

List of Publications

This thesis consists of an overview and of the following publications which are referred to in the text by their Roman numerals.

- I** **A.Inglese**, H.Laine, V.Vähänissi, H.Savin. Cu-gettering by phosphorus-doped emitters in *p*-type silicon: Effect on light-induced degradation. *AIP Advances*, 8, 015112, 2018.
- II** **A.Inglese**, J.Lindroos, H.Vahlman, H.Savin. Recombination activity of light-activated copper defects in *p*-type silicon studied by injection-and temperature-dependent lifetime spectroscopy. *Journal of Applied Physics*, 107, 052101, 2016.
- III** **A.Inglese**, H.Vahlman, W.Kwapil, J.Schön, H.Savin. Characterization of light-activated Cu defects in silicon: comparison with the recombination activity of metal precipitates. *Physica Status Solidi (c)*, 14, No. 7, 1700103, 2017.
- IV** H.Vahlman, A.Haarahiltunen, W.Kwapil, J.Schön, **A.Inglese**, H.Savin. Modeling of light-induced degradation due to Cu precipitation in *p*-type silicon. Part II: Comparison of simulations and experiments. *Journal of Applied Physics*, 121, 195704, 2017.
- V** **A.Inglese**, J.Lindroos, H.Savin. Accelerated light-induced degradation for detecting copper contamination in *p*-type silicon. *Applied Physics Letters*, 107, 052101, 2015.

Author's Contribution

Publication I: “Cu-gettering by phosphorus-doped emitters in *p*-type silicon: Effect on light-induced degradation”

With the help of the co-authors the author participated in the planning of the experiments and the preparation of samples. The author performed all experimental measurements and wrote the manuscript.

Publication II: “Recombination activity of light-activated copper defects in *p*-type silicon studied by injection- and temperature-dependent lifetime spectroscopy”

The author planned the experiments, processed the samples and performed all measurements. The author analysed the data and wrote the manuscript.

Publication III: “Characterization of light-activated Cu defects in silicon: comparison with the recombination activity of metal precipitates”

The author planned the experiments, processed the samples and performed all measurements. The author analysed the data with the help of the co-authors and wrote the manuscript.

Publication IV: “Modeling of light-induced degradation due to Cu precipitation in p-type silicon. Part II: Comparison of simulations and experiments”

The author actively participated in the planning of the experiments, processed some of the samples and helped with the execution of the lifetime measurements. The author wrote Section III F and critically revised the manuscript.

Publication V: “Accelerated light-induced degradation for detecting copper contamination in *p*-type silicon”

The author prepared the samples, performed the experiments, analysed the results with the help of the other co-authors and wrote the manuscript.

List of abbreviations, acronyms and symbols

List of abbreviations and acronyms

μ -PCD	Microwave Photoconductance Decay
Al_2O_3	Aluminum oxide
BMD	Bulk Micro Defects
BO-LID	Boron-Oxygen Light-Induced Degradation
Cu-LID	Copper-related light-induced degradation
Cu_3Si	Copper precipitate, copper silicide
Cu_i	Interstitial Copper
Cu_s	Substitutional Copper
CuB	Copper-Boron pair
CuGa	Copper-Gallium pair
Cz	Czochralski
DLTS	Deep-Level Transient Spectroscopy
DPSS	Deep Parameter Solution Surface
FeB	Iron-Boron pair
FZ-Si	Float-Zone silicon
HLI	High Level of Injection
IDLS	Injection Dependent Lifetime Spectroscopy
LID	Light-induced degradation
LLI	Low Level of Injection
LSQ	Least square
mc-Si	Multicrystalline silicon
PERC	Passivated Emitted Rear cell
PL	Photoluminescence

POCl_3	Phosphoryl chloride
QSSPC	Quasi-Steady State Photoconductance
QSSPL	Quasi-Steady State Photoluminescence
SCR	Space Charge Region
SEM	Scanning Electron Microscope
SiO_2	Silicon oxide
SIRM	Scanning Infrared Microscope
SPV	Surface Photo Voltage
SRH	Schockley-Read-Hall
SRV	Surface Recombination Velocity
TDLS	Temperature Dependent Lifetime Spectroscopy
TEM	Transmission Electron Microscope
TID	Transient Ion Drift

List of Greek symbols

α	Silicon absorption coefficient
β	QSSPC optical factor
Δn	Excess carrier concentration
$\mu_{n/p}$	Electron/Hole mobility
Φ_B	Schottky energy barrier
Φ_{ph}	Photon flux
ρ_{Cu}	Density of Copper atoms
$\sigma_{e/h}$	Electron/Hole capture cross section
σ_{prec}	Precipitate capture cross section
τ_{Aug}	Auger recombination lifetime
τ_{deg}	Minority carrier lifetime after illumination
τ_{init}	Minority carrier lifetime before illumination
$\tau_{n0/p0}$	Electron/Hole capture time constant
τ_{rad}	Radiative recombination lifetime
τ_s	Surface recombination lifetime
Ψ_n^S	Energy band bending
χ^2	Chi-squared fit error

List of Latin symbols

B_{rad}	Radiative recombination coefficient
$C_{n,p}$	Auger recombination coefficient
D	Carrier diffusivity
D_{Cu}	Copper diffusivity
d_n	Precipitate dissolution rate
E_c	Conduction band
E_i	Intrinsic energy level
E_t	Energy state
E_v	Valence band
E_{Fn}^S	Hole quasi Fermi level at precipitate/Si interface
E_{Fn}^S	Electron quasi Fermi level at precipitate/Si interface
E_F	Fermi energy level
G	Generation rate
g_n	Precipitate growth rate
I_{sc}	Short-circuit current
$J_{e/h}^S$	Thermionic emission current density of electrons/holes at precipitate/Si interface
$J_{e/h}^{sat}$	Saturation current density of electrons/holes
k	Capture cross section ratio (symmetry factor)
k_B	Boltzmann constant
L_n	Minority carrier diffusion length
n_0	Equilibrium electron concentration
N_a	Doping concentration (acceptor)
N_d	Doping concentration (donor)
N_t	Defect density
N_{prec}	Precipitate density
N_{Cu_i}	Interstitial copper concentration
N_{Cui}	Density of Interstitial Copper atoms
n_i	Intrinsic carrier concentration
p_0	Equilibrium hole concentration
q	Elementary charge
r_{prec}	Precipitate radius
S_{Cu}	Copper solubility
U	Recombination rate
V_{oc}	Open-circuit voltage
v_{th}	Carrier thermal velocity
W	Wafer thickness

1. Introduction

1.1 Background and research context

It was back in 1965 when Gordon Moore, cofounder of Intel® and Fairchild Semiconductor®, presented in the Electronics magazine what would later be identified as his law. Moore's prediction was that the number of integrated components on a chip would double every year [1, 2] and projected this rate of growth would continue for at least a decade. 52 years have passed since the formulation of the Moore's law, but, nevertheless, this pace of growth has remained unchanged and this year process technology will surpass the 10 nm node [3].

The dawn of photovoltaics also dates back to early 1960s, when scientists at Bells Lab announced the invention of the first silicon solar cell. At that time, the conversion efficiency was 6% [4]. Today the world record efficiency obtained with single-junction silicon solar cells stands at 26.7% [5].

There exists a common denominator behind the unabated miniaturization of integrated semiconductor devices and the continuous improvement of solar cell performance: silicon, i.e. the material from which most of these devices are made, and the demand for increasingly stringent levels of purity and crystal perfection.

Transition metals, such as iron (Fe), nickel (Ni) and copper (Cu), are among the most insidious impurities in silicon-based devices [6]. Besides being present in relevant quantities in the feedstock material [7, 8], additional sources of contamination are, among others, wafer sawing [9], the metallic parts of the equipment used for device processing and the use of metal alloys for contacts and interconnects [10].

Contamination from transition metals is responsible for a number of adverse effects in semiconductor-based devices, including the deterioration of

the gate oxide integrity [11, 12], the establishment of recombination active centers in the bandgap that degrade the minority carrier lifetimes [13, 14] with consequent increase in leakage currents [15] and parasitic short circuits. With regard to copper contamination, there exists an additional unwanted phenomenon caused by such impurity. This is the so-called *light-induced degradation* (LID) [16, 17], a phenomenon which progressively degrades the minority carrier lifetime during exposure to illumination. LID effects are typically considered a particular issue in silicon solar cells, where the decay of the carrier lifetime is often accompanied by a significant reduction of the conversion efficiency [18–20]. However, the relevance of this phenomenon can also be extended to all semiconductor-based devices that operate under illumination (e.g. photodetectors and light sensors) or carrier injection (e.g. diodes and transistors).

1.2 Research questions

The first scope of this dissertation is to investigate the impact of gettering, a well-established technique for driving impurities away from the active regions of semiconductor devices, on the extent of the Cu-related LID. Due to its high diffusivity in silicon [21, 22], Cu is generally regarded as a relatively benign impurity, which can be easily relocated from the bulk region of the wafer during the processing steps required for phosphorus diffusion. What is the impact of gettering on the Cu-related degradation process? Is Cu truly getterable to the extent that Cu-LID effects are fully mitigated? Chapter 5 and Publication I report the result of several experiments conducted with the aim of assessing the common belief of Cu contamination, and hence Cu-LID, being fully controllable by gettering. The results are then discussed in relation to the usual requirements of photovoltaic or microelectronic applications.

The second goal of this dissertation is to provide new insights into the root cause of Cu-LID that still remains debated despite nearly two decades of research on this topic. Specifically, what is the recombination active defect resulting from the light-activation of Cu species? What are the degradation mechanisms behind the establishment of such strong recombination centres? In Publications II-IV the recombination activity of the defect responsible for Cu-LID will be investigated through lifetime spectroscopy methods. The results obtained from these studies will then be compared with the outcome of a comprehensive model which attempts to describe the

physical principles behind the light-activation of Cu species.

In addition to elucidating the root cause of the light-activated precipitation process, the results included in Publications II-IV provide the theoretical foundation for addressing the problem of quickly detecting trace Cu concentrations in silicon, which represents the third scope of this dissertation. Specifically, this thesis explores the possibility of inducing Cu-LID for rapidly detecting Cu impurities in silicon and proposes an algorithm that enables quantitative and spatially resolved imaging of Cu contaminants in silicon wafers.

1.3 Structure of this dissertation

The content of this thesis is divided into 8 chapters. Chapters 2-4 provide the reader with the necessary theoretical background for understanding and discussing the main results of this doctoral work. Specifically, chapter 2 includes the recombination models used in Publications I-III, chapter 3 provides a literature review of the impurity copper and its related complexes in silicon, whereas Chapter 4 reviews the experimental techniques used in all publications.

The main results included in this thesis are summarized in Chapters 5-7. The impact of phosphorus gettering on the extent of Cu-LID effects is presented in Chapter 5, which includes the experimental results presented in Publication I together with additional data that will be included in forthcoming publications.

Chapter 6 compiles the results reported in Publications II-IV and presents an overview of the modeling and characterization work for elucidating the root cause of Cu-LID. These results also represent the theoretical foundation for the content of Chapter 7, where the findings described in Publication V are combined with the description of the aforementioned Cu-imaging algorithm. A summary of the main results is finally presented in Chapter 8 together with recommendations for further studies.

2. Charge carrier recombination in crystalline silicon

The minority carrier lifetime is an important figure of merit for defining the quality of a semiconductor substrate and its suitability towards a specific device. In this thesis, this parameter represents the starting point for addressing the research questions of this dissertation through an extensive modelling and characterization work.

In the following sections, the concepts of carrier recombination and lifetime will be briefly introduced. The main carrier recombination mechanisms will then be presented with a focus on bulk recombination processes.

2.1 Carrier generation, recombination and lifetime

When a semiconductor is exposed to a light with photon energy larger than the semiconductor bandgap, electron-hole pairs are formed and excited electrons are promoted to the conduction band, while leaving behind an equal concentration of excess holes in the valence band. This process is often referred to as *generation*. After generation of the excess carriers, a fraction of the electrons in the excited state recombine with holes and the annihilation of the electron-hole pair is often called *recombination*. The carrier lifetime τ generally refers to the average time elapsing between the generation of the electron-hole pairs and the subsequent recombination. On the base of this formulation, τ is related to the recombination rate per volume (U) and the excess carrier concentration ($\Delta n = \Delta p$) as follows

$$U = \frac{\Delta n}{\tau}. \quad (2.1)$$

Many pathways exist for the recombination of excess carriers, each of them described by a specific recombination rate and lifetime. Hence, the experimentally measured effective lifetime is the result of the simultaneous interplay of various recombination mechanisms, which will be briefly described in the next sections of this chapter.

2.2 Radiative recombination

Radiative recombination is also defined as *band-to-band* recombination since it represents the reverse process to the optical generation, through which electron-hole pairs directly annihilate releasing a photon with energy corresponding to the semiconductor bandgap. The radiative recombination rate is determined by the following relation

$$U_{rad} = B_{rad}(np - n_i^2) \quad (2.2)$$

where B_{rad} is the radiative recombination coefficient, which is material-dependent, and n_i is the intrinsic carrier concentration. Considering that silicon is an indirect bandgap semiconductor, the probability of a direct transition from the conduction band to the valence is relatively low compared to direct bandgap materials. For example, in silicon $B_{rad} = 9.5 \times 10^{-15} \text{ cm}^3 \text{s}^{-1}$ [23], which is several orders of magnitude smaller than in e.g. GaAs. This is due to the fact that in silicon the annihilation of an electron-hole pair must be assisted by a quasiparticle, called *phonon*, which carries the necessary momentum for the occurrence of the radiative emission.

Although it is usually weaker than other recombination processes in silicon, the radiative recombination is the physical principle behind the photoluminescence characterization method described in Sec. 4.3.

2.3 Auger recombination

Auger recombination is a process that involves three particles, namely an electron-hole pair and an additional electron or hole. In this case, the energy generated by the annihilation of the electron/hole pair is not released in the form of a photon but transferred to another electron or hole. The general formulation of the Auger-related recombination rate is given by the equation

$$U_{Aug} = C_n(n^2 p - n_i^2 n_0) + C_p(np^2 - n_i^2 p_0) \quad (2.3)$$

where C_n and C_p are the Auger recombination coefficients [24]. When electron-hole pairs are generated, the total carrier concentration becomes $n = n_0 + \Delta n$ and $p = p_0 + \Delta n$ and, on the base of Eq. 2.1, the lifetime associated to Auger recombination in *p*-type silicon becomes

$$\tau_{Aug}^{LLI} = \frac{1}{C_p N_a^2} (\Delta n \ll p_0), \quad \tau_{Aug}^{HLI} = \frac{1}{(C_n + C_p)\Delta n^2} (\Delta n \gg p_0). \quad (2.4)$$

Therefore, according to the classical formulation of the Auger recombination, the Auger-related lifetime shows a weak dependence on Δn at low level of injection ($\Delta n \ll p_0$), whereas it acquires an inverse quadratic dependence on the the excess carrier concentration towards the high injection regime ($\Delta n \gg p_0$).

In more recent years, it has been observed that the experimentally measured Auger lifetime is generally lower than the values predicted by Eq. 2.4. The reason for this discrepancy has been attributed to the Coulombic interaction of charge carriers, which enhances the Auger-related recombination rate. An improved parametrization has thus been proposed by Kerr *et al.* [25] by fitting the model to a large set of empirical data. On the base of this parametrization, the Auger-related lifetime can be rewritten as

$$\tau_{Aug} = \frac{\Delta n}{np(1.8 \times 10^{-24}n_0^{0.65} + 6 \times 10^{-25}p_0^{0.65} + 3 \times 10^{-27}\Delta n^{0.8})}, \quad (2.5)$$

which is the model used in the next chapters for estimating the contribution of Auger recombination mechanisms to the measured experimental data.

2.4 Shockley-Read-Hall (SRH) recombination

While Auger and radiative recombination are intrinsic recombination processes that occur irrespective of the material quality, the Shockley-Read-Hall (SRH) theory quantitatively defines the carrier recombination mechanisms assisted by the presence of impurities, defects and imperfections of the crystal lattice.

Such model relies on the assumption that each defect introduces a discrete number of energy states in the bandgap of the semiconductor [26] [27]. Two mechanisms are defined at such localized energy states, i.e. the capture and emission of holes and electrons. When the same carrier is captured and emitted to the conduction/valence band, the energy state is often defined as a carrier *trap*. Such trapping behaviour gives rise to well-known measurement artifacts during lifetime testing (see Chapter 4). Conversely, when both an electron and a hole are captured into the localized energy state in the bandgap, this energy state becomes a *recombination centre* for the electron-hole pair.

The recombination rate at these states is regulated by the carrier capture probability at the given energy level E_t . Supposing equal excess electron and hole concentrations ($\Delta n = \Delta p$), the SRH lifetime associated with a

single-level defect is defined as

$$\tau_{SRH} = \frac{\tau_{n0}(p_0 + p_1 + \Delta n) + \tau_{p0}(n_0 + n_1 + \Delta n)}{n_0 + p_0 + \Delta n}, \quad (2.6)$$

where $\tau_{n0} = (N_t v_{th} \sigma_n)^{-1}$ and $\tau_{p0} = (N_t v_{th} \sigma_p)^{-1}$ and n_1, p_1 define the population of holes and electrons in the given energy level E_t through the equations derived from the Fermi-Dirac distribution function

$$n_1 = N_c \exp\left(-\frac{E_c - E_t}{k_B T}\right) \quad p_1 = N_v \exp\left(-\frac{E_t - E_v}{k_B T}\right), \quad (2.7)$$

where the effective densities of states at 300K are taken as $N_c = 2.86 \times 10^{19} \text{ cm}^{-3}$ and $N_v = 3.1 \times 10^{19} \text{ cm}^{-3}$ [28]. The quantities N_t and $\sigma_{n,p}$ that appear in the capture time constants $\tau_{n0,p0}$ represent the defect density and the capture cross section, respectively. This latter parameter describes the effectiveness of the energy state in capturing a hole or electron. In addition, the product $v_{th} \sigma_{n,p}$, where $v_{th} \sim 10^7 \frac{\text{cm}}{\text{s}}$ [29] is the carrier thermal velocity, can be visualized as the volume swept out by a mobile carrier per unit time with cross section σ_n . If the energy state lies within this volume, the electron is captured by it. The capture cross section is a fundamental parameter for the classification and characterization of the electrical properties of the defect. In some cases the ratio

$$k = \frac{\tau_{p0}}{\tau_{n0}} = \frac{\sigma_n}{\sigma_p} \quad (2.8)$$

is defined in lieu of the single values of $\sigma_{n,p}$ to define the recombination activity of the energy state.

2.4.1 Influence of defect parameters on SRH recombination

In order to examine the physics behind the SRH formalism, the influence of E_t and k on the SRH lifetime in p-type silicon has been separately plotted in Figs. 2.1a and 2.1b. If it is assumed that the energy level lies near the mid-bandgap (i.e. it is a *deep* energy state), the SRH lifetime increases towards high injection conditions. Specifically, assuming acceptor doping concentrations $N_a = 10^{15} - 10^{16} \text{ cm}^{-3}$ and deep energy levels, from Eq.2.7 it results that $n_1, p_1 \ll p_0$, such that at low and high injection Eq. 2.6 reduces to

$$\tau_{SRH}^{LLI} = \tau_{n0} \quad , \quad \tau_{SRH}^{HLI} = \tau_{n0} + \tau_{p0} = \tau_{n0}(1 + k). \quad (2.9)$$

At low injection the SRH recombination rate is thus determined by the capture of minority carriers, which is limited by their relatively low concentration with respect to majority carriers. Conversely, under high injection

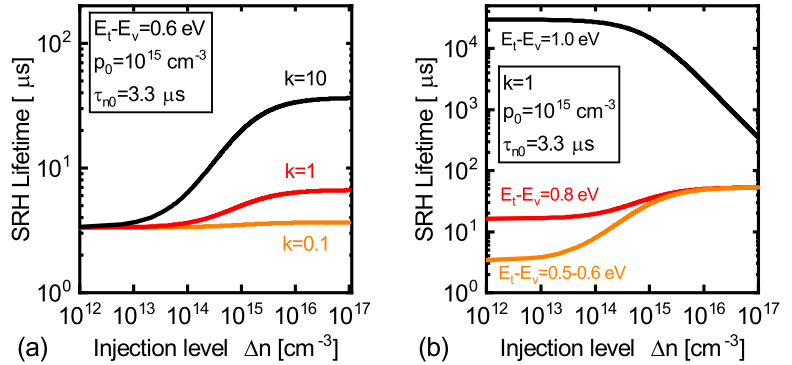


Figure 2.1. (a) Influence of the symmetry factor on the SRH lifetime for a deep energy level $E_t - E_v = 0.5$ eV and varying capture cross section ratios. (b) Influence of the energy level E_t on the SRH lifetime for fixed capture cross section ratio $k = 1$. For all curves plotted in the figures, a p-type substrate doping of 10^{15} cm⁻³ and a minority capture time constant $\tau_{n0} = 3.3$ μs have been assumed.

conditions the steady-state concentration of holes and electrons becomes comparable and the SRH lifetime saturates to the sum of the capture time constants for holes and electrons. Hence, at high injection the SRH lifetime is mostly influenced by the slowest between the minority and majority carrier capture processes. Under these conditions the increment of the capture cross section ratio imposes increasingly large electron capture cross sections, such that in *p*-type silicon the capture of majority carriers at the energy state becomes the dominant recombination-limiting mechanism. Figure 2.1b displays the influence of the the energy level on the injection dependence of the SRH lifetime. It can be observed that deep energy levels are the strongest recombination centres, as the SRH lifetime associated to these states is generally lower than in the case of shallow traps. Furthermore, the shift of the energy level towards the conduction or valence bands qualitatively changes the shape of the injection-dependence of τ_{SRH} from an increasing to decreasing trend at high injection conditions.

According to Eq. 2.7, for shallow energy states the captured carrier concentrations n_1, p_1 in the energy state exponentially increase when the energy level approaches the conduction and valence bands, respectively. Hence, depending on the position of the energy state in the semiconductor bandgap, the SRH recombination process is limited by either majority or minority carrier capture. For example, from Eq. 2.7 it results that in *p*-type Si shallow energy states in the upper bandgap half are mostly populated with electrons ($n_1 \gg p_1$). Recombination at shallow energy

states is thus limited by the low probability for holes to be trapped. Similar considerations apply to shallow energy states in the lower bandgap half. In this case, the population of carriers is reversed ($p_1 \gg n_1$) and the recombination process is similarly hindered by the low capture probability of minority carriers.

2.4.2 Defect classification based on SRH parameters

E_t and k represent the typical fingerprints for classifying and distinguishing defects in semiconductor. Besides providing information on the recombination strength of the underlying defect, k also reveals its electrical state. Specifically, in semiconductors the energy states introduced by defects and impurities may act as *donors* or *acceptors*. Donor defects are prone to releasing electrons, thus acquiring a positively charged state. Conversely, acceptor states tend to trap electrons and, when this occurs, they achieve a negatively charged state. As donor levels alternate between a positive and neutral state, the charged state is more attractive to electrons than the neutral state is to holes. For this reason, these states are likely to acquire a large electron capture cross section, which imposes $k > 1$. On the other hand, acceptor states alternate between negative and neutral states and similar considerations lead to expect that $k < 1$. Likewise, more extreme values of k (i.e. $k \gg 1$ or $k \ll 1$) are usually associated to energy states that act as *double* donors or acceptors (i.e. doubly charged states).

2.5 Carrier recombination at extended defects

The SRH model is generally well-suited for describing the carrier recombination at *point-like* defects that are not extended in space in any dimension and introduce a discrete number of energy states in the semiconductor bandgap. Besides establishing point-like defects, impurities can cluster together to form small regions of a different phase, which are often referred to as *precipitates*. Such precipitates extend along the three dimensions in the host crystal lattice and generally give rise to a continuous band of energy states. Although in some cases the recombination activity of extended defects can be approximated assuming single energy states (as discussed in Publication II), a rigorous description of carrier recombination at metallic precipitates requires more advanced models than simple SRH statistics. In Publication III the recombination activity of light-activated

Cu defects has been studied on the base of a numerical model proposed by Plekhanov *et al.* [30], which will be described in the next section.

2.5.1 Recombination at metallic precipitates - the Schottky model

The model is based upon the assumption that a Schottky junction with a barrier height Φ_{Bp} is formed between the silicide (metallic precipitate) and the surrounding semiconductor. A sketch of the metallic precipitate and the energy band bending under illumination and in thermal equilibrium conditions is presented in Fig. 2.2. The precipitate is assumed to be spherical and, when the junction is formed, a concentric space-charge region (SCR) is established around the silicide. The formation of a SCR and the consequent band bending at the Schottky contact ($e\Psi_n^S$) also involves the positive charging of the precipitate induced by the electric fields in the SCR.

The recombination activity of such metallic precipitates is based upon the thermionic emission of charge carriers across the Schottky junction. The current densities for electrons and holes at the precipitate-Si interface (J_e^S and J_h^S) can be written as [31, 32]

$$J_e^S = J_e^{sat} \left(\exp \left(\frac{E_{Fn}^S - E_F^M}{k_B T} \right) - 1 \right) \quad (2.10)$$

$$J_h^S = -J_h^{sat} \left(\exp \left(\frac{E_F^M - E_{Fn}^S}{k_B T} \right) - 1 \right), \quad (2.11)$$

where k_B is the Boltzmann constant and J_e^{sat} and J_h^{sat} are the saturation current densities of electrons and holes. Under the assumption that electrons and holes quasi-instantly recombine at the precipitate-Si interface, it can be written that

$$J_e^S = -J_h^S. \quad (2.12)$$

The calculation of the metallic precipitate recombination rate under illumination implies the numerical solution of the continuity equations for electrons and holes and the Poisson equation. The necessary boundary conditions can be derived from Eq. 2.12 together with Eqs. 2.10 and 2.11, as described in the Appendix. Given a certain generation rate G and doping concentration N_a , the value to which J_e^S converges allows to calculate the recombination rate associated to a precipitate of radius r_n as

$$R_{prec}(r_n, G, N_a, T) = N_{prec} \cdot \frac{4\pi r_n^2 \cdot J_e^S(r_n, G, N_a, T)}{e}. \quad (2.13)$$

Repeating the numerical simulation for several values of G allows the determination of the recombination rate as a function of different levels of

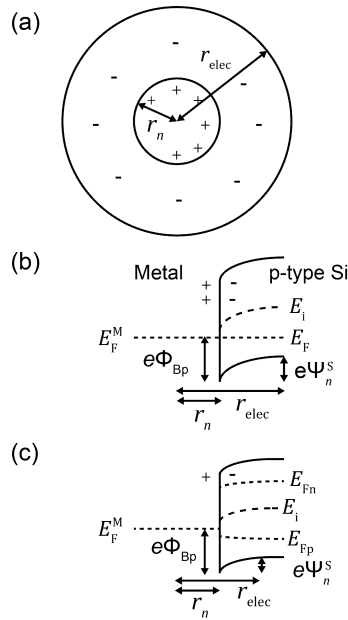


Figure 2.2. (a) Structure of a charge precipitate and surrounding space charge region, and energy band diagram under (b) thermal equilibrium and (c) illumination. (Reprinted with permission H.Vahlman, A.Haarahiltunen, W.Kwapił, J.Schon, A.Inglese, H.Savin, *Journal of Applied Physics* **121**, 195703, 2017)

injection. For a given excess carrier concentration Δn , the carrier lifetime limited by the precipitate with metallic core of radius r_n can be calculated from Eq. 2.1 as

$$\tau_{\text{prec}} = \frac{\Delta n}{R_{\text{prec}}(r_n, \Delta n, N_a, T)}. \quad (2.14)$$

Parametrization of precipitate-related lifetime

In order to ease the determination of the precipitate-limited lifetime, a parametrization has been recently proposed for quickly calculating τ_{prec} , without the need of numerical simulations. This parametrization consists of a set of equations which allows to calculate the dependence of the recombination rate R_{prec} on the input parameters, i.e., the doping N_a , Δn and the precipitate radius r_n . Note that this parametrized model only reproduces the lifetime injection dependence at room temperature, whereas for modeling the recombination activity at higher temperatures than 300K, finite-element simulations are necessary, as no specific parametrization exists. Further information on the Schottky model and the associated parametrization can be found at Refs. [33] and [34].

2.5.2 Influence of doping and precipitate size/density on the recombination activity

Since precipitates act as minority carrier traps, the precipitate-related lifetime can also be written as

$$\tau_{\text{prec}}(\Delta n, N_{\text{prec}}, r_n, N_A) = \frac{1}{v_{th} N_{\text{prec}} \sigma_{\text{prec}}(\Delta n, r_n, N_A)}, \quad (2.15)$$

where σ_{prec} represents the effective capture cross of the precipitate. By equating Eq. 2.14 with Eq. 2.15, the variation of σ_{prec} (and therefore τ_{prec}) as a function of the input parameters of the model (i.e. N_A , Δn and r_n) can be quickly calculated by means of the aforementioned parametrization.

Figure 2.3 illustrates the variation of the injection dependence τ_{prec} for different values of the precipitate radius and the semiconductor doping. It can be noticed that for all values used as input parameters for the model, the precipitate-related lifetime maintains a monotonic increasing trend for all injection conditions (i.e. similar injection dependence as deep SRH energy states). This increasing trend is explainable from the extent of the band bending at the precipitate/semiconductor interface (see Fig. 2.2). Under carrier injection, the photogenerated excess carrier concentration reduces the electric field around the junction and therefore the band bending in the SCR. Hence, with increasing injection levels, the width of the SCR around the silicide shrinks and so does the precipitate-related capture cross section.

The effect of the semiconductor doping on τ_{prec} and σ_{prec} is displayed in Figure 2.3a. At low injection conditions, lower lifetime (hence a larger capture cross section) is obtained in more lightly doped silicon. This behaviour arises from the fact that under pseudo-equilibrium conditions (as in the case of very low injection level) the extent of the SCR of a Schottky junction is inversely proportional to the semiconductor doping. When the injection level is increased, the situation becomes reversed, i.e. higher lifetime values (hence smaller capture cross sections) are generally observed with light semiconductor doping. This is again explainable by looking at Figure 2.2. Lighter doping implies that the condition for high injection ($\Delta n >> n_0, p_0$) is reached for lower values of Δn than in the case of heavily doped substrates. This means that the scenario depicted in 2.2c, where carrier injection flattens the total band bending around the Schottky junction, is reached for lower values of Δn . With increasing levels of injection the band bending at the junction is further reduced and so does the width of the SCR.

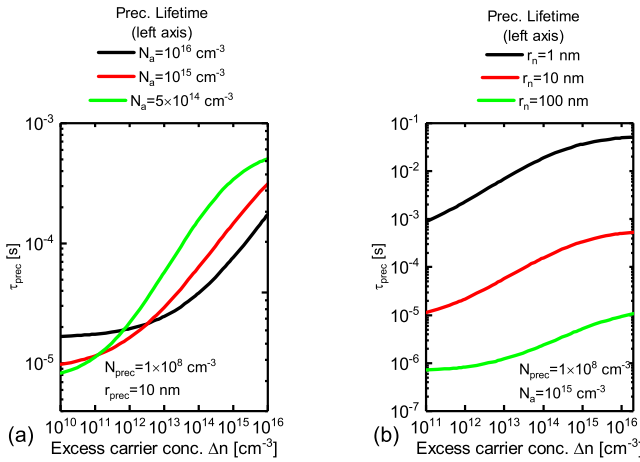


Figure 2.3. Influence of the semiconductor doping (a) and precipitate radius (b) on the injection dependence of the precipitate-related lifetime τ_{prec} assuming a fixed precipitate density for all curves ($N_{\text{prec}} = 10^8 \text{ cm}^{-3}$)

2.6 Surface recombination

The surface of a semiconductor sample terminates the periodicity of the crystal lattice, thus becoming a highly recombination active region. Surface recombination processes originate from the establishment of dangling covalent bonds caused by the large number of partially bonded Si atoms at the surface and the local stress in the crystal lattice imposed by the reconfiguration of the crystal structure to the lowest energy. The surface energy states generally behave similarly to the bulk defects and therefore the associated recombination processes can be modeled with the same SRH statistics as previously discussed in Sec. 2.4.

Analogously to extended bulk defects, surface energy states are continuously distributed across the whole bandgap. Hence, the calculation of the surface-related recombination rate in principle requires the integration of the SRH equation across the energy range where surface energy states are located. Instead of using this extended SRH formalism, the strength of surface recombination is often approximated with a single effective SRH energy level and its extent is expressed in terms of a parameter called *surface recombination velocity* (SRV). This is because the surface recombination rate is expressed per unit area, whereas in Eq. 2.1, any bulk recombination mechanism is expressed as a rate per unit volume. The SRV is thus defined as

$$SRV = \frac{U_s}{\Delta n}, \quad (2.16)$$

where U_s is the surface recombination rate defines in the units mentioned above.

In addition to the implications on the energetic position of the SRH energy states, the estimation of the SRV injection dependence requires the experimental determination of the interface defect concentration D_{it} and the capture cross sections of the surface states, as well as the calculation of the electron and hole densities at the surface by means of the algorithm proposed by Girisch et al. [35].

Since surface recombination occurs on both sides of the wafer and it may be affected by carrier diffusion, specific relations exist between the surface-limited lifetime and the SRV. For sufficiently low values of SRV (< 250 cm/s), the following relation holds between SRV and surface-limited lifetime [36, 37]

$$\frac{1}{\tau_s} \simeq \frac{2 \cdot SRV}{W}, \quad (2.17)$$

where W is the wafer thickness.

2.7 Calculation of the effective carrier lifetime

As stated earlier, the experimentally measured carrier lifetimes are the result of the interplay of all recombination processes, i.e. Auger, band-to-band, bulk and surface recombination. The effective carrier lifetime is calculated as

$$\tau_{eff} = \left(\frac{1}{\tau_{rad}} + \frac{1}{\tau_{Aug}} + \frac{1}{\tau_{bulk}} + \frac{2 \cdot SRV}{W} \right)^{-1}. \quad (2.18)$$

With regard to τ_{bulk} , the contribution from SRH energy states and metal precipitates of radius r_n can also be written as

$$\frac{1}{\tau_{bulk}} = \sum_i \frac{1}{\tau_{SRH,i}} + \sum_n \frac{1}{\tau_{prec(r_n)}}. \quad (2.19)$$

It results evident that, because of the structure of Eq. 2.18, for a given level of injection the effective lifetime is mostly limited by the recombination process providing the lowest lifetime. Figure 2.4 shows an example of effective carrier lifetime limited by Auger, intrinsic and SRH recombination. It can be observed that radiative and Auger recombination produce a significant impact on the effective lifetime only at high injection conditions, whereas the SRH recombination by deep energy states is generally the dominating recombination process in the low to mid-injection regime.

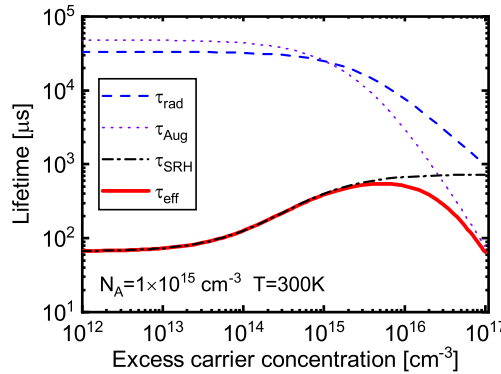


Figure 2.4. Effective carrier lifetime and contributions from Auger, Radiative and SRH recombination processes. For the calculation of the effective lifetime, a SRH asymmetric deep level ($E_c - E_t = 0.45 \text{ eV}$ $k = 100$) has been assumed.

3. Copper in Silicon

This chapter gathers the existing literature information on the impurity copper in silicon and its related complexes. The content is divided in three main parts: in the first the physical properties of Cu in silicon will be reviewed, the second includes a summary of Cu-related complexes and associated recombination activity and in the third part the literature information on the Cu-related light-induced degradation will be reviewed. This chapter mainly serves the purpose of providing the reader with the necessary background for discussing the content of all Publications included in this thesis work.

3.1 Physical properties

Copper (Cu) is commonly classified as a *3d* transition metal impurity, where the symbol *3d* defines the outer shell of the electron configuration of the atom. The particular electronic configuration of Cu ($3p^63d^{10}4s^1$) favours the ionization from a neutral state to a positively charged interstitial form (Cu_i^+) [22, 38–40], such that it becomes a shallow single donor in silicon. In this electrical state, the atomic radius of Cu_i^+ atoms becomes very small compared to the silicon lattice (radius estimated to be about 0.074 Å [22], while the silicon lattice constant is 5.43 Å [41]), producing direct implications on its physical properties, namely diffusivity, solubility and electrical activity.

3.1.1 Diffusivity

In intrinsic silicon the copper diffusivity has been determined with the Transient Ion Drift (TID) method as [42]

$$D_{Cu,in}(T) = (3.0 \pm 0.3) \times 10^{-4} \times \exp(-0.18 \pm 0.01 eV/k_B T) \text{ (cm}^2/\text{s}) \quad (3.1)$$

where k_B is the Boltzmann constant and T is the temperature in Kelvin scale.

In p-type silicon, positively charged Cu_i^+ ions tend to pair with negatively charged substitutional boron B_s^- , giving rise to CuB pairs [22]. The effect of this pairing is that only a fraction of the total copper concentration is mobile at a given moment, slowing down the overall diffusion process. Hence, for moderately doped silicon the effective diffusivity of copper atoms is given by the following formula [42]

$$D_{\text{eff}} = \frac{3 \times 10^{-4} \times \exp(-2090/T)}{1 + 2.584 \times 10^{-20} \times \exp(4990/T) \times (N_a/T)} \text{ (cm}^2/\text{s}) \quad (3.2)$$

where N_a indicates the boron doping level. If room temperature and $N_a = 10^{16} \text{ cm}^{-3}$ are assumed, for typical values of wafer thickness (e.g. $t = 400 \mu\text{m}$) Eq. 3.2 gives an average diffusion time of $\tau_d = \frac{t^2}{D_{\text{eff}}} \simeq 24.2 \text{ h}$, which is several orders of magnitude smaller than in the case of e.g. iron [43].

3.1.2 Solubility

The solubility of a given impurity represents the maximum concentration that remains dissolved in the host material at a certain temperature. In the case of Cu, the solubility in intrinsic silicon has been measured as [44]

$$S_{\text{Cu,in}}(T) = 5 \times 10^{22} \times \exp\left(2.4 - \frac{1.49 \text{ eV}}{k_B T}\right) \text{ cm}^{-3}, \quad (3.3)$$

in the range $500^\circ\text{C} < T < 800^\circ\text{C}$. Due to the Fermi level effect and the aforementioned pairing between boron atoms and Cu_i^+ atoms, Eq. 3.3 underestimates the copper solubility in p-type silicon. In order to take into account these effects, an additional correction factor to Eq. 3.3 has been proposed by Hoelzl *et al.*, such that the effective Cu solubility in p-doped silicon can be rewritten as [45]

$$S_{\text{Cu,eff}}(T) = S_{\text{Cu,in}} \times \exp\left(\frac{E_i - E_f}{k_B T}\right) \times (1 + [N_a K_{\text{CuB}}]), \quad (3.4)$$

where $E_i - E_f$ indicates the distance between the Fermi and the intrinsic energy level and the factor K_{CuB} accounts for the Cu-B pairing effect [46]. Despite the solubility enhancement imposed by these two effects, extrapolation of the Cu solubility to room temperature through Eq. 3.4 indicates a vanishingly low value of less than 10^8 atoms per cm^{-3} when $N_a = 1 \times 10^{16} \text{ cm}^{-3}$, which is higher than other transition metal impurities (e.g. Fe) but also several orders of magnitude lower than the Cu_i^+ concentrations experimentally measured. Indeed, TID measurements on

intentionally Cu contaminated samples revealed that Cu impurities remain in an interstitial form up to concentrations of 10^{15} - 10^{16} cm $^{-3}$ [47]. The reason for these high interstitial Cu concentrations has been hypothesized by Flink *et al.* [21, 47] to be the electrostatic repulsion between Cu $_{\text{i}}^+$ and positively charged precipitates. This theory also represents one of the starting assumptions for modelling of the Cu precipitation kinetics under illumination in Publication IV.

A direct consequence of the high concentrations of Cu $_{\text{i}}^+$ atoms that remain in interstitial form is the out-diffusion of these species to the surface in bare p-type silicon wafers [47, 48]. This phenomenon is due to the fact that the only pathways for Cu $_{\text{i}}^+$ atoms to reach the equilibrium solubility are either the transformation into Cu silicides (precipitation), which is however obstructed by the electrostatic interaction between Cu $_{\text{i}}^+$ and the growing precipitates, or the out-diffusion to the surface. This latter phenomenon is reduced to a negligible extent when the wafer is coated with a surface layer containing native positive charge (*e.g.* silicon dioxide) or positive ions are deposited on the wafer surface [49].

3.2 Copper complexes and recombination activity

Interstitial copper

As mentioned earlier, when Cu is introduced in crystalline silicon, it acquires a positively charged ionized form and quickly diffuses through the interstitial sites of the silicon lattice. As shown in Fig. 3.1, interstitial copper has been associated with a donor energy level located at $E_c - 0.15$ eV with an electron capture cross section of 1.5×10^{-15} cm $^{-3}$ [40]. Due to the shallow energy level and the small capture cross section associated to this defect, interstitial copper does not cause significant minority carrier recombination in silicon. Consequently, when Cu impurities are in the interstitial form, their effect cannot be detected through minority carrier lifetime measurements. However, as thoroughly described in this thesis, such copper impurities become very strong recombination centres during low-temperature anneals [50] or exposure to illumination [16, 51].

Substitutional copper

The transformation of Cu $_{\text{i}}^+$ atoms into a substitutional defect (Cu $_{\text{s}}$) near structural defects such as vacancies, dislocations and stacking faults has been reported in a wide range of publications, where the electrical ac-

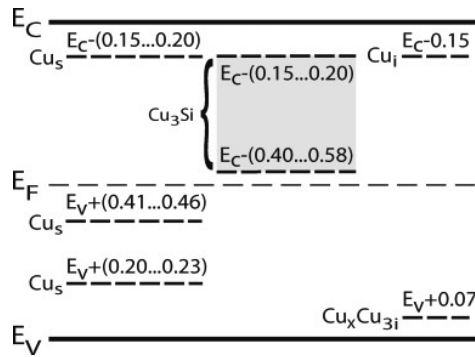


Figure 3.1. Energy levels and electrical state of Cu-related complexes in silicon (reprinted with permission from J.Lindroos, H.Savin, *Solar Energy Materials and Solar Cells* **147**, 115-126, 2016. Copyright 2015, Elsevier B.V.)

tivity of such defects has been studied by means of Deep Level Transient Spectroscopy (DLTS) or near-bandgap photoluminescence [43, 52, 53]. Several energy levels have been associated to Cu_s , specifically a donor energy state located at $E_v + (0.20 - 0.23)$ eV, an acceptor energy level at $E_v + (0.41 - 0.46)$ eV and an additional shallow energy state in the upper half of the bandgap at $E_c - (0.15...0.2)$ eV. No information is available regarding the electron capture cross sections (σ_e) of such energy states, however considering the acceptor nature of the deep energy level at $E_v + (0.41 - 0.46)$ eV and the considerations made in Sec. 2.4.2, it is reasonable to expect a small electron capture cross section and, therefore, a symmetry factor $k \ll 1$.

Copper precipitates

The precipitation of interstitial Cu atoms leads to the formation of highly recombination active $\eta - Cu_3Si$ silicides. While substitutional copper is a point-like defect establishing discrete energy levels in the silicon bandgap, the extended nature of Cu precipitates involves the formation of strain in the silicon lattice and the emission of stacking faults during precipitation [54]. This results in the formation of a continuous band of energy states, which DLTS studies indicated to be located in the upper half of the bandgap between $E_c - 0.15$ eV and $E_c - 0.58$ eV [46, 55].

The size of Cu-silicide precipitates has been reported to vary from few to several thousands of nm depending on a number of factors such as the presence of structural defects in the silicon lattice, the supersaturation level or the cooling rate after high temperature treatments [22, 46, 56]. As discussed in Chapter 2, the recombination activity of metal precipitates

is strongly dependent on the size and density. In addition to the recombination processes involving the thermionic emission of carriers discussed in Sec. 2.5.1, when the size of metal precipitates approaches the sub-10 nm scale, the recombination properties of these precipitates have been hypothesized to become affected by charge tunnelling [57] at the precipitate/semiconductor interface. In the modelling work that will be presented in Chapter 5, this phenomena have been assumed to produce a negligible effect on the recombination activity of the light-activate Cu precipitates.

Other copper-related complexes

Various acceptor elements (*e.g.* B, In, Ga and Al) are known to bind with mobile interstitial copper atoms, forming copper-acceptor pairs. Such complexes, however, are unstable at room temperature and do not exist in sufficiently high concentrations (only 0.1% of the total Cu concentration) to produce any relevant recombination activity.

In literature Cu has also been reported to form a pure copper complex, which was initially presumed to be a Cu_sCu_i complex [58] and later identified as a four copper atom defect, whose composition was hypothesized to be $\text{Cu}_{s1}\text{Cu}_{i3}$ [59, 60]. A shallow energy level at $E_v + 0.07 \text{ eV}$ [61] has been associated to this Cu complex through DLTS and PL measurements.

3.3 Copper-related light-induced degradation (Cu-LID)

The expression *light-induced degradation* (LID) defines a parasitic effect in crystalline silicon that results in the progressive decay of the minority carrier lifetime during exposure to illumination. This phenomenon is of particular relevance for silicon solar cells, where the decrement in carrier lifetime is often accompanied by drastic efficiency losses during illumination.

In the scientific community, LID has been a matter of intense research since early 1970s [62] and, in the course of the years, many theories have been formulated to explain various experimental observations. The presence of copper contamination has also been observed to induce a similar effect in silicon, albeit with several distinguishing characteristics from other widely reported LID phenomena [17, 63]. This section summarizes the existing literature information on the copper-related degradation process (Cu-LID).

Phenomenology and experimental observations

The first report on Cu-LID is dated back to 1998, when Tarasov *et al.* observed light-induced degradation in p-type Cz-Si wafers contaminated with Cu concentrations below the doping level [64]. Later, further evidence of the effect of copper contamination on the lifetime/diffusion length was found from experiments conducted with oxygen-lean FZ-Si [16, 51] and Ga-doped Cz-Si [65], which indicated that neither oxygen nor boron doping are prerequisites for the occurrence of Cu-related LID effects.

In more recent studies, indications of Cu-LID caused by unintentional contamination have been found in *p*-type mc-Si wafers [66], mc-Si Al-BSF solar cells [67] and PERC cells fabricated from seed-cast quasi-monocrystalline silicon [20]. These studies provided direct indications of Cu-LID effects in industrial solar cells caused by unintentional Cu contamination introduced during the fabrication steps or natively present in the feedstock material.

Kinetics of the degradation process

Figure 3.2 shows the minority carrier lifetime decay caused by Cu contamination in intentionally Cu-contaminated B-doped FZ-Si sample. For comparison purposes, the image also reports the lifetime data obtained with a reference uncontaminated FZ-Si sample. The Cu-related degradation appears to be a single stage process which starts affecting the minority carrier lifetime after several tens of minutes of exposure to illumination and leads to saturation of the lifetime decay after several thousands of minutes. As can be seen from Fig. 3.2, the lifetime decay observed in Cu-

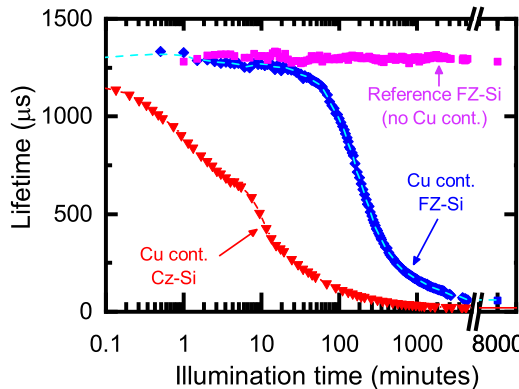


Figure 3.2. Effect of Cu-LID on the minority carrier lifetime measured in reference clean and intentionally contaminated boron-doped FZ-Si and Cz-Si samples ($\sim 3 \Omega \cdot cm$) with a Cu contamination level of $\sim 1 \times 10^{14} \text{ cm}^{-3}$. All samples were light soaked at room temperature under a 0.65 Suns LED lamp.

contaminated Cz-Si samples follows a different trend compared to FZ-Si. In this case, the effect of Cu-LID becomes visible upon exposure to illumination and appears to follow multiple degradation stages. In Ref. [68] the fit of the lifetime data to exponential functions indicated the coexistence of three simultaneous processes, *i.e.* a fast initial degradation followed by a second slower and a final very slow lifetime decrease. However, considering that Cz-Si is also prone to the so-called boron-oxygen (B-O) degradation [69] it is likely that some of the aforementioned degradation phases could be attributed to the co-occurrence of this latter phenomenon.

The Cu-related degradation process has also been observed to become faster with increasing temperature [68], illumination intensity [20, 51] and copper concentration [16]. In addition, the presence of bulk microdefects (BMDs), such as oxygen precipitates, has been shown to dramatically accelerate the Cu-related LID process and reduce the lifetime value to which the degradation process saturates.

With regard to the dependence of the degradation rate on the doping level, an inverse relationship exists between the Cu-LID degradation rate and the boron doping concentration, *i.e.* slower degradation kinetics have been observed with increasing boron concentrations. The reason for this behaviour was initially thought to be related to the slower Cu diffusivity in presence of heavier boron doping due to increased Cu-B pairing [66]. However, according to the model presented in Publication IV and Ref. [63] this dependence of Cu-LID kinetics on the doping concentration is likely to arise from the higher solubility of Cu with increasing boron concentrations. The Cu-related degradation kinetics were also found to depend on the acceptor doping element. Specifically, the observation of Cu-LID in B- and Ga-doped samples with equal doping and Cu concentrations revealed considerably slower degradation kinetics in the Ga-doped specimens [65]. A similar dependence on the doping element and density was also observable in Cu contaminated mc-Si specimens [70].

Effect of low-temperature thermal treatments

Upon light-activation of Cu defects, no lifetime recovery has been observed after low temperature anneals (*e.g.* 200°C for 10 minutes) performed in dark conditions. In Publication V a partial, yet incomplete recovery has been observed in lightly Cu contaminated areas ($[Cu_i] < 10^{14} \text{ cm}^{-3}$). On the other hand, in presence of stronger Cu contamination levels no significant lifetime enhancement has been observed [50, 68].

Influence of surface charge

The surface charge has been found to significantly influence the extent of Cu-LID effects. Specifically, remarkable reduction of Cu-related lifetime degradation was obtained through deposition of an aluminum-oxide layer with native negative charge [68] or a sufficiently large amount of negative corona charge on a passivating silicon dioxide layer [66, 71]. This behaviour has been attributed to the high diffusivity of copper ions at room temperature and the electrostatic attraction between surface charge and interstitial Cu ions in the wafer bulk.

Root cause and responsible defect

Transient ion drift (TID) measurements indicated that the Cu-LID effect is accompanied by a considerable reduction of the concentration of Cu_i^+ [72] during illumination. Concerns about Cu-LID arising from surface recombination were raised by Boehringer *et al.* However, recent contributions have confirmed that Cu-LID predominantly arises from increased bulk recombination [73, 74]. Hence, these findings imply that Cu-LID is likely to stem from the transformation of Cu_i^+ atoms into a different bulk recombination-active state, which however remains unknown.

Based on the literature information summarized in Sec. 3.2, possible candidates for the defect responsible of Cu-LID are substitutional copper defects (Cu_s) or copper precipitates. Early contributions attributed Cu-LID to the dissociation of a recombination inactive pure copper complex and the subsequent release of highly recombination active Cu_s complexes [50, 51]. However, the observation of a strong dependence of the Cu-related degradation rate on the bulk microdefects density and the energetic position of the quasi-Fermi level under illumination led to hypothesize that Cu-LID is the result of a light-activated precipitation process [75, 76].

In order to shed new light on the defect and the mechanisms leading to Cu-LID, in Chapter 6 the recombination activity of the defect behind Cu-LID has been studied through lifetime spectroscopy methods.

4. Experimental methods for carrier lifetime measurements

This chapter reviews the lifetime characterization techniques used for obtaining the experimental results reported in this thesis. After discussing the operation principles, a focus is maintained on the strengths and weaknesses of each method.

4.1 Quasi-steady state photoconductance (QSSPC)

The physical principle behind the QSSPC measurement method is the change in substrate conductivity induced by the excess carrier generated by the pulse of a Xenon flash light (see Figure 4.1).

The starting point for the determination of the carrier lifetime is the time evaluation of the excess carrier density, which is derived from the continuity equation [77], *i.e.*

$$\frac{d\Delta n(t)}{dt} = G(t) - U(t), \quad (4.1)$$

where it has been assumed that the charge is homogeneously distributed across the whole wafer thickness. By inserting the relation $U(t) = \Delta n(t)/\tau$ (*i.e.* Eq. 2.1) into Eq. 4.1 and solving for τ , it results

$$\tau = \frac{\Delta n(t)}{G(t) - \frac{d\Delta n(t)}{dt}}. \quad (4.2)$$

Hence for the determination of the effective lifetime it is necessary to accurately determine both the generation rate and the excess carrier concentration as a function of time. In the lifetime tester used in this thesis work (Sinton WCT-120TS) the generation rate is calculated from the photogenerated current in a reference cell (I_{ref}), *i.e.*

$$G(t) = \beta \frac{I_{ref}(t)}{qW}, \quad (4.3)$$

where β is a reflectivity-dependent optical constant, computed by comparing experimentally measured reference currents with PC1D simulation

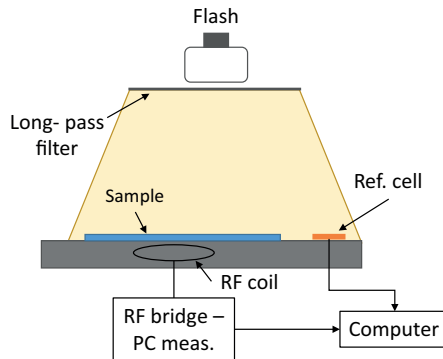


Figure 4.1. Simplified schematic of a QSSPC lifetime tester.

results.

The excess carrier concentration Δn is separately calculated from the variation of the conductivity of the sample $\Delta\sigma(t)$ measured by a 2 cm-wide coil connected to a Radio-Frequency (RF) bridge. The relation between Δn and the conductivity change follows the equation

$$\Delta n(t) = \frac{\Delta\sigma(t)}{q(\mu_n + \mu_p)W}, \quad (4.4)$$

where μ_n and μ_p are the electron and hole mobilities and W is the wafer thickness.

Eq. 4.2 refers to a generalized case [77], in which steady-state conditions are not necessarily reached (*i.e.* the generation and recombination processes are not necessarily in balance). The name *quasi-steady state* (QSS) [78] derives from the first version of the setup in which the time constant of the flash light decay was assumed to be considerably longer than the measured lifetime. If this condition is met, for each point of the measurement the excess carrier density remains approximately constant (*i.e.* $\frac{d\Delta n(t)}{dt} \approx 0$) and Eq. 4.2 reduces to $\Delta n = G\tau$. Considering that the decay time constant of the flash is 2-3 ms, the assumption of quasi-steady conditions remains valid only if carrier lifetime is at least 10-fold shorter than the duration of the flash pulse. Nonetheless, through the generalized Eq. 4.2, the range of measurable lifetime values can be extended to approximately the same order of magnitude as the duration of the flash pulse.

Experimental setup used in this dissertation

The instrument used in Publications II and III (Sinton WCT-120TS) also features a temperature controlled measurement stage, which allows to measure the injection dependent lifetime curves at temperatures between

20°C and 200°C. In this thesis, temperature-dependent measurements were performed by initially heating the measurement stage up to the maximum temperature and subsequently measuring the lifetime after predefined temperature steps of the cooling transient. Since Eq. 4.4 requires the determination of the carrier mobility, for each temperature the values of μ_n and μ_p were recalculated according to the Dorkel–Leturcq's mobility model [79].

Strengths and limitations

The QSSPC technique is a simple, contactless and non-destructive method, which is widely used in photovoltaics research. In addition, this technique is capable of measuring the dependence of the minority carrier lifetime over a wide injection range in the timeframe of a flash pulse.

Nonetheless, the QSSPC technique also presents several drawbacks and artifacts which shall be mentioned. All photoconductance-based techniques generally suffer from trapping artifacts when the lifetime measurement is performed at low injection conditions (typically when $\Delta n < 10^{14} \text{ cm}^{-3}$). These artifacts arise from the fact that, instead of directly recombining with holes, the excess electrons are captured and re-emitted back to the conduction band by shallow carrier traps (see Sec. 2.4). This effect results in the abnormal increase of the measured lifetime because the *lifespan* of the excess carriers is extended by the amount of time they remain trapped. These trapping effects vanish when the injection is raised above the trap density since, under this condition, all traps become filled and no longer affect the measurement.

In addition to trapping effects, it is worth mentioning that the QSSPC technique also suffers from the so-called depletion region modulation (DRM) effect, which results in the overestimation of the minority carrier lifetime at low injection regime [80]. This phenomenon is due to distortions in the excess conductance measurement caused by variations in depletion width of p-n junctions during the flash pulse.

Finally, it must be pointed out that, besides being sensitive to the room temperature variations (hence requiring periodical recalibration of the instrument), the QSSPC lifetime tester only allows to measure a small area of the sample at a time, thus providing little to no information on the lifetime spatial distribution.

4.2 Microwave-photoconductance decay (μ -PCD)

A simplified schematic of the measurement system is presented in Fig. 4.2. The physical principle behind the μ -PCD is similar to QSSPC, i.e. the change in conductance caused by carrier light-excitation. However, unlike the QSSPC technique, the excess carriers are generated by a near-infrared laser source which illuminates a small area of the wafer (up to 0.5 mm^2). The photoconductivity transient is then monitored by detecting the change in microwave reflectivity of the sample area under test.

During the detection of the photoconductance decay, no excess carriers are generated, hence Eq.4.2 reduces to

$$\tau = \frac{\Delta n(t)}{-\frac{d\Delta n(t)}{dt}} \quad (4.5)$$

The solution of this differential equation with respect to Δn yields an equation on the form of $\Delta n(t) = A \times \exp(-t/\tau)$ and, therefore, the carrier lifetime can be extracted from a fit of the measured decay to this single exponential function. From Eq. 4.5 it results evident that this technique does not require the determination of the generation rate and the excess carrier density. Furthermore, since the measurement is performed in a tiny area of the sample, the measurement probe can be scanned across the sample in order to obtain spatially resolved lifetime maps.

Nonetheless, this technique also features several drawbacks. Being a photoconductance-based method, the μ -PCD technique is prone to the same trapping artifacts as previously mentioned for the QSSPC method. This parasitic effects are usually minimized by setting a sufficiently high carrier excitation (typically $\Delta n > 10^{14} \text{ cm}^{-3}$). Another limitation of the first scanners employing this technique was related to the fact that no

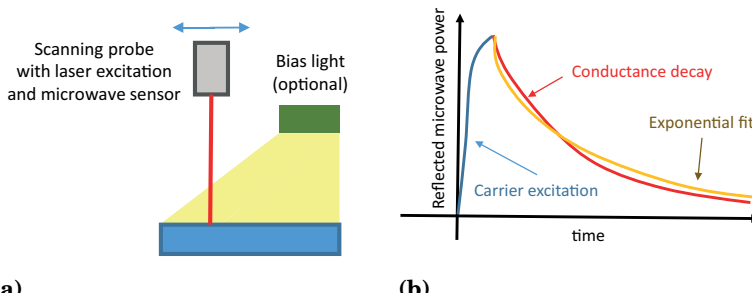


Figure 4.2. (a) Schematic illustration of the μ -PCD measurement setup. (b) Illustration of the photoconductivity transient decay from which the carrier lifetime is extracted through an exponential fit.

information on the lifetime injection dependence can be obtained from the analysis of the photoconductance decay. However, more recent instruments (*e.g.* Semilab PV-2000 [81]) are equipped with a large bias light to set a baseline for the level of injection in the sample. Hence, the excess conductivity transient created by the laser source can be treated as a minimal perturbation of the total photoconductivity, such that the level of injection can be assumed to remain approximately constant throughout the decay.

4.3 Photoluminescence imaging (PL-I)

Camera-based photoluminescence imaging represents one of the latest advances in lifetime metrology. A schematic illustration of the measurement setup is presented in Fig. 4.3.

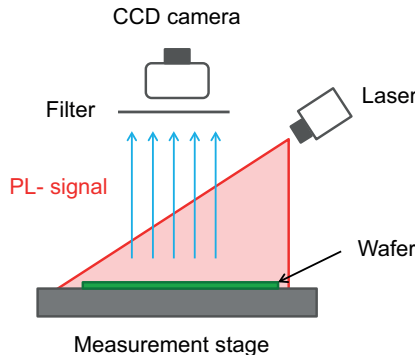


Figure 4.3. Illustration of PL-imaging experimental setup. A large-beam laser is used to homogeneously excite the excess carriers. The photons emitted through band-to-band recombination of the excess carriers are detected by a CCD camera.

The physical principle underlying this technique is the band-to-band radiative recombination introduced in Sec. 2.2. When excess carriers are optically generated, a small fraction of the excited carriers recombine through the emission of a photon with an energy corresponding to the energy gap of the semiconductor (in this case Si).

As the measurement setup in Fig 4.3 alone does not provide any quantification of the carrier lifetime, this characterization method must be coupled with other methods that provide a direct quantification of the carrier lifetime in a small portion of the sample under test. The lifetime maps are therefore obtained through a *calibration* procedure, which relates the strength of the raw PL signal to the effective lifetime values.

Photoconductance-based calibration

The PL-calibration by means of QSSPC represents the standard method implemented in various commercially available tools. Since one photon is generated for each recombination event, the PL emission rate (Φ_{PL}) equals the radiative recombination rate U_{rad} reported in Eq. 2.2. In a p-type substrate it results that $p = N_a + \Delta n$ and $n = n_0 + \Delta n \approx \Delta n$, such that Φ_{PL} can be written as

$$\Phi_{PL} = B_{rad}(np - n_i^2) = B_{rad}(N_a\Delta n + \Delta n^2). \quad (4.6)$$

The intensity of the PL signal detected by the CCD sensor (I_{PL}) is proportional to Φ_{PL} by means of an instrument- and sample-specific constant C_{cal} which accounts for the fraction of emitted light detected by the CCD sensor. Hence,

$$I_{PL} = C_{cal} \cdot \Phi_{PL} \quad (4.7)$$

and from Eq. 4.6 it is possible to derive the following expression

$$\Delta n(x, y) = \sqrt{\left(\frac{N_a}{2}\right)^2 + \frac{I_{PL}(x, y)}{C_{cal}B_{rad}}} - \frac{N_a}{2}. \quad (4.8)$$

Eq. 4.8 relates the measured PL intensity to the excess carrier concentration in each point of the PL image. Since PL images are measured under steady-state conditions, the effective lifetime becomes

$$\tau(x, y) = \frac{\Delta n(x, y)}{G} = \frac{\Delta n(x, y)}{(1 - R)\Phi_{ph}/W}, \quad (4.9)$$

where G is the generation rate imposed by the laser optical excitation, R is the front reflectance of the measured sample, Φ_{ph} is the photon flux of the laser source and W is the wafer width. If the carrier generation rate imposed by the laser source is known, in the calibration area the excess carrier concentration Δn_{cal} and lifetime for the given generation rate can be extracted from the injection dependent lifetime curves measured with the QSSPC technique. The calibration coefficient C_{cal} hence can be calculated as

$$C_{cal} = \frac{I_{PL,cal}}{B_{rad}(N_a\Delta n_{cal} + \Delta n_{cal}^2)} \quad (4.10)$$

and, once the value of this parameter is known, the effective lifetime values at each point of the image can be calculated through Eqs. 4.8 - 4.9. In general, this standard calibration process is robust when the test sample is relatively homogeneous. Indeed, it is based on the assumption that, since the calibration is performed on the test sample itself, there are usually negligible variations in doping, thickness, and optical properties of the

calibration region compared to the rest of the test sample. However, this assumption may not be verified in the case of mc-Si and therefore several alternative approaches have been proposed to overcome this drawback.

Alternative calibration methods

In recent implementations of PLI, the calibration procedure has been conducted without the need of secondary photoconductance measurements. These advanced calibration methods are based on a relatively novel technique for determining the minority carrier lifetime, called *quasi steady-state photoluminescence* (QSSPL). Two different approaches have been proposed for determining the carrier lifetime, and hence C_{cal} , from the QSSPL signal. In the former, the excess carriers are excited with a sinusoidal optical source inducing a photoluminescence response that follows the excitation source with a certain phase shift that corresponds to the effective carrier lifetime. An iterative procedure is described in Ref. [82] for extracting the injection dependent lifetime curves and hence derive the value of C_{cal} . In the latter, the calibration coefficient is determined via a self-consistent procedure initially proposed by Trupke et al. for determining the generation rate during photoconductance measurements [83] and later extended for calibrating photoluminescence [84]. In this case, the generation coefficient $G(t)$ and the intensity of the PL response I_{PL} are separately measured and C_{cal} is determined such that the hysteresis of the lifetime calculated through Eq. 4.2 becomes minimized during the rising and falling branches of the excitation waveform. As QSSPL measurements are usually performed on a small area of the wafer, an averaging procedure has then been proposed by Giesecke et al. in order to derive spatially resolved maps from the QSSPL lifetime information [85].

Strengths and limitations

Since it is based on a CCD camera, PLI is a very fast and contactless technique which allows to obtain lifetime maps in the timespan of few seconds with resolution in the μm range. The high spatial resolution obtainable with this characterization method makes it particularly suitable for characterizing multicrystalline silicon substrates, where lifetime variations at the grain boundaries and intra-grain regions would be masked by the insufficient resolution of other imaging techniques. [86, 87]

With regard to the abovementioned QSSPL technique, the main advantage over photoconductance-based methods is its capability of measuring at very low injection conditions (up to 10^{10} cm^{-3}) without suffering from trapping

artifacts.

Irrespective of the technique being used for calibrating the raw data, the main limitation of PLI arises from the fact that a secondary measurement is always necessary to obtain a quantification of the carrier lifetime across the sample area. In addition, when the QSSPL method is used, the calibration procedure becomes more complex and further complications arise when the lifetime measurements are not performed at room temperature conditions.

4.4 Surface photovoltage (SPV)

While the techniques reviewed in the previous sections measure the carrier lifetime, the surface photovoltage method quantifies the minority carrier diffusion length (L), which is related to the effective lifetime (τ) by the relation $L = \sqrt{D\tau}$, where D is the minority carrier diffusivity in the wafer under test [41].

A schematic representation of the operation principle and the experimental setup is shown in Fig. 4.4(a). The excess carriers are generated through monochromatic illumination. The extrapolation of the diffusion length is based on the detection of the surface photovoltage (V_{SPV}) by means of a non-contact Kelvin probe. Assuming a p-type substrate and a shallow surface n-doped layer (as shown in Fig. 4.4), when the wafer is exposed to a photon flux, the optical carrier excitation results in the reduction of the

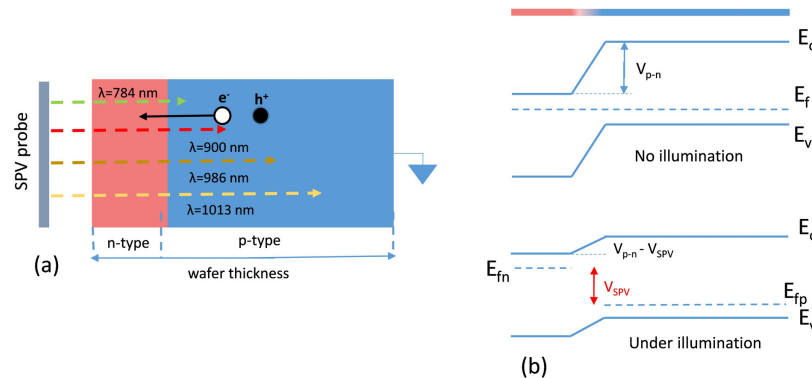


Figure 4.4. (a) Sample cross-section for SPV measurements. Excess carriers are generated by monochromatic illumination (the image reports 4 different wavelengths used in Semilab WT-85 XL). (b) Band diagram of the p-n junction in the dark and under carrier excitation. The band bending after optical excitation is denoted as $V_{p-n} - V_{SPV}$ where V_{p-n} is the built-in voltage of the p-n junction.

band bending across the p-n junction and the photogenerated electrons are subsequently collected by the surface n-doped layer [88].

As depicted in Fig. 4.4(b), the photovoltage is determined by the energetic separation between the quasi-Fermi levels arising from the non-equilibrium condition imposed by excess carrier excitation (the value of the photovoltage also corresponds to the reduction in band bending caused by excess carrier generation). Note that the term "surface" derives from the application of this measurement technique to wafers with a surface inversion layer, in lieu of a p-n junction. In this case, the inversion layer acts as collecting junction for the generated carriers and the variation of the band bending across the depletion region at the front surface during dark and carrier excitation conditions determines the value of V_{SPV} .

If the photon flux is kept constant, a linear relationship exists between the photovoltage and the diffusion length [55]

$$\frac{1}{V_{SPV}} = C_{SPV} \left(L_n + \frac{1}{\alpha(\lambda)} \right), \quad (4.11)$$

where C_{SPV} is a constant and $\alpha(\lambda)$ is the absorption coefficient of silicon for each wavelength [89] used for carrier photogeneration. The SPV scanner used in Publication V and chapter 5 (Semilab WT-85 XL) is equipped with a monochromator, which generates 4 different wavelengths in the near infrared region ($\lambda = 784 - 1013 \text{ nm}$). By exposing the sample to each wavelength and simultaneously measuring the V_{SPV} , a linear plot of $1/V_p$ versus $1/\alpha$ is obtained, from which the constant C and the diffusion length L_n can be readily fitted. The same procedure is then repeated for each point of the wafer, yielding a spatially resolved map of the diffusion length across the specimen.

Applications, strengths and limitations

As previously mentioned, the SPV method requires the sample to be pre-treated with a surface p-n junction or inversion layer. In the studies presented in Publication V and chapter 5, the SPV technique has been employed to detect bulk recombination processes in phosphorus-diffused samples that would not be directly measurable with the other characterization methods because of the co-occurrence of carrier recombination in the emitter region.

An additional advantage of this technique is represented by the fact that it generally operates at low injection conditions (typically $\Delta n = 10^{11} - 10^{12} \text{ cm}^{-3}$ [90]) and it is immune to the trapping artifacts previously described for PC-based techniques.

Since it is a point-by-point mapping technique, the measurements by means of the SPV method are considerably slower than e.g. QSSPC or PL imaging. Furthermore, it must be pointed out that an important limitation exists on the thickness of the wafers that can be reliably measured. Eq. 4.11 is only valid under the assumption that the wafer thickness is at least four times larger than the carrier diffusion length ($t_{\text{wafer}} \geq 4L_n$ [55]). When thin wafers are measured, such assumption no longer holds and Eq. 4.11 fails to describe the relationship between $1/V_p$ and $1/\alpha$. Hence, the linear fit, from which the diffusion length is extracted, may lead to significant deviations from the real values. In more recent implementations of the SPV method this limitation on the wafer thickness has been overcome by inserting a correction factor into Eq. 4.11, which accounts for the non-linearities arising from the reduced sample thickness [91].

5. Gettering of Cu impurities by phosphorus-doped regions

5.1 Phosphorus-gettering of Cu impurities

Gettering is a process by which metallic impurities are relocated to regions of the wafer where their detrimental effect on the device performance is minimal. In several silicon-based devices, such as solar cells, gettering naturally takes place during the formation of the phosphorus-doped emitter, which acts as a collecting region for the impurities initially located in the bulk region of the wafer.

While most of the previous gettering studies have focused on slow diffusing impurities (e.g. Au or Fe) [92], little literature information exists on the gettering of fast diffusing species. With regard to Cu, there exists a restricted number of publications indicating that large fractions of Cu contaminants remain segregated into the phosphorus-doped layer after gettering (e.g. in Refs. [93], [94] and [7]). However, such literature information does not fully elucidate the impact of phosphorus gettering on the occurrence of Cu-LID. Indeed, the aforementioned gettering studies have been conducted with heavily doped phosphorus layers, whereas in several applications, such as state-of-the-art solar cells [95, 96], it has become preferable to lower the doping level of the emitter in order to minimize the downsides arising from excessive doping, such as the formation of electrically inactive phosphorus layers [97] or the increase in emitter saturation currents [98]. Furthermore, the detection limit of the techniques used to assess the gettering efficiency is often close or above the threshold Cu concentrations that trigger LID effects, such that from the existing literature information no conclusion can be drawn as to whether phosphorus gettering results in the complete suppression of Cu-LID.

The aim of this chapter and Publication I is to ascertain whether Cu is

truly getterable to the extent that the associated Cu-LID phenomena are fully suppressed. The study has also been conducted with the purpose of identifying the critical processing parameters with largest impact on the gettering efficiency and Cu-LID effects.

5.2 Sample preparation and experimental details

In this chapter the Cu getterability has been studied with two different emitter profiles. In the former, the experiments have been conducted with a conventional n^+ emitter diffused from a POCl_3 source, whereas in the latter the emitter region has been formed by first implanting a light phosphorus dose and then diffusing the implant through a high temperature anneal. All experiments reported in this chapter have been performed with p-type monocrystalline Cz-Si specimens with resistivity of $3.4 \Omega \text{ cm}$.

The relevant process steps for both study cases are summarized in Fig. 5.1 and further details can be found in the experimental section of Publication I. In these experiments a surface phosphorus-doped layer has been created on the front side of each specimen and the Cu-contamination dose has been diffused from the opposite undoped side. The drive-in of the Cu contamination dose and gettering have been simultaneously performed during an isothermal anneal (800°C for 20 min) followed by a fast ($\sim 240^\circ\text{K/min}$) or a slow ($\sim 4^\circ\text{K/min}$) cooling ramp, as depicted in Fig. 5.1(c). Note that in these experiments only a specific region of the wafer has been intentionally contaminated such that the behaviour of contaminated and uncontaminated areas can be directly compared from the same specimen.

The emitter sheet resistances and doping profiles of all samples are reported in Fig. 5.2. In this study the Cu getterability has been studied in presence of lightly doped layers with sheet resistance in the range of $80 - 95 \Omega \cdot \text{sq}^{-1}$, which is higher than the values reported in previous literature data (e.g. in Ref. [7]).

The LID caused by bulk Cu contamination has been detected through the SPV technique reviewed in Sec. 4.4. The use of this characterization method allows to directly monitor the Cu-related light-induced effects in the wafer bulk without further sample processing. Specifically, during the SPV characterization the emitter layer becomes a collecting junction for the photogenerated minority carriers in the bulk region, thus allowing the determination of the associated diffusion length across the sample area.

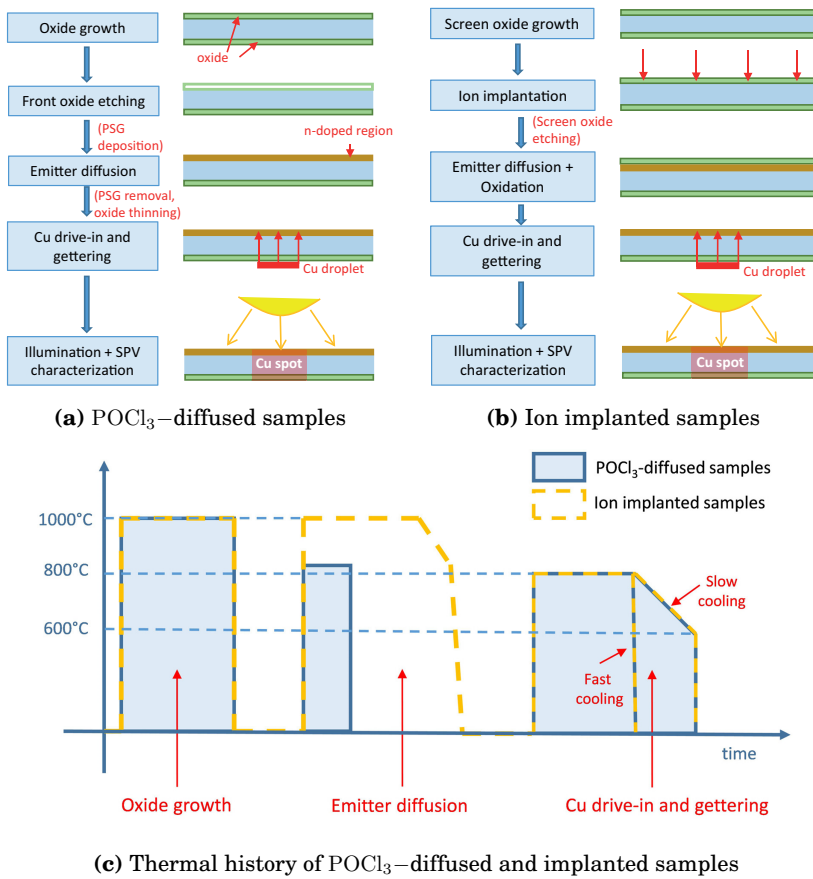


Figure 5.1. Schematic illustration of the process flow for emitter formation, drive-in of the Cu contamination dose (spot Cu contamination) and gettering in samples with diffused (Figure a) and ion implanted emitter (Figure b). Figure c shows the thermal history of samples with diffused (blue line) and ion implanted emitter (yellow). Notice the longer high-temperature step in the case of the implanted samples, which is necessary for activating the phosphorus implant and recovering the implantation debris.

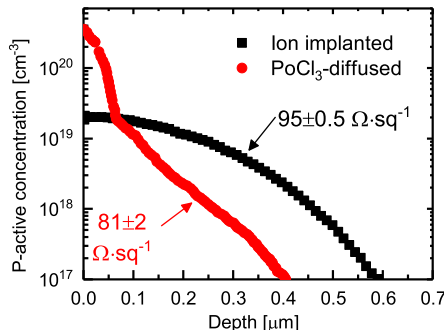


Figure 5.2. Electrically active phosphorus doping profile measured by Electrochemical Capacitance-Voltage (ECV) in the samples described in this chapter.

5.3 Cu-gettering by diffused emitters from POCl_3 source

Figure 5.3 shows the diffusion length maps measured after 120 hours of illumination at room-temperature in samples that underwent the phosphorus diffusion process from a POCl_3 source. For comparison purposes the figure also shows the diffusion length map of a contaminated specimen without emitter (hence no gettering).

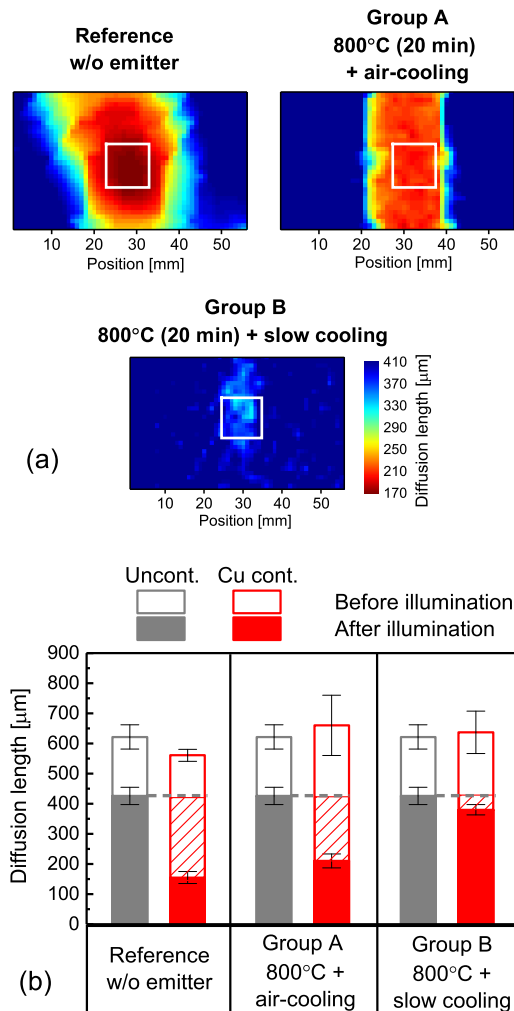


Figure 5.3. (a) Diffusion length maps measured after 120 h in ungettered and gettered samples which experienced fast and slow cooling after the gettering anneal. The white rectangles mark the region-of-interest (ROI) from which the values were averaged and plotted in figures (b). Figure (b) reports the average diffusion length measured within the Cu contaminated spot and outside this region. The shaded areas highlight the diffusion length decay caused by Cu-LID. (reprinted from A. Inglesi et al. *AIP Advances* **8**, 015112, Copyright CC BY 3.0)

In all samples, the Cu-spot becomes visible only after exposure to illumination, indicating that the residual Cu contamination after the gettering treatment remains in a recombination inactive state until the sample is light-soaked. During illumination, a different behaviour can be observed between the samples that underwent the fast and slow cooling process. While the gettering treatment with the slow cooling tail leads to the nearly complete disappearance of any Cu-LID effect, in the specimen that underwent the fast cooling treatment the Cu-contaminated region clearly remains distinguishable from the background region. By comparing the diffusion length measured in this latter set of specimens and the reference wafers without phosphorus emitter, it results that (i) in the gettered sample the decay of the diffusion length saturates to higher values ($\sim 150\mu m$ vs. $\sim 210\mu m$) and (ii) the Cu-related degradation process becomes significantly slower after the gettering treatment (see Fig. 3 of Publication I). Hence, these results support the conclusion that the gettering anneal followed by air-cooling results in partial, yet insufficient decrease in bulk Cu contamination for effectively suppressing the associated Cu-LID effects.

5.4 Cu-gettering by ion-implanted emitters

Figure 5.4 presents the diffusion length measured before and after illumination in the phosphorus-implanted samples. The experiment has been carried out with the same substrates previously used for $POCl_3$ diffusion (Cz-Si $\sim 3\Omega \cdot cm$ with oxygen content of > 15 ppma). It results evident that, in these implanted samples none of the tested gettering schemes was capable of effectively mitigating Cu-LID, since during illumination the diffusion length of all samples decreased up to $\sim 60\mu m$, regardless of the cooling phase. Furthermore, it is possible to notice that before light-soaking the measured diffusion length is approximately half of the value previously reported with $POCl_3$ -diffused samples. This different behaviour, however, is unlikely to arise from the incomplete recovery of the implantation debris, as the SPV method is solely sensitive to bulk recombination, whereas crystal damage from low-energy implantation is usually confined to only few μm below the surface. In order to gain deeper understanding into the cause for the persistence of Cu contamination and the considerably lower average diffusion length detected in these implanted specimens, the same experiments have been repeated with similar FZ substrates featuring a considerably lower bulk oxygen concentration than the Cz-Si wafers used

previously. The subset on the right-hand side of Figure 5.4(b) reports the experimental results obtained with these samples after the slow cooling tail. Interestingly, in these samples the gettering treatment resulted in the complete disappearance of the Cu-spot. Hence, the ineffectiveness of the gettering treatments in the implanted Cz-Si wafers cannot be attributed to the lighter emitter doping concentration with respect to the POCl_3 -diffused layer, nor to parasitic effects caused by dopant implantation (e.g. lattice damage or contamination from the ion implanter) because, if this were the case, it would be reasonable to expect similar experimental results in all the implanted wafers used for this study. Conversely, the remarkably different behaviour observed between these Cz- and FZ-Si samples is likely to originate from the different oxygen concentrations in the specimens used for these gettering tests.

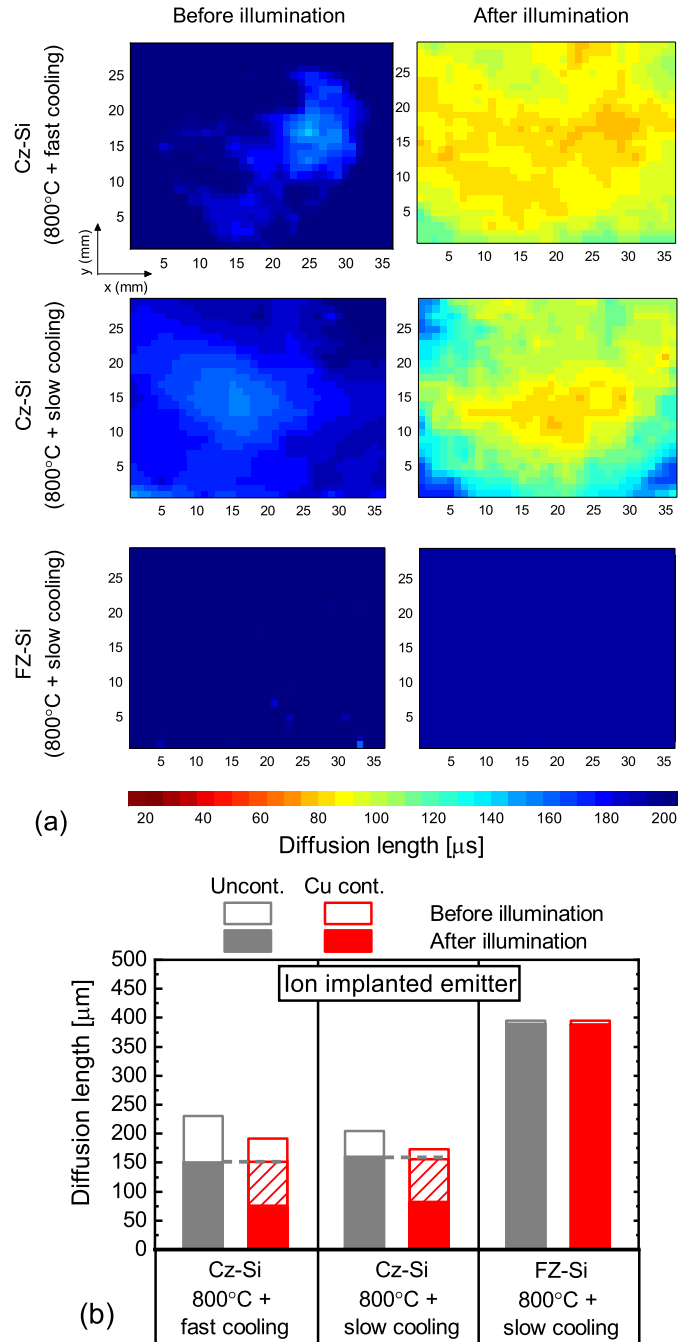


Figure 5.4. Figure (a) shows the diffusion length maps measured in phosphorus implanted Cz- and oxygen lean FZ-Si specimens. The average diffusion length measured before and after illumination in all samples are displayed in the histograms of Figure (b). For comparison purposes, the histograms also report the diffusion length values measured outside the Cu-spot.

5.4.1 Effect of bulk microdefects and oxygen precipitation on the Cu getterability

In order to gain deeper understanding into the reason for the persistence of Cu-LID in the implanted Cz-samples, it is instructive to take a glance at the diffusion length map measured with the ion implanted samples before the gettering anneal (see Fig. 5.5(a)). The appearance of ring-like patterns in lifetime/diffusion length maps is a typical indication of oxygen precipitation. In silicon, oxygen impurities mainly exist in the form of interstitial atoms, which alone do not act as active recombination centres, or in the form of oxide precipitates, whose effect on the electrical and mechanical properties of the silicon substrate has been widely documented [99, 100].

Evidence on the probable precipitation of oxygen species can be found from Fig. 5.5(b), which shows a micrograph obtained with a scanning infrared microscope (SIRM) in correspondence of the ring pattern. The image reveals the presence of bulk microdefects (BMDs), which could not be found in detectable quantities through analogous measurements performed on POCl_3 -diffused and the reference samples without emitter. Although such technique does not provide any information on the chemical and elemental composition of the BMDs, the detection of bulk precipitates only in the implanted samples, whose thermal budget is considerably heavier than the POCl_3 -diffused and the reference Cz-Si samples, is a direct indication of oxygen precipitation in these specimens.

As described in Chapter 3, the presence of BMDs has been proven to considerably strengthen Cu-LID effects [75] and lower the threshold Cu concentrations necessary for triggering visible light-induced effects [49]. The unintentional growth of these oxide precipitates also explains the

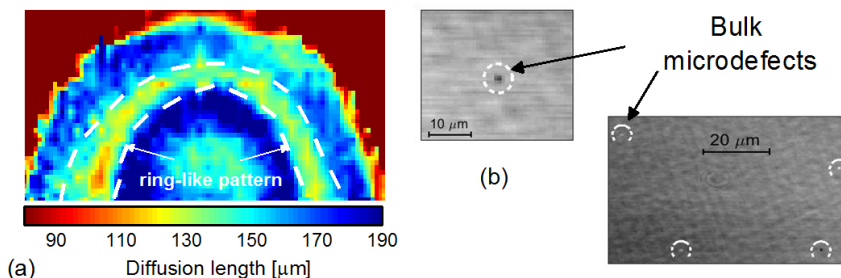


Figure 5.5. (a) Diffusion length map of an implanted specimen measured by SPV after the anneal for activating the implant and recovering the implantation debris. Figure (b) shows the SIRM micrographs obtained from various locations of the wafer.

reduced diffusion length measured before illumination in these implanted specimens. Hence, the results obtained with such implanted specimens are consistent with the hypothesis that, although a fraction of the Cu concentration might have been gettered during the thermal process, the unintentional growth of oxide precipitates increases the sensitiveness of the sample to Cu contamination to the extent that none of the tested gettering treatments are capable of effectively suppressing Cu-LID effects. An alternative explanation for the ineffective suppression of Cu-LID is that the oxide precipitates act as stronger gettering sinks compared to the phosphorus layer, such that no impurity relocation at all takes place during the cooling phase. The repetition of the same Cu-gettering test in samples with intentionally grown oxygen precipitates and more heavily doped emitters may provide additional insights into the reason for the ineffectiveness of gettering in these implanted specimens.

5.5 Implications towards silicon photovoltaics and microelectronics applications

The results presented above provide evidence that Cu-gettering by lightly doped phosphorus layers does not always result in sufficient relocation of Cu impurities from the wafer bulk for suppressing the associated Cu-LID effects. Indeed, while in the specimens with a diffused emitter a significant enhancement of the gettering efficiency was achievable through the addition of a slow cooling tail, none of the tested gettering treatments was found to induce sufficiently strong gettering to inhibit the occurrence of Cu-LID effects. Further investigations into this latter set of sample led to identify precipitated oxygen impurities as the probable cause for the ineffective suppression of Cu-LID in the phosphorus implanted samples.

These results can be interpreted in relation to the general requirements within photovoltaic and microelectronic applications. Specifically, in solar cells the bulk oxygen precipitation is generally considered as an undesirable effect [87, 101–103] and the persistence of relevant bulk Cu concentrations in the gettering experiments described above provides a proof that Cu is not necessarily a benign impurity, which can be driven away from the bulk region during the processing steps for solar cell fabrication.

With regard to integrated circuit manufacturing, an opposite requirement often exists, i.e. the surface region of the wafer becomes of greater import-

tance than the bulk. Hence, in these applications, oxygen precipitates and other intentionally created bulk microdefects become internal gettering sinks that prevent the impurities from harming the device active regions. Within this context, the Cu-LID shall be regarded as a beneficial effect that facilitates the decoration of existing structural defects by interstitial Cu impurities. The possibility of inducing internal gettering of Cu impurities through light-soaking has been discussed in several recent studies (e.g. in Ref. [104] and [105]).

Irrespective of the ultimate application of this study, the results presented above raise the need for deeper understanding of the root cause for the increased Cu-related bulk recombination upon exposure to light-soaking and the development of non-destructive approaches for detecting bulk Cu contamination in silicon samples. Each of these research questions will be addressed in the following chapters.

6. Root cause analysis of Cu-LID

As previously mentioned in Sec. 3.3, the root cause of Cu-LID has long remained unclear. This chapter compiles the main results presented in Publications II-IV, where the defect responsible of Cu-LID has been characterized through lifetime spectroscopy analyses. The aim of these studies is to identify the "fingerprints" of the defect formed during Cu-LID through an extensive analysis of its recombination activity as a function of temperature and injection level. The result of these analyses also enables a discussion on the physical mechanisms behind the light-activation of Cu species.

6.1 Defect characterization in terms of SRH recombination

The expression *lifetime spectroscopy* (LS) represents a set of analytical methods to identify and characterize recombination active defects by fitting experimental lifetime results to the SRH model described in Sec. 2.4 [106]. This is an alternative approach to the so-called *deep level transient spectroscopy* (DLTS) and it comes with the advantage of being an extremely sensitive method without requiring specific sample preparation. The study of the defect properties through DLTS is currently under investigation and further work is required to reliably detect the light-activated Cu defect with this technique.

In this thesis, the characterization of light-activated Cu defects has been carried out through the analysis of injection- and temperature-dependent lifetime data measured in deliberately Cu-contaminated FZ-Si wafers with estimated Fe concentration below 10^{10} cm^{-3} , which gives an estimated background lifetime due to Fe_i species in the millisecond range. Such wafers were also free of any BO-related degradation as depicted in Figure 1 of Publication II.

After saturation of the Cu-related degradation kinetics (see Figure 1 in Publication II) and extraction of the lifetime limited by light-activated copper defects as described in Sec. IV A of Publication II, the resulting injection- and temperature-dependent lifetime curves measured in the range between 25°C and 195°C have been fitted to the SRH recombination model described in Sec. 2.4. As shown in Fig. 6.1, the SRH fit of the entire set of injection- and temperature dependent lifetime curves requires the assumption of two non-interacting energy states, *i.e.*, a deep recombination center, which dominates the lifetime curve in the low to mid-injection regime, and an additional shallow energy level mostly affecting the carrier lifetime towards high injection conditions.

The coexistence of two recombination centres makes the extraction of the real defect parameters more challenging. This is because the assumption of two independent energy levels increases the number of parameters that must be simultaneously determined from the fit of each curve (in total 6, *i.e.* 3 for each recombination center). Furthermore, the optimum fit of the injection-dependent lifetime curves is generally achieved through multiple combinations of the SRH defect parameters. In order to overcome these issues, the defect parameters of the shallow energy state were manually adjusted to fit the entire set of curves in Fig. 6.1 and then kept on fixed values ($E_c - E_t = 0.15 \text{ eV}$ and $k = 0.1$) while determining the true defect parameters of the deep energy state through the deep surface solution

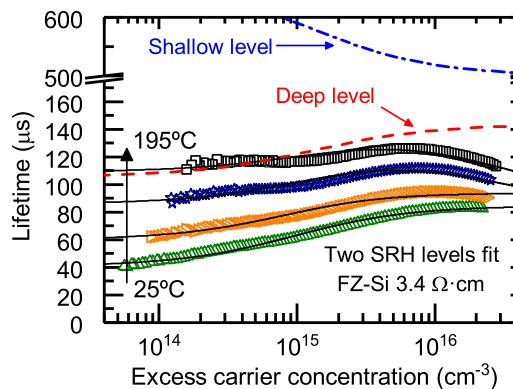


Figure 6.1. SRH fit of the injection-dependent lifetime curves measured at varying temperatures after saturation of the degradation kinetics. The fit of the whole set of injection- and temperature-dependent lifetime curves requires the assumption of two energy levels, *i.e.* a deep level located at $E_c - (0.48 - 0.62) \text{ eV}$ ($k = 1.7 \pm 0.4$) and shallow energy state located at $E_c - 0.15 \text{ eV}$ ($k = 0.1$). (Reprinted with permission from A.Inglese *et al.* *J. Appl. Phys.* **120**, 125703, 2016 - Copyright 2017, AIP Publishing LLC)

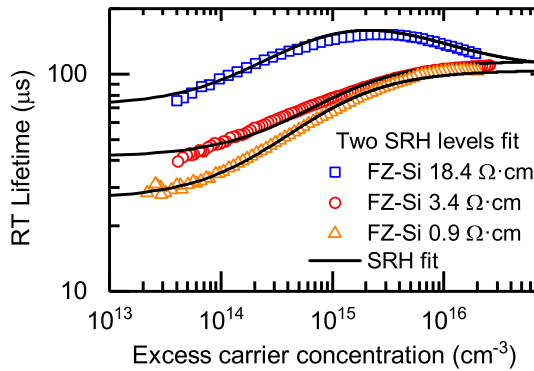


Figure 6.2. Injection dependent lifetime curves measured at room temperatures in Cu-contaminated samples featuring different doping concentrations. The solid line represents the fit obtained assuming two non-interacting SRH levels with the same energy levels and symmetry factors used in Figure 6.1. (Reprinted with permission from A.Inglese *et al.* *J. Appl. Phys.* **120**, 125703, 2016) Copyright 2017, AIP Publishing LLC)

surface (DPSS) approach proposed by Rein *et al.* [106]. The application of the DPSS fit procedure to the experimental data is described in Publication II, where it is shown that the uncertainty on the actual defect parameters associated to the deep energy level can be reduced by extending the DPSS analysis to the whole set of temperature-dependent lifetime curves. On the base of this analysis, it is found that the energy level of the deep recombination center is located between $E_c - 0.48\text{ eV}$ and $E_c - 0.62\text{ eV}$ with symmetry factor $k = 1.7 \pm 0.4$.

As depicted in Fig. 6.2, these defect parameters have been inserted into the SRH equation to fit the injection dependence lifetime curves obtained with wafers with equal Cu contamination levels but different acceptor doping concentrations. With these defect parameters, a good match was obtained between the experimental data and the lifetime data predicted by the SRH model.

6.1.1 Temperature dependence of capture cross sections and verification of previous fit results

In order to further cross-check the results and gain additional insights into the temperature dependence of certain defect parameters, such as the capture cross sections σ_n and σ_p , the SRH fit has been applied to the lifetime results obtained at a fixed injection level ($\Delta n = 1 \times 10^{14} \text{ cm}^{-3}$) over a broader temperature range (83-470°K) than in Publication II (see Sec. IV C). It must be pointed out that at low injection the measured lifetime is

mostly affected by the deep energy state, hence the fit result obtainable from the data shown in Figure 6.3 is referred to this recombination center. As depicted in Figure 6.3(a), if a recombination centre is assumed with energy level near the mid-bandgap ($E_c - E_t = 0.5 \text{ eV}$) and temperature-independent capture cross sections, a notable mismatch is observable between the experimental data and the SRH model. On the other hand, the fit accuracy significantly improves if the position of the deep energy level is maintained near the mid-bandgap and a power-law temperature dependence of the capture cross sections is assumed (for the sample examined in Fig. 6.3, $\sigma_p = \sigma_0 \times T^{-1.1}$).

Figure 6.3(b) reports the fitted SRH parameters from the temperature dependent lifetime data of Figure (a). Under the assumption of temperature-dependent capture cross sections, the fit error is minimized for energy levels in the energy range between $E_c - E_t \simeq 0.2 \text{ eV}$ and $E_c - E_t \simeq 0.6 \text{ eV}$, thus excluding the upper half of the bandgap from the range of energy levels

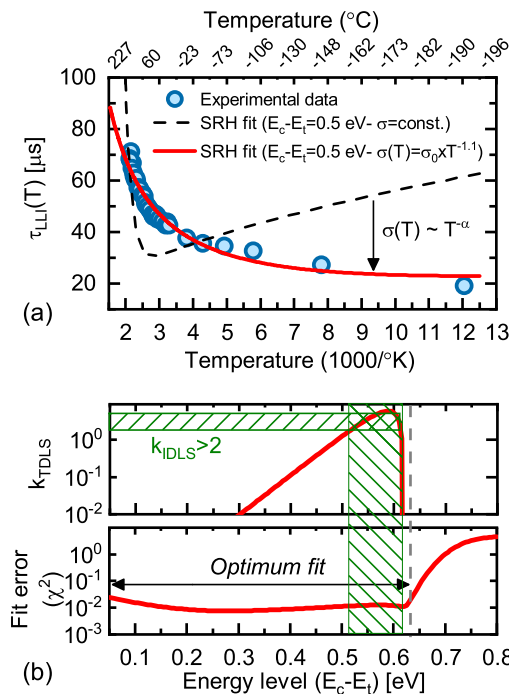


Figure 6.3. SRH fit of temperature-dependent lifetime results measured at fixed injection level ($\Delta n = 1 \times 10^{14} \text{ cm}^{-3}$) on a 1 ppm Cu contaminated FZ sample with $N_a = 1 \times 10^{16} \text{ cm}^{-3}$. Figure (b) displays the DPSS diagrams for the symmetry factor and the corresponding fit error. The green shaded area highlights the domain of energy levels and k factors that are compatible with the fit result of Fig. 6.1.

associated to the recombination center. In addition, it turns out that the fitted values of k -factor for energy levels in the range $0.2 \leq E_c - E_t \leq 0.52 \text{ eV}$ are inconsistent with the fit results from the datasets previously shown in Figure 6.1, which impose $k \simeq 2$. Hence, the SRH fit of the temperature-dependent lifetime data shown in Figure 6.3 confirms that the energy level of the deep recombination centre is presumably located near the mid bandgap with a corresponding k factor between 2 and 6.

Although the ambiguity on the energy level during of the TDLS analysis does not impede the extraction of the defect parameters, the fit result shown in Fig. 6.3(b) raises a discussion as to why the fit error curve features a plateau over a relatively large energy range. While in Publication II this ambiguity of the fit result may be attributable to the narrow temperature range of the lifetime measurements, in Fig. 6.3(b) the extended range of temperatures seems not to significantly improve the ultimate result. Plausible reasons for the ambiguity of the TDLS analysis may be the scarce number of measurement points in Fig. 6.3(b) at very low temperatures or the strong superposed temperature-dependence of capture cross sections.

6.1.2 Comparison with literature data

On the base of the fit results presented above, it can be concluded that the recombination activity of light-activated Cu defects is well described by two non-interacting SRH energy levels, *i.e.*, a shallow energy level at $E_c - E_t \cong 0.15 \text{ eV}$ and a deep recombination center located in the energy range $E_c - E_t = 0.48 - 0.62 \text{ eV}$ with $k \simeq 2.5$ and a strong power-law temperature dependence of the capture cross sections.

Based on the available information on the recombination activity of copper complexes in silicon (see Sec. 3.2), interstitial copper atoms and copper-boron pairs are unlikely to be the defect responsible for Cu-LID, as no recombination activity has been related to such complexes. Hence, the remaining suitable candidates for the light-activated defects are substitutional copper atoms (Cu_s) and copper precipitates.

In early contributions Cu-LID has been hypothesized to stem from the dissociation of a recombination inactive pure copper complex, which was long presumed to be Cu_sCu_i pair, and the subsequent formation of Cu_s complexes [50, 64]. However, this reaction path does not explain the decrease in Cu_i concentration during light-soaking reported in literature [72]. Moreover, no sufficient consistency can be found between the DLTS results for substitutional copper (see Fig. 3.1) and the earlier reported fit results.

Indeed, the energy level reported for Cu_s (*i.e.* $E_v + 0.41 - 0.45\text{ eV}$) lies approximately 100 meV below the value predicted by the injection and temperature-dependent fit results in Fig. 6.1 and 6.3. Furthermore, given the acceptor-like behaviour of the deep energy state, it would be reasonable to expect $k \ll 1$, whereas the LS results suggest a moderate donor-like behaviour for the underlying defect.

Conversely, the fitted energy levels approximately correspond to the boundaries of the energy range associated to Cu precipitates (see Fig. 3.1), thus indicating these extended defects to be the probable root cause of Cu-LID. These considerations are further supported by earlier studies conducted by Macdonald *et al.* [107, 108] on thermally activated Cu precipitates, which led to similar conclusions. However, considering the extended nature of Cu precipitates and the continuous band of the energy states introduced by such defects, a rigorous description of their recombination activity would require more complex models than SRH statistics. In order to gain deeper insights into the defect behind Cu-LID, in the next section the lifetime data has been studied by means of the Schottky model introduced in Sec. 2.5.1.

A final discussion must be dedicated to the initial assumption of two non-interacting SRH energy levels. Several attempts to fit the experimental data under the assumption of a single defect with two associated energy levels (for more information see the appendix of Ref. [109]) failed to produce consistent fit results between the temperature- and injection-dependent analyses. The reason may be found from the fact that the shallow energy levels generally account for "side" effects concurring with the growth of the precipitates (*e.g.* strain caused by the expansion of the precipitate within the host crystal lattice [56]) and are therefore independent of the main recombination channel caused by the copper-related defect.

6.2 Defect characterization in terms of carrier recombination at extended metallic precipitates

In Fig. 6.4 (a), the Schottky model has been fitted to the experimental data corrected from the effect of the recombination channels unrelated to Cu precipitates. The excellent match between the Schottky model and the experimental data provides evidence of Cu precipitates being the dominating recombination active defects. In addition, since the input parameters for the parametrization of the Schottky model are the precipitate radius

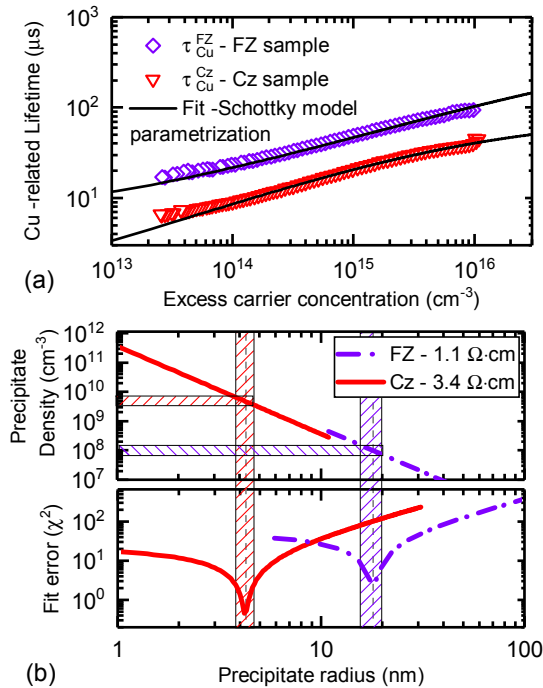


Figure 6.4. (a) Least squares fit of the injection-dependent Cu-related lifetime. The parameters that provide the best fit to the experimental data are shown in (b) where the precipitate density and the corresponding fit error (χ^2) have been calculated for each value of the precipitate radius. The shaded areas define the values of the precipitate radii/densities that minimize the fit error. (Reprinted with permission from A. Inglese, H. Vahlman, W. Kwaplil, J. Schön and H. Saivn *physica status solidi (c)* **14**, 7, 1700103 (2017))

and density (in addition to the semiconductor doping level and the excess carrier concentration) the analysis of the experimental lifetime by means of the Schottky model also provides an estimation of the actual precipitate size and density.

Before analyzing the fit results, it must be pointed out that the application of the Schottky model to the experimental data implies several assumptions that must be *a priori* made, *i.e.*

- i. The entire amount of interstitial Cu atoms transforms into recombination active precipitates;
- ii. All precipitates feature the same size.

Given these assumptions, the precipitate density N_{prec} becomes fixed and it can be written as follows

$$N_{\text{prec}} = \frac{N_{\text{Cu}_i}}{\rho_{\text{Cu}} V_{\text{prec}}} = \frac{N_{\text{Cu}_i}}{\rho_{\text{Cu}} \left(\frac{4}{3}\pi r_{\text{prec}}^3\right)}, \quad (6.1)$$

where $\rho_{\text{Cu}} = 6.52 \times 10^{22} \text{ cm}^{-3}$ is the density of Cu atoms in each precipitate [76]. The fit procedure is based upon a similar approach to the DPSS method, where the precipitate radius is swept across the validity range of the Schottky model (1-100 nm). The values of r_{prec} , together with the calculated values of N_{prec} from Eq. 6.1, are used as input parameters for the recombination model, which gives as an output the lifetime injection dependence. For each combination of the input parameters $N_{\text{prec}}, r_{\text{prec}}$ the displacement between the experimental data and the curve predicted by the Schottky model has been quantified in terms of a squared sum of residuals.

Based on the results shown in Fig. 6.4(b), it turns out that there exist specific combinations of precipitate radii/densities that provide an optimum fit to the experimental data. Particularly, in the case of the FZ-specimen with resistivity in the range of $1.1 \Omega \cdot \text{cm}$ the best fit is obtained with a precipitate radius of $\sim 20 \text{ nm}$ and a density of $\sim 1 \times 10^8 \text{ cm}^{-3}$. On the other hand, the fit to the lifetime curve acquired with the Cz-sample indicates the presence of precipitates with smaller radius ($r_{\text{prec}} \sim 4 \text{ nm}$) and higher density ($N_{\text{prec}} \sim 4 \times 10^9 \text{ cm}^{-3}$).

6.2.1 Temperature dependence of precipitate-limited lifetime

Similarly to the previous SRH-based analysis, the Schottky model has been applied to the temperature-dependent lifetime data measured at fixed level of injection. As depicted in Fig. 6.5, with the values of the precipitate radius and density shown in Fig. 6.4 the Schottky model predicts a lifetime temperature dependence which is in good agreement with the experimental data. Since τ_{Cu} in Fig. 6.5 is calculated according to Eq. 2.15 and no significant precipitate dissolution is likely to occur in the temperature range of the lifetime measurements [74, 110], the increase in the measured lifetime with temperature may only originate from the temperature dependence of the capture cross section and the carrier thermal velocity v_{th} . However, since v_{th} monotonically increases with temperature [111] (and therefore τ_{Cu} would decrease, if σ were temperature independent), the upward trend of the measured lifetime at higher temperatures is solely explainable with precipitate-related capture cross sections becoming smaller at increasing temperature. Hence, such consideration is in agreement with the results presented in Sec. 6.1.1, which indicated a power-law dependence ($\sigma \sim T^{-\alpha}$) of the capture cross section and, hence, smaller capture cross section with increasing temperature.

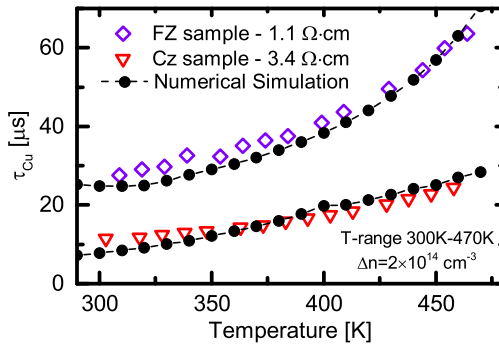


Figure 6.5. Experimental (open symbols) and simulated (filled circles) lifetime data plotted as a function of temperature. Numerical simulations are based on the general formulation of Schottky model, whose mathematical details can be found in appendix A. (Reprinted with permission from A. Inglese, H.Vahlman, W.Kwapil, J.Schön and H.Savin *physica status solidi (c)* **14**, 7, 1700103 (2017))

6.3 Modeling Cu precipitation and comparison with fit results

In the previous sections, the fit of the experimental data in terms of SRH recombination statistics and the Schottky model led to identify Cu precipitates as the defect responsible of Cu-LID. In order to gain deeper understanding into the process that leads to the transformation of interstitial copper atoms into highly recombination active silicides, a comprehensive mathematical model for Cu-LID has been presented in Ref. [112] and Publication IV. The model reproduces the kinetics of precipitate growth and dissolution under illumination and calculates the effect of the growing precipitates on the minority carrier lifetime through the Schottky model. Such modeling work relies on three main assumptions:

- i. Cu precipitates grow/shrink through the addition/release of one atom at a time;
- ii. The driving force for Cu precipitation is the supersaturation level of Cu atoms, i.e. the difference between the actual concentration of interstitial copper species and the solubility limit;
- iii. The precipitate growth is affected by the electrostatic repulsion between positively charged copper ions and the growing Cu_3Si precipitate nuclei. This assumption strictly follows the electrostatic model postulated by Flink *et al.* [113] to explain the densities of interstitial Cu_1^+ atoms that remain in this form at concentrations well above the room temperature solubility limit.

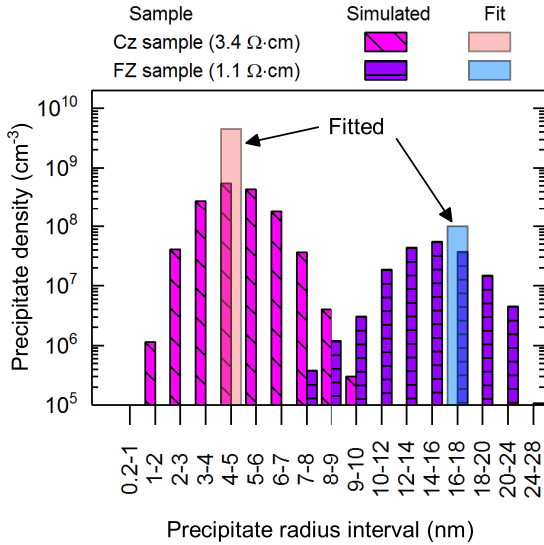


Figure 6.6. Comparison of the fit result from Fig. 6.4 with simulated precipitate size distributions according to the precipitation model (see Ref. [112] and Publication IV).

All mathematical details of this model can be found in Ref. [112]. Once the time evolution of the precipitate size growth has been calculated, the simulation output has been interlinked with the Schottky model, in order to reproduce the effect of the light-activated precipitation process on the lifetime decay.

Publication IV presents an extensive comparison between the experimental lifetime data obtained with differently Cu contaminated samples and the simulation output. The model was able to convincingly reproduce the dependence of the Cu-LID kinetics on a wide range of parameters, such as temperature, doping concentration and light intensity. In this section, we only compare the fit results reported in Sec. 6.2 with the precipitate size and densities predicted by this model.

The simulated precipitate size distributions are plotted in Fig. 6.6 together with the fit results previously presented in Fig. 6.4. Despite the simplifying assumptions that have been made when applying the Schottky model to the experimental injection-dependent lifetime curves (see Sec. 6.2), the fitted precipitate radii and densities are in good agreement with the simulated precipitate size distributions.

Besides confirming the fit results obtained with the Schottky model, the simulated precipitate distributions also highlight a clear dependence of the precipitate size and density on the doping concentration. Specifically, the

model predicts larger precipitates in the specimen featuring lower resistivity (hence higher boron doping concentration). The reason can be found from the increase in Cu solubility with stronger boron doping (i.e. the Fermi level effect on impurity solubility) and its effect on the precipitation process. Indeed, on the base of assumption (ii), the increased Cu solubility implies a weaker driving force for the precipitation process, which ultimately results in the slower descent of precipitate-limited carrier lifetime during illumination (see Fig.6 in Publication III). The enhanced solubility also affects the energetics of precipitate nucleation, as it increases the nucleation barrier, *i.e.* the amount of energy needed for nucleation of new precipitates. The higher nucleation barrier in low-resistivity material renders the nucleation of new precipitates less energetically favourable, such that the precipitation process preferentially continues with the growth of existing nuclei.

In addition to the doping concentration, in the samples previously analysed another factor that might play a role in the Cu-related degradation rates is the different oxygen concentration. Hence, the unintentional precipitation of oxygen species in the Cz-sample during oxidation and subsequent thermal anneals may be partly responsible for the faster degradation observed in these specimens.

7. Fast detection and imaging of copper impurities in crystalline silicon

7.1 The problem of detecting Cu impurities in silicon

Detecting low levels of Cu contamination in silicon is a rather challenging task. The concentration of Cu impurities can be quantitatively detected through chemical analyses, such as inductively-coupled plasma mass spectroscopy (ICP-MS) or secondary ion mass spectrometry (SIMS) but the sensitivity of these techniques is generally limited to rather high impurity concentrations ($> 10^{16} \text{ cm}^{-3}$). Furthermore, these methods are destructive and require the use of expensive equipment which cannot be found in common laboratories. An alternative approach for chemically detecting Cu is the vapor-phase decomposition (VPD) but the sensitivity of this method is solely limited to the wafer surfaces.

Cu concentrations as low as 10^{11} cm^{-3} have been measured through the so-called transient ion drift (TID) [43, 76], which is based on the capacitance transients measurement through DLTS. However, besides being a destructive method, the sample preparation for TID is somewhat challenging and time-consuming, as it requires the formation of metal contacts on both sides of the wafer. In addition, the TID method is solely sensitive to Cu_i species and it provides no information in regards to the spatial distribution of Cu contaminants across the specimen.

On the other hand, the light-induced lifetime degradation caused by Cu contamination represents a characteristic behaviour of this impurity that distinguishes it from the effect of other transition metals. While no lifetime decay has been observed after illumination of Ni- [114] and Cr-contaminated samples [115, 116], the effect of Fe impurities on the minority carrier lifetime is well-known and distinguishable from Cu-LID. Indeed, the dissociation of Fe-acceptor pairs leads to a lifetime decrease only for

levels of injection below the characteristic crossover point [117]. Furthermore at room temperature and under standard illumination conditions the splitting of these pairs often occurs on a different timescale compared to the light-activation of Cu impurities [118, 119]. The Cu-related LID is, therefore, a distinctive feature of this impurity in silicon and lifetime imaging methods become an effective tool for detecting traces of Cu contamination. Leveraging the findings presented in the previous chapter, in this chapter an algorithm will be proposed for detecting and quantitatively imaging the distribution of Cu impurities across the substrate.

7.2 Accelerated Cu-LID

As described in Chapter 5, Cu-LID is a progressive degradation process which occurs in the timespan of several tens of hours under standard illumination conditions (*i.e.* room temperature and illumination intensity ≤ 1 Sun). For quickly detecting Cu contamination in Si, it is important to accelerate the lifetime degradation process, such that the same effect can be achieved within few minutes.

The impact of simultaneous illumination and annealing at 120°C is shown in Fig. 7.1. It can be noticed that, while in the case of room-temperature illumination almost 24 hours are necessary to reach the complete saturation of lifetime degradation, raising the illumination temperature to 120°C reduces the time needed for saturation of the degradation kinetics

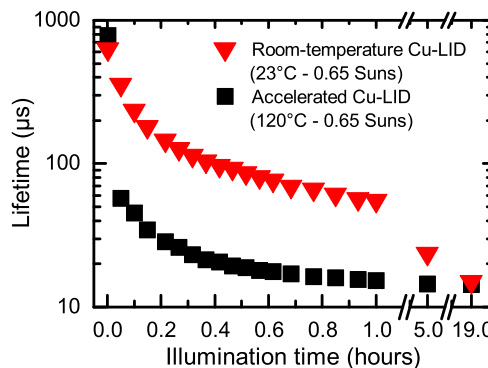


Figure 7.1. Minority carrier lifetime measured at the injection level $\Delta n = 0.1 \times N_a$ as a function of the illumination time in identical Cu-contaminated Cz-wafers during conventional room-temperature illumination and accelerated degradation conditions (reproduced with permission from A.Inglese, J.Lindroos, H.Savin *Applied Physics letters* **107**, 052101, 2015. Copyright 2015, AIP publishing).

up to less than 1 hour. Hence, the presence of Cu impurities can be quickly detected through lifetime measurements carried out before and after a short illumination step at moderately high temperature.

Once LID has been observed, there still remains the problem of distinguishing the effect of copper from other sources, such as the dissociation of Fe-B pairs and the activation of the so-called boron-oxygen defect [74, 120]. For this purpose, Publication V proposes the insertion of short dark anneals above 200°C before and after illumination. The former mainly serves the purpose of dissociating all Fe-B pairs such that no lifetime change is expected from this impurity during the illumination step, whereas the latter allows to distinguish the metastability of the boron-oxygen defect [121] from the non-recoverability of light-activated Cu complexes after such heat treatment (see Sec. 3.3 and Ref. [110]).

Quantitatively estimating the concentration of Cu species

After detecting Cu contamination, the actual concentration of Cu species still needs to be determined. As discussed in Sec. 3.3, the extent of the Cu-related degradation process is proportional to the total Cu contamination level. In Publication V a map of the Cu distribution across an intentionally contaminated specimen was obtained from the empirical formula reported in Ref. [49]

$$N_{Cu-TID} = C_{Cu-TID} \times \sqrt{\frac{1}{\tau_{deg}} - \frac{1}{\tau_{init}}} \quad , \quad (7.1)$$

where the measured Cu concentrations (N_{Cu-TID}) are related to the lifetime measured before and after illumination ($\tau_{deg/init}$) via a fitted pre-factor (C_{Cu-TID}). This approach, however, presents several limitations. First, the applicability of this approach is limited to lifetime results obtained with the μ -PCD method at mid-injection conditions. Second, Eq. 7.1 was extrapolated from intentionally Cu contaminated wafers with a given resistivity ($\sim 20 \Omega \cdot cm$) and measured Cu concentrations between 8×10^{12} and $10^{14} cm^{-3}$, such that a certain error in the estimated concentrations may arise if the same relation is applied to lifetime results obtained from substrates with different resistivity and Cu concentrations outside the aforementioned range. Furthermore, this approach also brings in itself the drawbacks of the μ -PCD method, i.e. relatively long time necessary for lifetime mapping and lower spatial resolution than other methods. In order to overcome these limitations, an alternative approach based on the PL-imaging technique will be proposed in the following section.

7.3 High-resolution imaging of Cu impurities by photoluminescence

As discussed in Chapter 4, the main advantages of the PL-technique are the high spatial resolution and the extremely short time necessary for lifetime mapping. These strengths can be combined with the knowledge gained in the previous chapter in order to quickly obtain spatially resolved information on the distribution of Cu impurities across the silicon specimens.

7.3.1 Change in photoluminescence response during Cu-LID

A deliberately Cu contaminated area of FZ-Si wafers has been exposed to the light emitted by the same laser source used for generating the PL response.

Fig. 7.2 shows an evident decrease in PL-signal due to the light-activation of the copper-related defect. Hence, the PL-imaging setup becomes a viable option for in-line and high-resolution detection of Cu impurities in silicon wafers. Notice that in Fig. 7.2 Cu-LID has been induced at room temperature under an illumination intensity of ~ 1 Sun due to experimental limitations with the measurement setup. On the base of the results discussed above, it is reasonable to expect faster degradation at higher temperature and illumination intensity.

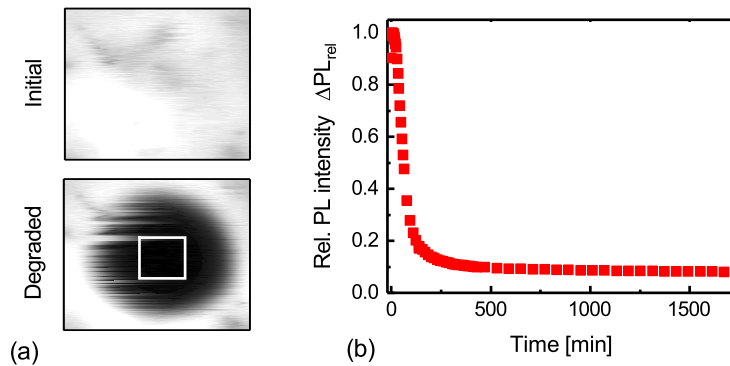


Figure 7.2. Decrease in PL intensity during light-soaking of Cu contaminated regions. Figure (a) shows the raw PL images before and after illumination. Figure (b) plots the relative variation of PL intensity as a function of time. Light-soaking was performed at room temperature under a 1 Sun illumination source.

7.3.2 Calibration and extraction of Cu-related lifetime

In order to apply the concepts described in the previous chapter, the raw PL data must be converted into the corresponding lifetime values. The lifetime injection dependence has been derived by varying the intensity of the laser source and repeating the measurement of the PL response for each level of excitation. The raw data have then been calibrated following the QSSPL-based procedure described in Sec. 4.3.

The lifetime map calibrated from the raw data after saturation of the lifetime decay is shown in Fig. 7.4(a). For each pixel of the lifetime map, the Cu-related lifetime has been calculated as

$$\tau_{Cu}(\Delta n) = \left(\frac{1}{\tau_{deg}(\Delta n)} - \frac{1}{\tau_{init}(\Delta n)} \right)^{-1}, \quad (7.2)$$

where $\tau_{deg}(\Delta n)$ and $\tau_{init}(\Delta n)$ represent the injection dependent lifetime curves measured before and after light soaking, respectively. The application of Eq. 7.2 to the experimental data has a two-fold function: on the one hand it enables the separation of the Cu-limited lifetime from the other recombination channels (Auger, surface, intrinsic, SRH recombination from other impurities etc.) and, on the other, it allows to identify the regions of the wafer affected by Cu-LID. However, it must be pointed out that Eq. 7.2 is an effective way for separating Cu-related recombination from other recombination channels only when (i) the surface passivation is not affected by illumination and (ii) other LID sources (e.g. the boron-oxygen complex) are not superposed to the light activation of Cu species. When many LID mechanisms take place during the light-soaking, additional dark anneals may be necessary for deactivating the boron-oxygen component while maintaining the Cu-related recombination activity nearly unaffected. In order to simplify the discussion of the results that will be hereinafter presented, in the next sections the analysis has been purposely carried out with specimens that are free of other bulk or surface-related LID effects.

7.3.3 Quantitative determination of Cu contamination levels

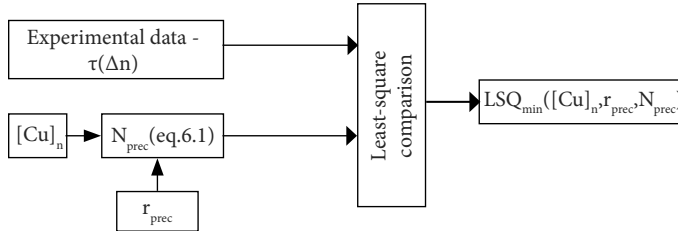
The basic concept for this advanced Cu-imaging method is the analysis of the injection-dependent lifetime results by means of the Schottky model and it follows the same reasoning as previously described in Sec. 6.2. A schematic representation of the procedure for determining the density of Cu contaminants is presented in Fig. 7.3.

The determination of the Cu concentration from injection dependent life-

1. A vector contains a set of randomly chosen Cu concentrations ($[Cu]$)

$$[Cu]_1 \boxed{[Cu]_2} [Cu]_3 \dots [Cu]_n$$

2. For each $[Cu_i]$, the DPSS fit procedure is applied in order to determine the minimum least-square fit error with the given $[Cu]_n$



3. The actual $[Cu_i]$ is pinpointed by the absolute minimum least-square fit error

$$\min \left[\begin{array}{c} LSQ[Cu]_1 \\ LSQ[Cu]_2 \\ \dots \\ LSQ[Cu]_n \end{array} \right] \rightarrow [Cu]_i$$

Figure 7.3. Block diagram representation of the fit procedure for determining the actual Cu contamination level.

time data implies the solution of a reverse problem. Indeed, while in Sec. 6.2 the concentrations of Cu_i atoms were known and represented the starting point for calculating the injection-dependent lifetime curves through the Schottky model, in this case the value of Cu_i must be determined by comparing the output of the Schottky model with the experimental lifetime data. For this purpose, the fit process starts by choosing arbitrary values of Cu_i . For each value of Cu_i , a least square (LSQ) fit routine determines the combination of precipitate size/density that provides the optimum fit to the experimental lifetime curves. The Cu concentration which is closest to the actual contamination level of the wafer is then pinpointed by the value of Cu_i that gives the best match (*i.e.* lowest least-square fit error) between the experimental data and the curves predicted by the recombination model. The concept behind this fit procedure becomes more clear when the algorithm is applied to real experimental data.

Fig. 7.4 describes the application of the abovementioned algorithm to the experimental results obtained after calibrating the raw PL data in Fig. 7.2. The LSQ curve fits are plotted in Fig. 7.4(b) together with τ_{Cu} measured in center of the Cu-spot, where the Cu contamination level is maximum, and in a peripheral region of the Cu spot featuring milder Cu-LID (hence

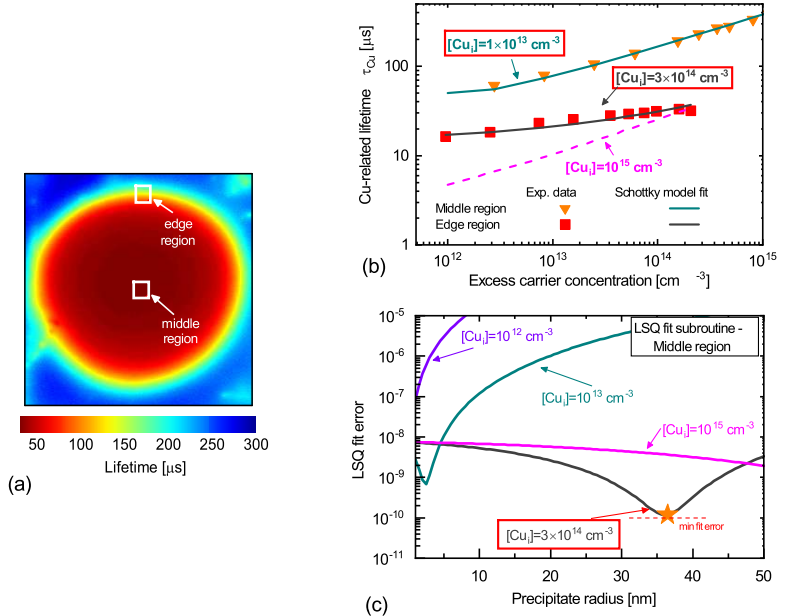


Figure 7.4. Estimation of the Cu contamination level based on the measured lifetime injection dependence. Figure (a) shows the calibrated PL lifetime map of the Cu-spot. τ_{Cu} measured in two different parts of the Cu-spot (middle region and edge) is plotted in figure (b) together with the LSQ fit based on the Schottky model. As an example, the figure presents the application of the fit routine to the lifetime results measured in the middle (black solid line) and at the edge (green solid line) of the Cu-spot. Figure (c) illustrates the principle behind the LSQ fit subroutine.

lower Cu concentration). The subroutine that performs the LSQ curve fit (Fig. 7.4(c)) follows the same logic as the diagram shown in Fig. 6.4, i.e. given a certain value of Cu_i , the optimum combinations of precipitate radii/densities are determined by varying the precipitate radius within the validity range of the model (precipitate radius 1-100 nm).

From Fig. 7.4(b) it can be observed that while in the middle of the Cu spot the optimum LSQ fit is obtained for $[Cu_i] = 3 \times 10^{14} \text{ cm}^{-3}$, at peripheral regions of the contaminated region an accurate fit to the experimental data is obtained assuming considerably lower Cu concentration ($[Cu_i] = 1 \times 10^{13} \text{ cm}^{-3}$). This algorithm, hence, enables the quantification of the Cu contamination level from a simple analysis of the lifetime injection dependence. Iteration of this procedure for each pixel of the PL-image yields the map of the Cu distribution across the wafer, as shown in Fig. 7.5. The figure also displays the detection of a Cu concentration gradient between the middle of the Cu-spot and the edge regions of the Cu-spot. In order to verify the accuracy of these quantitative estimations, it would

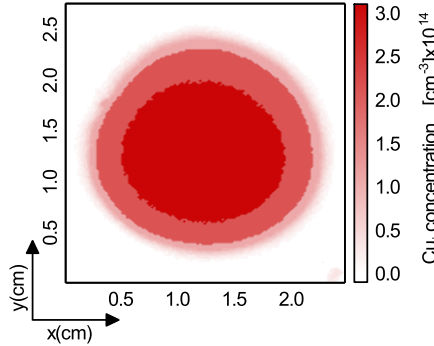


Figure 7.5. Map of the copper distribution across the contaminated region obtained by iterating the fit algorithm illustrated in Fig. 7.4 and Sec. 7.3.3 for each pixel of the PL-lifetime map in Fig. 7.4(a)

be beneficial to compare the estimated Cu concentrations in Fig. 7.5 with direct experimental measurements, for example via TID or ICP-MS. However, it must be pointed out that the estimated Cu concentrations in Fig. 7.5 are in the same order of magnitude as the Cu concentrations reported in previous literature for similarly contaminated wafers (see Publication V and Refs. [49, 76, 122]).

The results presented in Fig. 7.5 also raise a discussion on the detection limits of this method. The lowest Cu concentration detected in Figure 7.5 stands at $[Cu_i] = 8 \times 10^{12} \text{ cm}^{-3}$ and it substantially depends on the background lifetime measured before illumination. This is because the Cu-related degradation process must be sufficiently strong to induce a detectable lifetime decay and enable the accurate determination of τ_{Cu} through Eq. 7.2. With regard to the sample shown in Fig. 7.4, τ_{init} is in the range $300 \mu\text{s}$ (measured at $\Delta n = 1 \times 10^{14} \text{ cm}^{-3}$) and it is presumably limited by surface recombination. Hence, lower detection limits are in principle achievable through the enhancement of surface passivation.

7.3.4 Applicability to multicrystalline silicon

Detecting and determining the actual Cu concentration in multicrystalline material is, in principle, a more challenging task than in monocrystalline samples because of the presence of grain boundaries, dislocations clusters and other structural defects, which provide additional recombination channels for the photogenerated carriers.

In order to test the applicability of this method to multicrystalline silicon, the fit algorithm has been applied to lifetime data obtained with gallium-

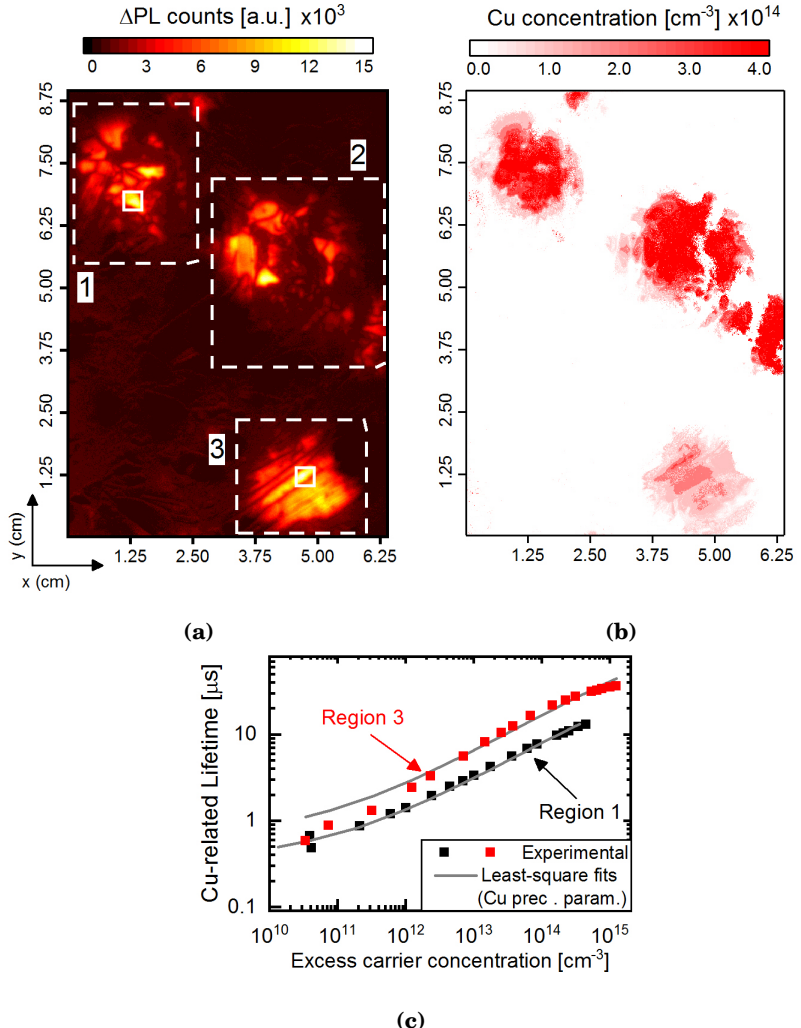


Figure 7.6. Detection of Cu contaminated region through (a) subtraction of raw PL images before and after illumination (20 hours at 1 Sun intensity) and (b) iteration of the fit algorithm described in Sec. 7.3.1 for each pixel of the lifetime-calibrated PL images. In figure (a) the Cu contaminated areas have been labelled with progressive numbers (1-3). Figure (c) displays the fit of the injection-dependent lifetime data measured in rectangles with solid border depicted in figure (a).

doped specimens with resistivity $\sim 2.2 \Omega \cdot \text{cm}$. In these samples, specific regions were intentionally contaminated by means of the same spot-like contamination procedure used for the monocrystalline samples analysed in the previous section.

Fig. 7.6(a) presents the subtracted PL map calculated by subtracting the PL counts before and after light-soaking of the specimen for about 30 hours at room temperature. The Cu contaminated areas clearly result distinguishable from the non-contaminated regions due to the drastic

decrease in PL intensity during illumination (hence larger Δ PL). Notice that in order to highlight the decrement in PL counts during light-soaking the integration time (i.e. the time during which the CCD sensor remains exposed to the PL response) has been kept constant when measuring the PL intensity before and after light-soaking.

Before applying the procedure for determining the actual Cu contamination levels, the raw PL images have been converted into the corresponding lifetime maps and the Cu-related injection dependent lifetime has then been extracted in a similar manner as described in the previous section (see Eq. 7.2).

Despite the higher density of structural defects compared to monocrystalline silicon samples, a good match was found between the experimental data and the lifetime injection dependence predicted the Schottky model (see Fig. 7.6(c)). Furthermore, the application of the fit algorithm reveals estimated Cu contamination levels in all intentionally contaminated regions between $\sim 10^{13} \text{ cm}^{-3}$ and $\sim 4 \times 10^{14} \text{ cm}^{-3}$, thus resulting in the same range as the previous estimations on monocrystalline silicon. It is also possible to distinguish the presence of a concentration gradient between the center of each contaminated region and the edge areas, which is in analogy with the Cu distribution shown in Fig. 7.5. Hence, the fact that (i) the estimated Cu concentrations are similar to the values predicted in Fig. 7.5 and (ii) no modifications to the Schottky model were necessary to obtain a reasonable fit to experimental data provides indications that the method presented in this chapter is capable of reliably detecting and quantifying Cu species also in multicrystalline specimens.

It is noteworthy that, while in Region 3 the subtracted raw PL map outlines a stronger variation of the PL signal compared to the other regions of the wafer, the estimated density of Cu contaminants in this region is lower than in the other intentionally contaminated areas. The reason for this apparent discrepancy is the fact that Region 3 encompasses grains with slightly higher initial lifetime than the rest of the wafer and, therefore, the light-activation of Cu species results in enhanced Δ PL. However during light-soaking, the degradation process saturates to slightly higher lifetime values than in the rest of the wafer, resulting in lower Cu concentrations predicted by the fit procedure.

8. Summary and outlook

The extreme levels of miniaturization of integrated semiconductor devices on one hand and the continuous improvement of solar cell performance on the other, have set increasingly stringent limits on the concentrations of metallic impurities in silicon materials used for microelectronics and photovoltaic applications. Copper is no exception and the Cu-related LID effects render this element particularly insidious for the performance of several silicon-based devices.

In Chapter 5 the effectiveness of phosphorus gettering has been investigated in relation to its effect on the extent of Cu-LID effects. It has been shown that phosphorus gettering does not always prevent the occurrence of Cu-LID. Although the addition of a slow cooling process after the gettering anneal has been proven to significantly enhance the gettering efficiency by POCl_3 -diffused emitters, in a batch of differently processed samples none of the tested gettering schemes was found to effectively suppress Cu-LID. Deeper investigations into this latter set of specimens led to identify oxygen precipitation as the cause for the ineffectiveness of the gettering treatments.

Future studies on this topic may include the testing of competitive gettering schemes with different phosphorus profiles. In addition, further hints on the source of Cu contamination may arise from the analysis of the effect of post-gettering thermal treatments (e.g. the firing steps required for screen-printing the front metal contacts in solar cells) on the distribution of Cu species across the wafer thickness.

Publications II-IV have provided multiple evidence towards Cu precipitation being the root cause behind the observed LID effects. In a first attempt, the recombination activity of the defect responsible of the Cu-LID has been analyzed within the framework provided by SRH recombination statistics. It has been shown that the experimental data are well described

by two energy levels, i.e. a shallow state at $E_c - E_t = 0.1 - 0.2$ eV and a deep recombination center at $E_c - E_t = 0.48 - 0.62$ eV with capture cross section ratio $k = 1.7 - 2.6$, which approximately coincide with the edges of the energy band associated to Cu-precipitates. The same experimental data have then been analysed through a different recombination model specifically developed for describing the recombination activity of metallic precipitates and excellent agreement was found between the predicted lifetime values and the experimental data. Finally, these fit results were compared with the output of a comprehensive physical model that describes the mechanisms behind the light-induced precipitation of interstitial copper atoms. As a final confirmation of the conclusions drawn from this part of the thesis work, future investigations on the defect may include electrical characterization via DLTS and high resolution imaging through scanning infrared (e.g. SIRM) or electron microscopy (e.g. SEM or TEM). However, irrespective of the discussions above on the actual defect behind Cu-LID, the accurate modelling of the injection-dependent lifetime data by means of the aforementioned recombination models provides the necessary information for including the effect of light-activated Cu complexes in advanced simulation software (e.g. PC1D [123] or TCAD Atlas/Sentaurus [124]). Besides shading new light onto the origin of Cu-LID in silicon, these root cause studies also provided a theoretical foundation for addressing the problem of quantitatively detecting the presence of copper contamination through simple lifetime measurements. As LID is a distinguishing characteristic of Cu impurities in silicon, the presence of Cu contamination can be quickly detected by accelerating the LID process through simultaneous illumination and low-temperature annealing. Quantitative high-resolution maps of the Cu spatial distribution were then obtained by comparing the lifetime injection dependence predicted by the Schottky model with experimental lifetime data obtained with deliberately contaminated mono- and multicrystalline silicon specimens.

For the purpose of optimizing the fit procedure, future refinements may include the implementation of advanced machine learning algorithms that minimize the number of iterations required for the least-square fitting process. Furthermore, the application of this method to wafers with high concentrations of oxygen precipitates and bulk microdefects would probably provide additional information on its applicability.

References

- [1] G. Moore, “Cramming more components onto integrated circuits,” *Electronics*, vol. 38, no. 8, 1965.
- [2] E. Mollick, “Establishing Moore’s Law,” *IEEE Annals of the History of Computing*, vol. 28, no. 3, pp. 62–75, 2006.
- [3] Semiconductor Industry Association, “International Technology Roadmap for semiconductors,” tech. rep., 2017.
- [4] D. M. Chapin, C. S. Fuller, and G. L. Pearson, “A New Silicon p-n Junction Photocell for Converting Solar Radiation into Electrical Power,” *Journal of Applied Physics*, vol. 25, no. 5, pp. 676–677, 1954.
- [5] M. A. Green, Y. Hishikawa, W. Warta, E. D. Dunlop, D. H. Levi, J. Hohl-Ebinger, and A. Ho-Bailie, “Solar cell efficiency tables (version 50),” *Progress in Photovoltaics: Research and Applications*, vol. 25, no. 7, pp. 668–676, 2017.
- [6] R. Falster, “Gettering in silicon: fundamentals and recent advances,” *Semiconductor Fabtech, 13th Edition*, 2001.
- [7] M. B. Shabani, T. Yamashita, and E. Morita, “Metallic Impurities in Mono and Multi-crystalline Silicon and Their Gettering by Phosphorus Diffusion,” in *ECS Transactions*, vol. 16, pp. 179–193, 2008.
- [8] A. E. Morishige, M. A. Jensen, J. Hofstetter, P. X. T. Yen, C. Wang, B. Lai, D. P. Fenning, and T. Buonassisi, “Synchrotron-based investigation of transition-metal getterability in n -type multicrystalline silicon,” *Applied Physics Letters*, vol. 108, no. 20, p. 202104, 2016.
- [9] S. Choi, B. Jang, J. Kim, H. Song, and M. Han, “Cu-contamination of single crystalline silicon wafers with thickness of 100 um during multi-wire sawing process,” *Solar Energy*, vol. 125, pp. 198–206, 2016.
- [10] A. Kraft, C. Wolf, J. Bartsch, M. Glatthaar, and S. Glunz, “Long term stability of copper front side contacts for crystalline silicon solar cells,” *Solar Energy Materials and Solar Cells*, vol. 136, pp. 25–31, 2015.
- [11] R. Hoelzl, K. Range, L. Fabry, and D. Huber, “Calibrated Contamination Spiking Method for Silicon Wafers,” *Journal of The Electrochemical Society*, vol. 146, no. 6, p. 2245, 1999.

- [12] E. Grann, A. Huber, J. Grabmeier, R. Holzl, and R. Wahlich, "Silicon Substrate Related Gate Oxide Integrity at Different Oxide Thicknesses," in *Gate Dielectric Integrity: Material, Process, and Tool Qualification*, p. 112, ASTM International, 1999.
- [13] A. A. Istratov, C. Flink, H. Hieslmair, T. Heiser, and E. R. Weber, "Influence of interstitial copper on diffusion length and lifetime of minority carriers in p-type silicon," *Applied Physics Letters*, vol. 71, pp. 2121–2123, oct 1997.
- [14] L. Zhong and F. Shimura, "Dependence of lifetime on surface concentration of copper and iron in silicon wafers," *Applied Physics Letters*, vol. 61, no. 9, pp. 1078–1080, 1992.
- [15] H. Talvitie, A. Haarahiltunen, H. Savin, M. Yli-Koski, M. Asghar, and J. Sinkkonen, "Effect of internal gettering of iron on electrical characteristics of devices," *Materials Science and Engineering: B*, vol. 159-160, pp. 269–273, 2009.
- [16] H. Savin, M. Yli-Koski, and A. Haarahiltunen, "Role of copper in light induced minority-carrier lifetime degradation of silicon," *Applied Physics Letters*, vol. 95, no. 15, p. 152111, 2009.
- [17] J. Lindroos and H. Savin, "Review of light-induced degradation in crystalline silicon solar cells," *Solar Energy Materials and Solar Cells*, vol. 147, pp. 115–126, 2016.
- [18] K. Ramspeck, S. Zimmermann, H. Nagel, A. Metz, Y. Gassenbauer, B. Brikmann, and A. Seidl, "Light induced degradation of Rear Passivated mc-Si solar cells," in *Proceedings of the 27th EUPVSEC 2012*, pp. 861–865, 2012.
- [19] T. Luka, M. Turek, S. Großer, and C. Hagendorf, "Microstructural identification of Cu in solar cells sensitive to light-induced degradation," *physica status solidi (RRL) - Rapid Research Letters*, vol. 11, no. 2, p. 1600426, 2017.
- [20] H. Vahlman, M. Wagner, F. Wolny, A. Krause, H. Laine, A. Inglese, M. Yli-Koski, and H. Savin, "Light-induced degradation in quasi-monocrystalline silicon PERC solar cells: Indications on involvement of copper," *Physica Status Solidi (a)*, vol. 214, no. 7, 2017.
- [21] A. Istratov, C. Flink, H. Hieslmair, S. McHugo, and E. Weber, "Diffusion, solubility and gettering of copper in silicon," *Materials Science and Engineering: B*, vol. 72, no. 2, pp. 99–104, 2000.
- [22] A. Istratov and E. R. Weber, "Physics of Copper in Silicon," *Journal of The Electrochemical Society*, vol. 149, no. 1, p. G21, 2002.
- [23] H. Schlangenotto, H. Maeder, and W. Gerlach, "Temperature dependence of the radiative recombination coefficient in silicon," *Physica Status Solidi (a)*, vol. 21, no. 1, pp. 357–367, 1974.
- [24] J. Dziewior and W. Schmid, "Auger coefficients for highly doped and highly excited silicon," *Applied Physics Letters*, vol. 31, no. 5, pp. 346–348, 1977.
- [25] M. Kerr and A. Cuevas, "General parameterization of Auger recombination in crystalline silicon," *Journal of Applied Physics*, vol. 91, no. 4, p. 2473, 2002.

- [26] W. Shockley and W. T. Read, "Statistics of the Recombinations of Holes and Electrons," *Physical Review*, vol. 87, no. 5, pp. 835–842, 1952.
- [27] R. N. Hall, "Electron-Hole Recombination in Germanium," *Physical Review*, vol. 87, pp. 387–387, jul 1952.
- [28] M. A. Green, "Intrinsic concentration, effective densities of states, and effective mass in silicon," *Journal of Applied Physics*, vol. 67, no. 6, p. 2944, 1990.
- [29] C. Sun, F. E. Rougieux, and D. Macdonald, "Reassessment of the recombination parameters of chromium in n- and p-type crystalline silicon and chromium-boron pairs in p-type crystalline silicon," *Journal of Applied Physics*, vol. 115, no. 21, p. 214907, 2014.
- [30] P. S. Plekhanov and T. Y. Tan, "Schottky effect model of electrical activity of metallic precipitates in silicon," *Applied Physics Letters*, vol. 76, no. 25, pp. 3777–3779, 2000.
- [31] M. D. Negoita and T. Y. Tan, "Metallic precipitate contribution to generation and recombination currents in p-n junction devices due to the Schottky effect," *Journal of Applied Physics*, vol. 94, no. 8, p. 5064, 2003.
- [32] M. D. Negoita and T. Y. Tan, "Metallic precipitate contribution to carrier generation in metal–oxide–semiconductor capacitors due to the Schottky effect," *Journal of Applied Physics*, vol. 95, pp. 191–198, jan 2004.
- [33] W. Kwapisil, J. Schon, W. Warta, and M. C. Schubert, "Carrier Recombination at Metallic Precipitates in p-and n-Type Silicon," *IEEE Journal of Photovoltaics*, vol. 5, no. 5, pp. 1285–1292, 2015.
- [34] W. Kwapisil, J. Schon, F. Schindler, W. Warta, and M. C. Schubert, "Impact of Iron Precipitates on Carrier Lifetime in As-Grown and Phosphorus-Gettered Multicrystalline Silicon Wafers in Model and Experiment," *IEEE Journal of Photovoltaics*, vol. 4, no. 3, pp. 791–798, 2014.
- [35] R. Girisch, R. Mertens, and R. De Keersmaecker, "Determination of Si-SiO₂ interface recombination parameters using a gate-controlled point-junction diode under illumination," *IEEE Transactions on Electron Devices*, vol. 35, no. 2, pp. 203–222, 1988.
- [36] A. B. Sproul, "Dimensionless solution of the equation describing the effect of surface recombination on carrier decay in semiconductors," *Journal of Applied Physics*, vol. 76, no. 5, pp. 2851–2854, 1994.
- [37] R. Bonilla, B. Hoex, P. Hamer, and P. R. Wilshaw, "Dielectric surface passivation for silicon solar cells: A review," *Physica Status Solidi (a)*, vol. 214, no. 7, p. 1700293, 2017.
- [38] R. N. Hall and J. H. Racette, "Diffusion and Solubility of Copper in Extrinsic and Intrinsic Germanium, Silicon, and Gallium Arsenide," *Journal of Applied Physics*, vol. 35, no. 2, p. 379, 1964.
- [39] H. Prigge, P. Gerlach, P. O. Hahn, A. Schnegg, and H. Jacob, "Acceptor Compensation in Silicon Induced by Chemomechanical Polishing," *Journal of The Electrochemical Society*, vol. 138, no. 5, p. 1385, 1991.

- [40] A. A. Istratov, C. Flink, H. Hieslmair, T. Heiser, and E. R. Weber, "Influence of interstitial copper on diffusion length and lifetime of minority carriers in p-type silicon," *Applied Physics Letters*, vol. 71, no. 15, p. 2121, 1997.
- [41] R. S. Muller, T. I. Kamins, and M. Chan, *Device electronics for integrated circuits*. John Wiley & Sons, 2003.
- [42] A. A. Istratov, C. Flink, H. Hieslmair, E. R. Weber, and T. Heiser, "Intrinsic Diffusion Coefficient of Interstitial Copper in Silicon," *Physical Review Letters*, vol. 81, no. 6, pp. 1243–1246, 1998.
- [43] K. Graff, *Metal Impurities in Silicon-Device Fabrication*, vol. 24. Berlin/Heidelberg: Springer, 2000.
- [44] E. Weber, "Transition metals in silicon," *Applied Physics A Solids and Surfaces*, vol. 30, no. 1, pp. 1–22, 1983.
- [45] R. Hözl, L. Fabry, and K. Range, "Gettering efficiencies for Cu and Ni as a function of size and density of oxygen precipitates in p/p- silicon epitaxial wafers," *Applied Physics A Materials Science & Processing*, vol. 73, no. 2, pp. 137–142, 2001.
- [46] A. A. Istratov, H. Hedemann, M. Seibt, O. F. Vyvenko, W. Schröter, T. Heiser, C. Flink, H. Hieslmair, and E. R. Weber, "Electrical and Recombination Properties of Copper-Silicide Precipitates in Silicon," *Journal of The Electrochemical Society*, vol. 145, no. 11, p. 3889, 1998.
- [47] C. Flink, H. Feick, S. A. McHugo, W. Seifert, H. Hieslmair, T. Heiser, A. A. Istratov, and E. R. Weber, "Out-Diffusion and Precipitation of Copper in Silicon: An Electrostatic Model," *Physical Review Letters*, vol. 85, no. 23, pp. 4900–4903, 2000.
- [48] M. B. Shabani, T. Yoshimi, and H. Abe, "Low-Temperature Out-Diffusion of Cu from Silicon Wafers," *Journal of The Electrochemical Society*, vol. 143, no. 6, p. 2025, 1996.
- [49] H. Väinölä, E. Saarnilehto, M. Yli-Koski, A. Haarahiltunen, J. Sinkkonen, G. Berenyi, and T. Pavelka, "Quantitative copper measurement in oxidized p-type silicon wafers using microwave photoconductivity decay," *Applied Physics Letters*, vol. 87, no. 3, p. 032109, 2005.
- [50] W. B. Henley, D. A. Ramappa, and L. Jastrezbski, "Detection of copper contamination in silicon by surface photovoltage diffusion length measurements," *Applied Physics Letters*, vol. 74, no. 2, p. 278, 1999.
- [51] D. A. Ramappa, "Surface photovoltage analysis of phase transformation of copper in p-type silicon," *Applied Physics Letters*, vol. 76, no. 25, p. 3756, 2000.
- [52] S. D. Brotherton, J. R. Ayres, A. Gill, H. van Kesteren, and F. J. A. M. Greidanus, "Deep levels of copper in silicon," *Journal of Applied Physics*, vol. 62, no. 5, p. 1826, 1987.
- [53] H. Lemke, "Substitutional transition metal defects in silicon grown-in by the float zone technique," *Proceedings of the Fourth International Symposium on*, 1996.

- [54] M. Seibt, R. Khalil, V. Kveder, and W. Schröter, "Electronic states at dislocations and metal silicide precipitates in crystalline silicon and their role in solar cell materials," *Applied Physics A*, vol. 96, no. 1, pp. 235–253, 2009.
- [55] D. K. Schroder, "Surface voltage and surface photovoltage: history, theory and applications," *Measurement Science and Technology*, vol. 12, no. 3, pp. R16–R31, 2001.
- [56] M. Seibt, M. Griess, A. A. Istratov, H. Hedemann, A. Sattler, and W. Schröter, "Formation and Properties of Copper Silicide Precipitates in Silicon," *Physica Status Solidi (a)*, vol. 166, no. 1, pp. 171–182, 1998.
- [57] J. Jacobs, B. Hamilton, S. Leonard, V. P. Markevich, and A. R. Peaker, "Nanoprecipitates ... a new recombination model," in *IEEE 42nd Photovoltaic Specialist Conference (PVSC)*, pp. 1–3, IEEE, 2015.
- [58] J. Weber, H. Bauch, and R. Sauer, "Optical properties of copper in silicon: Excitons bound to isoelectronic copper pairs," *Physical Review B*, vol. 25, no. 12, pp. 7688–7699, 1982.
- [59] S. Streicher and A. Carvalho, "The Cu_{PL} defect and the $Cu_{s1}Cu_{i3}$ complex," *Physica B: Condensed Matter*, vol. 407, no. 15, pp. 2967–2969, 2012.
- [60] K. Shirai, H. Yamaguchi, A. Yanase, and H. Katayama-Yoshida, "A new structure of Cu complex in Si and its photoluminescence," *Journal of Physics: Condensed Matter*, vol. 21, no. 6, p. 064249, 2009.
- [61] M. Nakamura, S. Murakami, and H. Udon, "Transformation reactions of copper centers in the space-charge region of a copper-diffused silicon crystal measured by deep-level transient spectroscopy," *Journal of Applied Physics*, vol. 112, no. 6, p. 063530, 2012.
- [62] K. Graff and H. Pieper, "Carrier lifetime measurements on electron-irradiated silicon crystals," *Physica Status Solidi (a)*, vol. 30, no. 2, pp. 593–599, 1975.
- [63] H. Vahlman, A. Haarahiltunen, W. Kwapił, J. Schön, A. Inglese, and H. Savin, "Modeling of light-induced degradation due to Cu precipitation in p-type silicon. II. Comparison of simulations and experiments," *Journal of Applied Physics*, vol. 121, no. 19, p. 195704, 2017.
- [64] I. Tarasov and O.Ostapenko, "Light Induced Defect Reactions in Boron-Doped Silicon: Cu versus Fe," in *8th Workshop on crystalline silicon solar cell material and process*, p. 207, 1998.
- [65] J. Lindroos, M. Yli-Koski, A. Haarahiltunen, M. C. Schubert, and H. Savin, "Light-induced degradation in copper-contaminated gallium-doped silicon," *physica status solidi (RRL) - Rapid Research Letters*, vol. 7, no. 4, pp. 262–264, 2013.
- [66] J. Lindroos, Y. Boulfrad, M. Yli-Koski, and H. Savin, "Preventing light-induced degradation in multicrystalline silicon," *Journal of Applied Physics*, vol. 115, no. 15, p. 154902, 2014.
- [67] T. Turmagambetov, S. Dubois, J. Garandet, B. Martel, N. Enjalbert, J. Veirman, and E. Pihan, "Influence of copper contamination on the illuminated forward and dark reverse current-voltage characteristics of multicrystalline

- p-type silicon solar cells," *Physica Status Solidi (c)*, vol. 11, no. 11-12, pp. 1697–1702, 2014.
- [68] J. Lindroos and H. Savin, "Formation kinetics of copper-related light-induced degradation in crystalline silicon," *Journal of Applied Physics*, vol. 116, no. 23, p. 234901, 2014.
- [69] T. Niewelt, J. Schon, W. Warta, S. W. Glunz, and M. C. Schubert, "Degradation of Crystalline Silicon Due to Boron-Oxygen Defects," *IEEE Journal of Photovoltaics*, vol. 7, no. 1, pp. 383–398, 2017.
- [70] A. Inglese, A. Focareta, F. Schindler, J. Schön, J. Lindroos, M. C. Schubert, and H. Savin, "Light-induced Degradation in Multicrystalline Silicon: The Role of Copper," *Energy Procedia*, vol. 92, pp. 808–814, 2016.
- [71] Y. Boulfrad, J. Lindroos, A. Inglese, M. Yli-Koski, and H. Savin, "Reduction of Light-induced Degradation of Boron-doped Solar-grade Czochralski Silicon by Corona Charging," *Energy Procedia*, vol. 38, pp. 531–535, 2013.
- [72] A. Belayachi, T. Heiser, J. Schunck, and A. Kempf, "Influence of light on interstitial copper in p -type silicon," *Applied Physics A*, vol. 80, no. 2, pp. 201–204, 2005.
- [73] Y. Boulfrad, J. Lindroos, M. Wagner, F. Wolny, M. Yli-Koski, and H. Savin, "Experimental evidence on removing copper and light-induced degradation from silicon by negative charge," *Applied Physics Letters*, vol. 105, no. 18, p. 182108, 2014.
- [74] J. Lindroos, "Copper-related light-induced degradation in crystalline silicon," 2015.
- [75] H. Väinölä, M. Yli-Koski, A. Haarahiltunen, and J. Sinkkonen, "Sensitive Copper Detection in P-type CZ Silicon using μ PCD," *Journal of The Electrochemical Society*, vol. 150, no. 12, p. G790, 2003.
- [76] M. Yli-Koski, *Optical activation of copper in silicon studied by carrier lifetime measurements*. Doctoral dissertation - Helsinki University of Technology, 2004.
- [77] H. Nagel, C. Berge, and A. Aberle, "Generalized analysis of quasi-steady-state and quasi-transient measurements of carrier lifetimes in semiconductors," *Journal of Applied Physics*, vol. 86, p. 6218, 1999.
- [78] R. Sinton, A. Cuevas, and M. Stuckings, "Quasi-steady-state photoconductance, a new method for solar cell material and device characterization," in *25th IEEE Photovoltaic Specialists Conference*, pp. 457–460, IEEE, 1996.
- [79] J. Dorkel and P. Leturcq, "Carrier mobilities in silicon semi-empirically related to temperature, doping and injection level," *Solid-State Electronics*, vol. 24, pp. 821–825, sep 1981.
- [80] D. H. N. Cousins, P. J. and J. E. Cotter, "Experimental verification of the effect of depletion-region modulation on photoconductance lifetime measurements," *Journal of Applied Physics*, no. 95, p. 1854, 2004.

- [81] M. Wilson, P. Edelman, J. Lagowski, S. Olibet, and V. Mihailetschi, "Improved QSS- μ PCD measurement with quality of decay control: Correlation with steady-state carrier lifetime," *Solar Energy Materials and Solar Cells*, vol. 106, pp. 66–70, 2012.
- [82] J. A. Giesecke, M. C. Schubert, D. Walter, and W. Warta, "Minority carrier lifetime in silicon wafers from quasi-steady-state photoluminescence," *Applied Physics Letters*, vol. 97, no. 9, 2010.
- [83] T. Trupke and R. A. Bardos, "Self-consistent determination of the generation rate from photoconductance measurements," *Applied Physics Letters*, vol. 85, no. 16, pp. 3611–3613, 2004.
- [84] T. Trupke, R. A. Bardos, and M. D. Abbott, "Self-consistent calibration of photoluminescence and photoconductance lifetime measurements," *Applied Physics Letters*, vol. 87, no. 18, p. 184102, 2005.
- [85] J. Giesecke, M. Schubert, B. Michl, F. Schindler, and W. Warta, "Minority carrier lifetime imaging of silicon wafers calibrated by quasi-steady-state photoluminescence," *Solar Energy Materials and Solar Cells*, vol. 95, no. 3, pp. 1011–1018, 2011.
- [86] T. Trupke, R. A. Bardos, M. C. Schubert, and W. Warta, "Photoluminescence imaging of silicon wafers," *Applied Physics Letters*, vol. 89, p. 044107, jul 2006.
- [87] J. Haunschmid, M. Glatthaar, M. Demant, J. Nievendick, M. Motzko, S. Rein, and E. R. Weber, "Quality control of as-cut multicrystalline silicon wafers using photoluminescence imaging for solar cell production," *Solar Energy Materials and Solar Cells*, vol. 94, no. 12, pp. 2007–2012, 2010.
- [88] L. Kronik and Y. Shapira, "Surface photovoltage phenomena: theory, experiment, and applications," *Surface Science Reports*, vol. 37, no. 1-5, pp. 1–206, 1999.
- [89] D. K. Schroder, "Semiconductor material and device characterization," pp. 439–448, 2006.
- [90] W. M. Bullis, "Interpretation of Carrier Recombination Lifetime and Diffusion Length Measurements in Silicon," *Journal of The Electrochemical Society*, vol. 143, no. 4, p. 1399, 1996.
- [91] J. Lagowski, A. M. Kontkiewicz, L. Jastrzebski, and P. Edelman, "Method for the measurement of long minority carrier diffusion lengths exceeding wafer thickness," *Applied Physics Letters*, vol. 63, no. 21, pp. 2902–2904, 1993.
- [92] W. Schröter, M. Seibt, and D. Gilles, "High-Temperature Properties of Transition Elements in Silicon," in *Materials Science and Technology*, Weinheim, Germany: Wiley-VCH Verlag GmbH & Co. KGaA, 2013.
- [93] R. Hoelzl, K. Range, and L. Fabry, "Comparison of different gettering techniques for Cu- p+ versus polysilicon and oxygen precipitates," *Applied Physics A: Materials Science & Processing*, vol. 75, no. 5, pp. 591–595, 2002.

- [94] R. Hoelzl, K.-J. Range, and L. Fabry, "Modeling of Cu gettering in p- and n-type silicon and in poly-silicon," *Applied Physics A: Materials Science & Processing*, vol. 75, no. 4, pp. 525–534, 2002.
- [95] SEMI PV Group, "International Technology Roadmap for Photovoltaic (Seventh Edition)," tech. rep., 2016.
- [96] H. Li, K. Kim, B. Hallam, B. Hoex, S. Wenham, and M. Abbott, "POCl₃ diffusion for industrial Si solar cell emitter formation," *Frontiers in Energy*, vol. 11, no. 1, pp. 42–51, 2017.
- [97] P. Ostoja, S. Guerri, P. Negrini, and S. Solmi, "The effects of phosphorus precipitation on the open-circuit voltage in N+/P silicon solar cells," *Solar Cells*, vol. 11, pp. 1–12, feb 1984.
- [98] B. Bazer-Bachi, E. Fourmond, P. Papet, L. Bouzaas, O. Nichiporuk, N. Le Quang, and M. Lemiti, "Higher emitter quality by reducing inactive phosphorus," *Solar Energy Materials and Solar Cells*, vol. 105, pp. 137–141, 2012.
- [99] A. Borghesi, B. Pivac, A. Sassella, and A. Stella, "Oxygen precipitation in silicon," *Journal of Applied Physics*, vol. 77, no. 9, pp. 4169–4244, 1995.
- [100] G. Kissinger, "Oxygen Precipitation in Silicon," pp. 273–341, Springer, Tokyo, 2015.
- [101] J. D. Murphy, K. Bothe, M. Olmo, V. V. Voronkov, and R. J. Falster, "The effect of oxide precipitates on minority carrier lifetime in p-type silicon," *Journal of Applied Physics*, vol. 110, no. 5, p. 053713, 2011.
- [102] J. Murphy, R. McGuire, K. Bothe, V. Voronkov, and R. Falster, "Minority carrier lifetime in silicon photovoltaics: The effect of oxygen precipitation," *Solar Energy Materials and Solar Cells*, vol. 120, pp. 402–411, 2014.
- [103] K. Youssef, M. Shi, C. Radue, E. Good, and G. Rozgonyi, "Effect of oxygen and associated residual stresses on the mechanical properties of high growth rate Czochralski silicon," *Journal of Applied Physics*, vol. 113, no. 13, p. 133502, 2013.
- [104] G. Kissinger, D. Kot, M. A. Schubert, A. Sattler, and T. Müller, "Internal Gettering of Copper for Microelectronic Applications," *Solid State Phenomena*, vol. 242, pp. 236–245, 2015.
- [105] D. Kot, G. Kissinger, M. Schubert, T. Müller, and A. Sattler, "Impact of RTA on the Morphology of Oxygen Precipitates and on the Getter Efficiency for Cu and Ni in Si Wafers," *Materials Science Forum*, vol. 725, pp. 239–242, 2012.
- [106] S. Rein, *Lifetime Spectroscopy*. Springer Series in Material Science, Berlin/Heidelberg: Springer-Verlag, 2005.
- [107] D. Macdonald, A. Cuevas, S. Rein, P. Lichtner, and S. W. Glunz, *Temperature- and injection-dependent lifetime spectroscopy of copper-related defects in silicon*, vol. 1. IEEE, 2003.

- [108] D. Macdonald, W. Brendle, A. Cuevas, and A. Istratov, “Injection-Dependent Lifetime Studies of Copper Precipitates in Silicon,” in *Proceedings of the Workshop on Crystalline Silicon Solar Cell Materials and Processes*, pp. 201–204, 2002.
- [109] J. D. Murphy, K. Bothe, R. Krain, V. V. Voronkov, and R. J. Falster, “Parameterisation of injection-dependent lifetime measurements in semiconductors in terms of Shockley-Read-Hall statistics: An application to oxide precipitates in silicon,” *Journal of Applied Physics*, vol. 111, no. 11, p. 113709, 2012.
- [110] H. Vahlman, A. Haarahiltunen, W. Kwapił, J. Schön, M. Yli-Koski, A. Inglese, C. Modanese, and H. Savin, “Effect of low-temperature annealing on defect causing copper-related light-induced degradation in p-type silicon,” *Energy Procedia*, vol. 124, pp. 188–196, 2017.
- [111] S. Rein, T. Rehrl, W. Warta, and S. W. Glunz, “Lifetime spectroscopy for defect characterization: Systematic analysis of the possibilities and restrictions,” *Journal of Applied Physics*, vol. 91, no. 3, pp. 2059–2070, 2002.
- [112] H. Vahlman, A. Haarahiltunen, W. Kwapił, J. Schön, A. Inglese, and H. Savin, “Modeling of light-induced degradation due to Cu precipitation in p-type silicon. I. General theory of precipitation under carrier injection,” *Journal of Applied Physics*, vol. 121, no. 19, p. 195703, 2017.
- [113] C. Flink, H. Feick, S. A. McHugo, W. Seifert, H. Hieslmair, T. Heiser, A. A. Istratov, and E. R. Weber, “Out-Diffusion and Precipitation of Copper in Silicon: An Electrostatic Model,” *Physical Review Letters*, vol. 85, no. 23, pp. 4900–4903, 2000.
- [114] H. Savin, M. Yli-Koski, A. Haarahiltunen, H. Talvitie, and J. Sinkkonen, “Detection of Nickel in Silicon by Recombination Lifetime Measurements,” *Solid State Phenomena*, vol. 131-133, pp. 183–188, 2008.
- [115] S. Dubois, O. Palais, and P. J. Ribeyron, “Determination at 300K of the hole capture cross section of chromium-boron pairs in p-type silicon,” *Applied Physics Letters*, vol. 89, no. 23, p. 232112, 2006.
- [116] H. Habenicht, M. C. Schubert, and W. Warta, “Imaging of chromium point defects in p-type silicon,” *Journal of Applied Physics*, vol. 108, no. 3, p. 034909, 2010.
- [117] D. Macdonald, J. Tan, and T. Trupke, “Imaging interstitial iron concentrations in boron-doped crystalline silicon using photoluminescence,” *Journal of Applied Physics*, vol. 103, no. 7, p. 073710, 2008.
- [118] L. J. Geerligs and D. Macdonald, “Dynamics of light-induced FeB pair dissociation in crystalline silicon,” *Applied Physics Letters*, vol. 85, no. 22, pp. 5227–5229, 2004.
- [119] C. Möller, T. Bartel, F. Gibaja, and K. Lauer, “Iron-boron pairing kinetics in illuminated p-type and in boron/phosphorus co-doped n-type silicon,” *Journal of Applied Physics*, vol. 116, no. 2, p. 024503, 2014.
- [120] T. Niewelt, J. Schon, W. Warta, S. W. Glunz, and M. C. Schubert, “Degradation of Crystalline Silicon Due to Boron–Oxygen Defects,” *IEEE Journal of Photovoltaics*, vol. 7, no. 1, pp. 383–398, 2017.

- [121] S. W. Glunz, S. Rein, J. Y. Lee, and W. Warta, “Minority carrier lifetime degradation in boron-doped Czochralski silicon,” *Journal of Applied Physics*, 2001.
- [122] M. Yli-Koski, H. Väinölä, A. Haarahiltunen, J. Storgårds, E. Saarnilehto, and J. Sinkkonen, “Light Activated Copper Defects in P-Type Silicon Studied by PCD,” *Physica Scripta*, vol. 114, pp. 69–72, 2004.
- [123] D. Clugston and P. Basore, “PC1D version 5: 32-bit solar cell modeling on personal computers,” in *Conference Record of the Twenty Sixth IEEE Photovoltaic Specialists Conference - 1997*, pp. 207–210, 1998.
- [124] Synopsys Inc., “TCAD Sentaurus Manual,” tech. rep., Mountain View (CA), 2015.

Appendix: Detailed mathematical description of the Schottky junction model

General mathematical formulation

Note: Unless otherwise stated, the calculations included in this section follow the same sign and symbol conventions as in Fig. 2.2.

The magnitude of the built-in voltage of a metal-semiconductor Schottky junction in thermal equilibrium is

$$\Psi_n^S = \Phi_{Bp} - \frac{E_f - E_v}{e}, \quad (\text{A.1})$$

where Φ_{Bp} is the energy barrier height, E_f is the Fermi level and E_v is the valence band minimum.

Under carrier injection, the calculation of the band bending at metal semiconductor interface requires the numerical solution of the Poisson equation together with the continuity equations for holes and electrons. Specifically, the continuity equations are expressed as

$$\nabla \cdot J_e = -eG \quad , \quad \nabla \cdot J_h = eG, \quad (\text{A.2})$$

where G is the generation rate, whereas J_e and J_h are the electron and hole current densities. For these quantities the drift-diffusion equations hold, i.e.

$$J_e = e\mu_e n E + eD_e \nabla n \quad , \quad J_p = e\mu_p p E - eD_p \nabla p. \quad (\text{A.3})$$

The Poisson's equation is expressed as

$$\nabla^2 \Psi_n = -\frac{e(p - n + [\text{Cu}_i^+] - N_a^-)}{\epsilon_{Si}}, \quad (\text{A.4})$$

where Ψ_n is the electric potential around a given precipitate, $E = -\nabla \cdot \Phi_n$ is the electric field, p and n are hole and electron concentrations, N_a^- is the negative acceptor concentration, ϵ_{Si} is the permittivity of silicon. The

concentrations of electrons and holes obey the Fermi-Dirac statistics and, on the base of the adopted symbol conventions are expressed as

$$n = n_i \exp\left(\frac{e\Psi_n + E_{Fn} - E_i^{bulk}}{k_B T}\right) \quad p = n_i \exp\left(\frac{E_i^{bulk} - E_{Fp} - e\Psi_n}{k_B T}\right), \quad (\text{A.5})$$

where n_i defines the intrinsic electron concentration and $E_{fn,p}$ are the quasi Fermi levels for holes and electrons respectively.

As mentioned in Sec. 2.5.1, the boundary condition for the solution of the Poisson's equation together with the continuity equations is $J_e^S = -J_h^S$ [30, 31], where the thermionic emission currents at the metal/semiconductor interface are

$$J_e^S = J_e^{sat} \left(\exp\left(\frac{E_{Fn}^S - E_F^M}{k_B T}\right) - 1 \right) \quad (\text{A.6})$$

$$J_h^S = -J_h^{sat} \left(\exp\left(\frac{E_F^M - E_{Fn}^S}{k_B T}\right) - 1 \right). \quad (\text{A.7})$$

After several calculations and rearrangements, the boundary condition translates into the following expression of the built-in potential

$$\Psi_n^S = \frac{k_B T}{e} \cdot \log \left(\frac{J_e^{sat} - J_h^{sat} + \sqrt{(J_e^{sat} - J_h^{sat})^2 + 4J_e^{sat}J_h^{sat} \exp\left(\frac{E_{Fn}^S - E_{Fp}^S}{k_B T}\right)}}{2J_e^{sat} \frac{n_i}{N_c} \exp\left(\frac{E_G - e\Phi_{Bp} + E_{Fn}^S - E_i^{bulk}}{k_B T}\right)} \right). \quad (\text{A.8})$$

The recombination rate at the precipitate is then calculated through Eq. 2.14 introduced in Sec. 2.5.1.

Parametrization of the Schottky model

The general formulation of the Schottky model implies the numerical solution of the Poisson's equation together with the continuity equations, which must provide a self-consistent determination of Ψ_n (i.e. this solution must solve all equations at once). The solution of the problem becomes computationally demanding when the concepts introduced above are applied to 2D and 3D simulations. In addition, when simulating the recombination rate at varying levels of injection, the calculation has to be repeated for each excess carrier concentration. In order to ease the determination of the recombination rate, Kwapisil *et al.* [33] proposed a system of equations that allows to determine the lifetime injection dependence from certain input parameters, i.e. r_{prec} , N_{prec} and the semiconductor doping N_a . The calculation of the precipitate-limited lifetime is based upon the relation

$$\tau_{\text{prec}}(\Delta n, N_{\text{prec}}, r_n, N_A) = \frac{1}{v_{th} N_{\text{prec}} \sigma_{\text{prec}}(\Delta n, r_n, N_a)}, \quad (\text{A.9})$$

where the dependence of σ_{prec} on the precipitate radius, semiconductor doping and excess carrier concentration is estimated via the equations listed below

$$\frac{\sigma_{\text{prec}}}{r_{\text{prec}}^2} = \sigma_{\min} + \frac{\sigma_{\max} - \sigma_{\min}}{1 + \left(\frac{\Delta n}{\Delta n_{\text{ref}}}\right)^{\alpha}} \quad (\text{A.10})$$

$$\sigma_{\min} = \sigma_{\min}^{\min} + \frac{\sigma_{\max}^{\min} - \sigma_{\min}^{\min}}{1 + \left(\frac{r_{\text{prec}}}{r_{\text{ref}}^{\min}}\right)^{\alpha^{\min}}} \quad (\text{A.11})$$

$$\sigma_{\max} = \sigma_{\min}^{\max} + \frac{\sigma_{\max}^{\max} - \sigma_{\min}^{\max}}{1 + \left(\frac{r_{\text{prec}}}{r_{\text{ref}}^{\max}}\right)^{\alpha^{\max}}} \quad (\text{A.12})$$

$$\Delta n_{\text{ref}} = 10^{(a+b[r_{\text{prec}}/1\text{ nm}]^c)} \quad (\text{A.13})$$

$$\alpha = A + \exp(-C \cdot [r_{\text{prec}}/1\text{ nm}]). \quad (\text{A.14})$$

The following functions define the dependence on the acceptor doping concentration N_A

$$\sigma_{\min}^{\min} = \text{const.}, \quad \sigma_{\min}^{\max} = \text{const.} \quad (\text{A.15})$$

$$\sigma_{\max}^{\min} = \sigma_{\max,0}^{\min} + \sigma_{\max,1}^{\min} \cdot \exp(-\sigma_{\text{msx},2} \cdot [N_A/1\text{ cm}^{-3}]) \quad (\text{A.16})$$

$$r_{\text{ref}}^{\min} = r_{\text{ref},0}^{\min} + r_{\text{ref},1}^{\min} \cdot [N_A/1\text{ cm}^{-3}] \quad (\text{A.17})$$

$$\sigma_{\max}^{\max} = \sigma_{\max,0}^{\max} + \sigma_{\max,1}^{\max} \cdot \exp(-\sigma_{\text{msx},2} \cdot [N_A/1\text{ cm}^{-3}]) \quad (\text{A.18})$$

$$r_{\text{ref}}^{\max} = r_{\text{ref},0}^{\max} + r_{\text{ref},1}^{\max} \cdot [N_A/1\text{ cm}^{-3}] \quad (\text{A.19})$$

$$\alpha^{\max} = \alpha_0^{\max} \cdot [N_A/1\text{ cm}^{-3}] \quad (\text{A.20})$$

$$a = a_0^{\max} + a_1 \cdot [N_A/1\text{ cm}^{-3}]^{a_2} \quad (\text{A.21})$$

$$b = b_0^{\max} \cdot [N_A/1\text{ cm}^{-3}]^{b_1} \quad (\text{A.22})$$

$$c = c_0^{\max} \cdot [N_A/1\text{ cm}^{-3}]^{c_1} \quad (\text{A.23})$$

$$A = A_0 \cdot [N_A/1\text{ cm}^{-3}]^{A_1} \quad (\text{A.24})$$

$$B = B_0 + B_1 \cdot \exp(-B_2 \cdot [N_A/1\text{ cm}^{-3}]) \quad (\text{A.25})$$

$$C = C_0 + C_1 \cdot \exp(-C_2 \cdot [N_A/1\text{ cm}^{-3}]). \quad (\text{A.26})$$

The constant values have been fitted in Ref. [33] from simulation results and reported in the table below. Notice that the values reported in the table hold only for *p*-type silicon).

Symbol	Value	Symbol	Value
σ_{min}^{min}	0.3	a_0	11.02711
$\sigma_{max,0}^{min}$	0.30037	$\sigma_{max,1}^{min}$	1.57
$\sigma_{max,2}^{min}$	$7.1 \cdot 10^{-17}$	$r_{ref,0}^{min}$	1.08186
$r_{ref,1}^{min}$	$3.16 \cdot 10^{-16}$	α_0^{min}	18.46
α_1^{min}	66.83429	α_2^{min}	$9.26 \cdot 10^{-16}$
σ_{min}^{max}	0.38	$\sigma_{max,0}^{max}$	-4550
$\sigma_{max,1}^{max}$	2460	$\sigma_{max,2}^{max}$	0.019
$r_{ref,0}^{max}$	1.215	$r_{ref,1}^{max}$	$8.78 \cdot 10^{-20}$
α_0^{max}	8876920	α_1^{max}	-0.40128
a_0	11.02	a_1	-0.00777
a_2	0.14313	b_0	$2.69 \cdot 10^{-5}$
b_1	0.29433	c_0	2.7833
c_1	-0.06212	A_0	154.65447
A_1	-0.16677	B_0	0.25835
B_1	-0.18501	B_2	$2.86 \cdot 10^{-17}$
C_0	0.03771	C_1	-0.03102
C_2	$4.08 \cdot 10^{-18}$		

Publication I

A.Inglese, H.Laine, V.Vähäniemi, H.Savin. Cu-gettering by phosphorus-doped emitters in *p*-type silicon: Effect on light-induced degradation. *AIP Advances*, 8, 015112, 2018.

© 2018 American Institute of Physics Publishing LLC.

Reprinted with permission.

Cu gettering by phosphorus-doped emitters in p-type silicon: Effect on light-induced degradation

Alessandro Inglese,^a Hannu S. Laine, Ville Vähänissi, and Hele Savin

*Department of Electronics and Nanoengineering, Aalto University, Tietotie 3,
02150 Espoo, Finland*

(Received 7 November 2017; accepted 29 December 2017; published online 10 January 2018)

The presence of copper (Cu) contamination is known to cause relevant light-induced degradation (Cu-LID) effects in p-type silicon. Due to its high diffusivity, Cu is generally regarded as a relatively benign impurity, which can be readily relocated during device fabrication from the wafer bulk, i.e. the region affected by Cu-LID, to the surface phosphorus-doped emitter. This contribution examines in detail the impact of gettering by industrially relevant phosphorus layers on the strength of Cu-LID effects. We find that phosphorus gettering does not always prevent the occurrence of Cu-LID. Specifically, air-cooling after an isothermal anneal at 800°C results in only weak impurity segregation to the phosphorus-doped layer, which turns out to be insufficient for effectively mitigating Cu-LID effects. Furthermore, we show that the gettering efficiency can be enhanced through the addition of a slow cooling ramp (-4°C/min) between 800°C and 600°C, resulting in the nearly complete disappearance of Cu-LID effects. © 2018 Author(s). All article content, except where otherwise noted, is licensed under a Creative Commons Attribution (CC BY) license (<http://creativecommons.org/licenses/by/4.0/>). <https://doi.org/10.1063/1.5012680>

I. INTRODUCTION

Copper (Cu) is an abundant and deleterious $3d$ metal impurity in photovoltaic grade crystalline silicon. Besides being present in significant concentrations in the as-grown feedstock material,^{1–4} additional sources of Cu contamination are wafer sawing⁵ and the use of cost-effective Cu alloys for contacts and interconnects. The presence of parasitic Cu contamination is known to progressively deteriorate the bulk minority carrier lifetime during exposure to illumination.⁶ This phenomenon is referred in literature to as copper-related light-induced degradation (Cu-LID) and recent root-cause investigations have proven that Cu-LID arises from the transformation of interstitial Cu atoms into highly recombination active precipitates in the bulk region of the wafer.^{7–10}

Gettering is a well-established technique, by which transition metal impurities are relocated to pre-defined substrate areas where they result less harmful for the device performance. In devices where the wafer bulk represents the region of major relevance for the device performance (*e.g.* solar cells), the gettering effect is usually achieved by creating a phosphorus-doped surface layer where metal impurities naturally tend to relocate during the high-temperature steps required for device fabrication.

Because of its high diffusivity in silicon,¹¹ Cu is generally regarded as an easily getterable impurity and, for this reason, little information exists on its actual getterability during device processing. Shabani *et al.* reported a decrement of the bulk Cu concentration by several orders of magnitude after diffusing heavily doped emitters with peak phosphorus concentration up to $\sim 8 \times 10^{21} \text{ cm}^{-3}$ and subjecting the samples to various gettering anneals.^{3,12} However, in state-of-the-art solar cells, it has become desirable to reduce the doping level of the emitter¹³ because excessive dopant concentrations lead to the formation of an electrically inactive layer (often called “dead layer”),^{14,15} increased

^aE-mail: alessandro.inglese@aalto.fi

emitter saturation current and Auger recombination,^{16,17} with negative implications on the maximum achievable conversion efficiency. On the other hand, the choice of light emitter doping also weakens the driving force for the segregation of metallic impurities to the phosphorus-doped region, such that the benefits arising from light doping may be counterbalanced by the incomplete gettering of several metallic impurities, including Cu, as indicated by recent observations of Cu-related LID in industrial silicon solar cells.^{18,19} It is therefore crucial to investigate the impact of gettering by lightly doped emitters on the strength of Cu-LID effects.

In this contribution, we test the getterability of Cu impurities with an industrially relevant phosphorus emitter and we assess the effectiveness of the gettering treatments by directly monitoring the Cu-LID effects caused by residual bulk Cu contamination after gettering. The aim of this study is (i) to assess whether bulk Cu contamination is controllable by lightly doped emitters to the extent that Cu-LID effects are fully inhibited and (ii) evaluate the impact of different gettering temperature profiles on the resulting Cu-LID effects.

II. EXPERIMENTAL

The experiments were performed on electronic grade, 4-in., boron-doped, Czochralski-grown silicon with resistivity of 3.4–3.9 Ω cm, thickness of 380 ± 15 μm , and oxygen concentration ≥ 14.5 ppm. A schematic representation of the experimental processing steps is shown in Figure 1. After standard RCA cleanings, the wafers were oxidized in wet ambient at 1000°C for 84 min, which resulted in the growth of a 440 nm thick oxide layer. Some wafers were then kept as reference samples, while the rest of the batch was subjected to the formation of the phosphorus-doped region. Before dopant diffusion, the thermal oxide at the front side of the wafer was etched off, while the backside oxide layer was kept as a barrier for dopant diffusion. The emitter was then formed by depositing a phosphosilicate glass (PSG) via a phosphorus oxychloride (POCl_3) process and then diffusing the dopant at 830°C for 20 minutes followed by a 5 min anneal in oxidizing ambient. Next, the PSG was removed in a HF:DIW solution (1:50) and the sheet resistance of the phosphorus layer was measured with a four-point probe to be $\sim 80 \Omega \text{ sq}^{-1}$. Electrochemical Capacitance-Voltage (ECV) measurements performed on similarly processed wafers also indicated a peak electrically active phosphorus concentration of $\sim 2 \times 10^{20} \text{ cm}^{-3}$ and a junction depth of $\sim 0.4 \mu\text{m}$.²⁰

Next, the processing of all wafers continued with the intentional Cu contamination. This step was executed by thinning the backside oxide layer down to 45 ± 10 nm in buffered HF and subsequently depositing droplets of a 15 ppb% (w/v) Cu sulfate solution on a small area ($\sim 10-11 \text{ cm}^2$) of the oxidized backside. Cu drive-in and gettering were then simultaneously performed during two different thermal

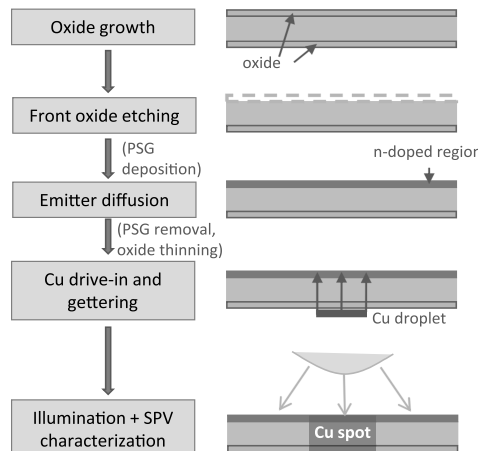


FIG. 1. Schematic representation of the experimental process flow for sample preparation and characterization.

treatments. Samples from Group A experienced an isothermal anneal at 800°C for 20 min followed by a fast air-cooling (*i.e.* direct pullout from the furnace producing a cooling rate of ~240°C/min), whereas specimens from Group B went through an additional temperature tail consisting of a cooling process from 800°C to 600°C at a controlled rate of 4°C/min before withdrawal from the furnace.

After the gettering anneals, all specimens were illuminated at room temperature (RT) under a 0.65 Suns LED lamp for up to 120h. The LID caused by the residual bulk Cu contamination was constantly monitored through the surface photovoltage (SPV) technique,²¹ which enables the time-resolved monitoring of light-induced variations of the minority carrier diffusion length caused by ungettered Cu impurities without further sample processing.

III. RESULTS

An overview of the results that will be hereinafter discussed is presented in Figure 2(a), which reports the diffusion length maps measured after 120 hours of room temperature illumination in reference specimens without phosphorus-doped layer and in the samples with n⁺-emitter that underwent the aforementioned gettering anneals. As indicated by the diffusion length map of the reference specimen, the intentionally Cu contaminated areas appear in the form of a circular low diffusion length region, which stems from stronger LID than the surrounding uncontaminated areas. The more pronounced degradation observable in the middle of the Cu-contaminated region is also an indication of higher local Cu concentrations compared to the peripheral areas.²²

In the samples from Group A, the Cu-spot remains clearly distinguishable from the neighboring uncontaminated areas. Hence, this result clearly demonstrates that, in these specimens, the gettering treatment did not result in the suppression of Cu-LID effects. In addition, the size of the Cu spot detected in these gettered samples remains comparable to the one observed in the reference samples, indicating that this gettering treatment remains ineffective towards the edge regions of the Cu-spot, where lower Cu densities are expected. Figure 2(a) also reports the SPV maps measured in the specimens from Group B. In this case, the slow cooling process experienced by such specimens appears to considerably enhance the gettering efficiency, as demonstrated by the nearly complete disappearance of Cu-LID effects after such treatment.

For the moment, we turn our attention onto the central region of each Cu spot marked by the white rectangles in Figure 2(a) and we analyze the average diffusion lengths measured within this region-of-interest before and after light soaking. As can be seen from Figure 2(b), a high initial diffusion length ($\geq 600 \mu\text{m}$) was detected before illumination in both contaminated and uncontaminated areas of all samples. After light soaking, the diffusion length in the reference sample diminished to the value of $155 \pm 15 \mu\text{m}$, whereas it resulted in the range of $220 \pm 10 \mu\text{m}$ and $380 \pm 7 \mu\text{m}$ in the specimens from Groups A and B, respectively. Outside the intentionally contaminated regions, the average diffusion length was also found to decrease from $\sim 600 \mu\text{m}$ up to $\sim 425 \mu\text{m}$, probably due to the light-activation of the so-called boron-oxygen complex.⁶

In order to quantitatively estimate the bulk Cu concentrations before and after gettering, it is possible to leverage earlier studies where the strength of the Cu-LID process (*i.e.* the lifetime/diffusion length variation before and after light soaking) has been correlated to quantitative measurements of the interstitial Cu concentrations involved in the degradation process.^{23,24} After transforming the measured diffusion lengths into the corresponding lifetimes and inserting the obtained lifetime values into the empirical formula proposed in Ref. 24, we find an average Cu concentration of $\sim 7 \times 10^{13} \text{ cm}^{-3}$ in the reference samples with no emitter, which approximately corresponds to the Cu contamination levels reported by several authors in as-cut solar-grade wafers.^{1,12,25} In Group A, the residual Cu concentration after gettering is estimated to be $\sim 3.8 \times 10^{13} \text{ cm}^{-3}$ (*i.e.* a gettering efficiency < 50%). On the other hand, the nearly complete disappearance of Cu-LID in the group B indicates residual Cu concentrations below $5 \times 10^{12} \text{ cm}^{-3}$ (gettering efficiency > 90%). Hence, the results reported in Figure 2(b) indicate that in Group A the gettering treatment led to partial removal of the bulk Cu contamination, which was however insufficient for effectively suppressing the associated Cu-LID effects.

In order to evaluate the impact of gettering on the Cu-related degradation kinetics, the decay of the diffusion length was constantly monitored during light soaking and the density of Cu-related

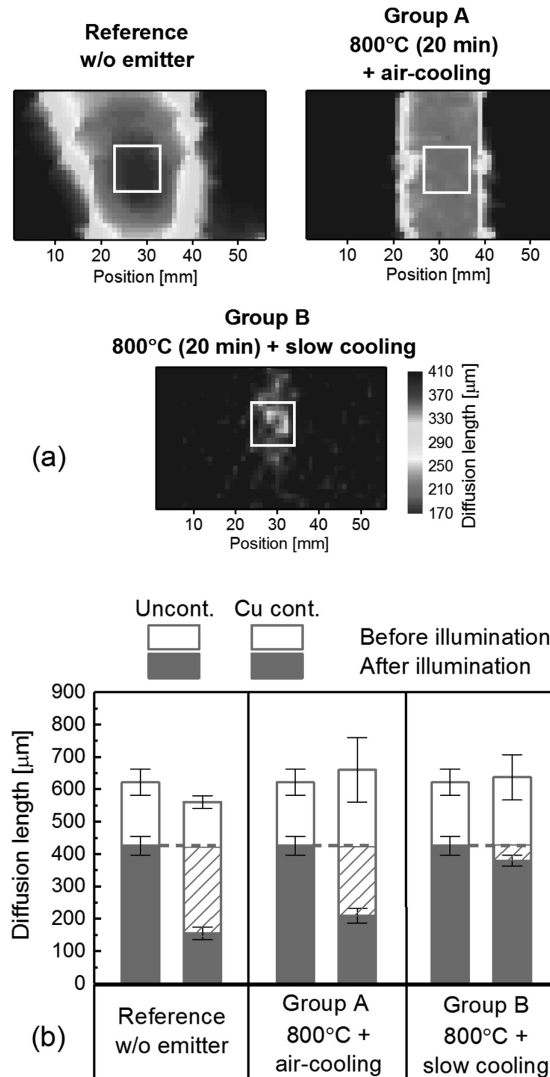


FIG. 2. (a) Diffusion length maps measured after 120 hours of RT illumination in reference specimens without phosphorus layer and in the samples from groups A and B with a POCl_3 -diffused emitter. The white rectangles mark the region-of-interest (ROI) from which the values were averaged and plotted in figures (b). Figure (b) reports the average diffusion length measured in the reference uncontaminated and within the ROIs displayed in figure (a). The shaded areas highlight the diffusion length decay caused by Cu-LID and the error bars refer to the standard deviation of the measured diffusion length within the ROI.

recombination sites was calculated as

$$N_{\text{Cu}}(t) = \frac{1}{L(t)^2} - \frac{1}{L(t=0)^2} - \frac{1}{L_{\text{ref}}(t)^2}, \quad (1)$$

where the term $L_{\text{ref}}(t)$ accounts for the aforementioned background degradation in the uncontaminated regions. Figure 3 plots the normalized value $N_{\text{Cu}}(t)/N(t \rightarrow \infty)$ as a function of illumination time.

It is possible to observe that the gettering treatment considerably slows down the Cu-related degradation, as in the specimens from Group A the saturation of the degradation kinetics is reached after several thousands of minutes, whereas in reference samples without emitter the same extent of degradation is reached within few tens of minutes. As the Cu-related degradation rate is proportional

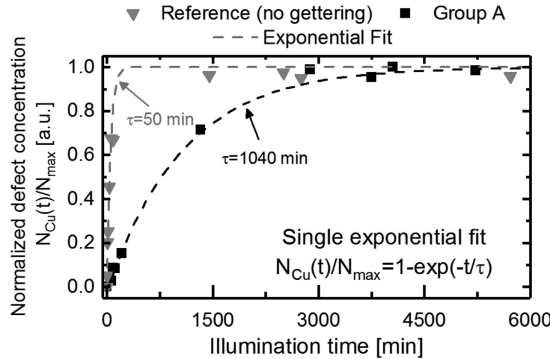


FIG. 3. Normalized Cu-related defect concentration as a function of illumination time for reference samples and gettered sample from Group A. The dashed lines represent the least-mean-square fits according to a single exponential function. The data reported in the figure have been calculated from the average diffusion length measured within the ROIs previously shown in Figure 2.

to the Cu concentration involved in the LID process.^{6,26} Figure 3 further supports the conclusion drawn from the results presented above, i.e. the gettering anneal followed by air-cooling resulted in partial, yet incomplete removal of bulk Cu impurities.

IV. DISCUSSION

On the base of the results presented above, it is possible to deduce that the cooling phases after high-temperature anneals are a critical stage for efficient Cu gettering. This is explainable with the hypothesis of impurity segregation²⁷ in the phosphorus layer driven by the enhancement of the Cu solubility gradient between the emitter and the wafer bulk during the cooling ramps. Figure 4 plots the variation of the Cu diffusivity²⁸ and the equilibrium segregation coefficient $k_{seg} = \frac{S_{em}}{S_{bulk}}$ calculated from the average Cu solubility in the bulk (S_{bulk}) and in the emitter (S_{em}) predicted by the model

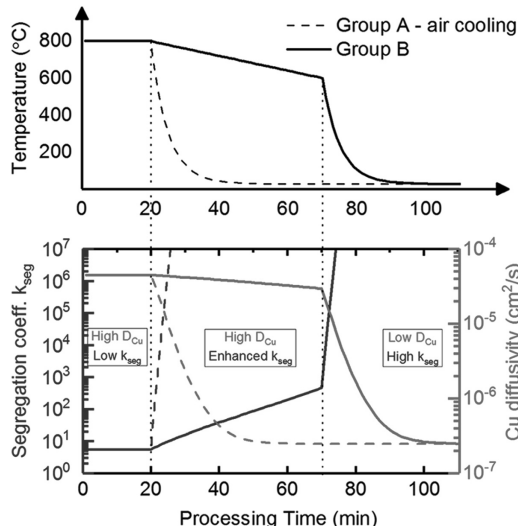


FIG. 4. Cu segregation coefficient and diffusivity during the thermal treatments for Cu drive-in and gettering calculated from the models described in Refs. 29 and 28, respectively. Temperature variation during air-cooling has been approximated through an exponential function with a time constant that reproduces the measured cooling rate (240°C/min).

proposed by Hoezl et al.²⁹ In the temperature range between 700°C and 800°C, the Cu diffusivity is maximum but $k_{seg} \approx 4$, indicating that weak impurity segregation takes place during the isothermal anneal at 800°C and the initial phase of the cooling ramp. When temperature approaches 600°C, the Cu diffusivity remains close to its maximum value, while $k_{seg} \approx 400$ due to the drastic decrease in bulk Cu solubility.

While these considerations are consistent with the experimental observations from Group B, such calculations do not fully explain the persistence of Cu impurities in Group A, which experienced the same temperature variation during the cooling phase (hence the same change in Cu solubility gradient), although on a considerably shorter timescale. Indeed, after integrating the Cu diffusivity during the different cooling transients of Groups A and B, we find that in both cases the theoretical diffusion length of Cu species exceeds the wafer thickness. Hence, the ineffectiveness of the gettering treatment in Group A does not seem to be attributable to the incomplete diffusion of Cu species during air-cooling, but presumably to other competing effects that ultimately reduce the mobility of Cu impurities. Possible competing phenomena might include impurity trapping at bulk microdefects (e.g. oxygen precipitates) or electrostatic interactions of interstitial Cu ions with the electric fields at the interface between p- and n-doped regions. In order to gain deeper insights, future work will focus on the accurate modelling of the gettering process and the in-depth analysis of the effect of precipitated oxygen on the efficiency of phosphorus gettering.

V. CONCLUSION

In this contribution, we have tested the getterability of Cu impurities in presence of a lightly doped phosphorus-emitter diffused from a POCl_3 source. The effectiveness of several gettering treatments has been evaluated in relation to their effective capability of mitigating LID effects caused by intentionally added Cu contamination. The results presented in this manuscript have shown that Cu is not necessarily a benign impurity, whose detrimental LID effects can be fully controlled by relocation to the phosphorus-doped layer. Indeed, complete mitigation of Cu-related LID effects was only achievable through the addition of a slow cooling tail after the gettering anneal, which kept the samples at intermediate temperatures (600-700°C) for several tens of minutes.

ACKNOWLEDGMENTS

The work described in this article was supported by the European Research Council under the project “SolarX” (project No. 307315). The authors acknowledge the provision of facilities and technical support by Aalto University at the Micronova Nanofabrication Centre. A.I. also acknowledges the financial support of Aalto ELEC doctoral school and Alfred Kordelin Foundation. H. S. L. acknowledges the financial support of Tiina and Antti Herlin Foundation, Finnish Cultural Foundation, and Walter Ahlström Foundation.

- ¹ A. E. Morishige, M. A. Jensen, J. Hofstetter, P. X. T. Yen, C. Wang, B. Lai, D. P. Fenning, and T. Buonassisi, *Appl. Phys. Lett.* **108**, 202104 (2016).
- ² A. A. Istratov, T. Buonassisi, R. J. McDonald, A. R. Smith, R. Schindler, J. A. Rand, J. P. Kalejs, and E. R. Weber, *J. Appl. Phys.* **94**, 6552 (2003).
- ³ M. B. Shabani, T. Yamashita, and E. Morita, *ECS Trans.* 179–193 (2008).
- ⁴ Y. Boulfrad, J. Lindroos, A. Inglese, M. Yli-Koski, and H. Savin, *Energy Procedia* **38**, 531 (2013).
- ⁵ S. Choi, B. Jang, J. Kim, H. Song, and M. Han, *Sol. Energy* **125**, 198 (2016).
- ⁶ J. Lindroos and H. Savin, *Sol. Energy Mater. Sol. Cells* **147**, 115 (2016).
- ⁷ H. Vahlman, A. Haarahiltunen, W. Kwapił, J. Schön, A. Inglese, and H. Savin, *J. Appl. Phys.* **121**, 195703 (2017).
- ⁸ H. Vahlman, A. Haarahiltunen, W. Kwapił, J. Schön, A. Inglese, and H. Savin, *J. Appl. Phys.* **121**, 195704 (2017).
- ⁹ A. Inglese, H. Vahlman, W. Kwapił, J. Schön, and H. Savin, *Phys. Status Solidi* **14**, 1700103 (2017).
- ¹⁰ Y. Boulfrad, J. Lindroos, M. Wagner, F. Wolny, M. Yli-Koski, and H. Savin, *Appl. Phys. Lett.* **105**, 182108 (2014).
- ¹¹ A. A. Istratov and E. R. Weber, *J. Electrochem. Soc.* **149**, G21 (2002).
- ¹² M. B. Shabani, T. Yamashita, and E. Morita, *Solid State Phenom.* **131–133**, 399 (2008).
- ¹³ SEMI PV Group, *International Technology Roadmap for Photovoltaic*, Seventh Edition (2016).
- ¹⁴ P. Ostoja, S. Guerri, P. Negrini, and S. Solmi, *Sol. Cells* **11**, 1 (1984).
- ¹⁵ B. Bazer-Bachi, E. Fourmond, P. Papet, L. Bouaas, O. Nichiporuk, N. Le Quang, and M. Lemiti, *Sol. Energy Mater. Sol. Cells* **105**, 137 (2012).
- ¹⁶ M. J. Kerr and A. Cuevas, *J. Appl. Phys.* **91**, 2473 (2002).
- ¹⁷ R. R. King, R. A. Sinton, and R. M. Swanson, *IEEE Trans. Electron Devices* **37**, 365 (1990).

- ¹⁸ H. Vahlman, M. Wagner, F. Wolny, A. Krause, H. Laine, A. Inglese, M. Yli-Koski, and H. Savin, Phys. Status Solidi **214** (2017).
- ¹⁹ T. Turmagambetov, S. Dubois, J. Garandet, B. Martel, N. Enjalbert, J. Veirman, and E. Pihan, Phys. Status Solidi **11**, 1697 (2014).
- ²⁰ H. S. Laine, V. Vahanissi, Z. Liu, H. Huang, E. Magana, A. E. Morishige, N. Khelifati, S. Husein, B. Lai, M. Bertoni, D. Bouhafs, T. Buonassisi, D. P. Fenning, and H. Savin, in *2016 IEEE 43rd Photovolt. Spec. Conf.* (IEEE, 2016), pp. 0678–0680.
- ²¹ D. K. Schroder, Meas. Sci. Technol. **12**, R16 (2001).
- ²² A. Inglese, J. Lindroos, and H. Savin, Appl. Phys. Lett. **107**, 52101 (2015).
- ²³ H. Väinölä, M. Yli-Koski, A. Haarahiltunen, and J. Sinkkonen, J. Electrochem. Soc. **150**, G790 (2003).
- ²⁴ H. Väinölä, E. Saarnilehto, M. Yli-Koski, A. Haarahiltunen, J. Sinkkonen, G. Berenyi, and T. Pavelka, Appl. Phys. Lett. **87**, 32109 (2005).
- ²⁵ D. Bredemeier, D. Walter, S. Herlufsen, and J. Schmidt, AIP Adv. **6**, 35119 (2016).
- ²⁶ A. Inglese, A. Focareta, F. Schindler, J. Schön, J. Lindroos, M. C. Schubert, and H. Savin, Energy Procedia **92**, 808 (2016).
- ²⁷ D. Gilles, W. Schröter, and W. Bergholz, Phys. Rev. B **41**, 5770 (1990).
- ²⁸ A. A. Istratov, C. Flink, H. Hieslmair, E. R. Weber, and T. Heiser, Phys. Rev. Lett. **81**, 1243 (1998).
- ²⁹ R. Hoelzl, K.-J. Range, and L. Fabry, Appl. Phys. A Mater. Sci. Process **75**, 525 (2002).

Publication II

A.Inglese, J.Lindroos, H.Vahlman, H.Savin. Recombination activity of light-activated copper defects in *p*-type silicon studied by injection- and temperature-dependent lifetime spectroscopy. *Journal of Applied Physics*, 107, 052101, 2016.

© 2016 American Institute of Physics Publishing LLC.
Reprinted with permission.

Recombination activity of light-activated copper defects in *p*-type silicon studied by injection- and temperature-dependent lifetime spectroscopy

Alessandro Inglesi,^{1,a)} Jeanette Lindroos,² Henri Vahlman,¹ and Hele Savin¹

¹Department of Micro- and Nanosciences, Aalto University, Tietotie 3, 02150 Espoo, Finland

²Department of Engineering and Physics, Karlstad University, Universitetsg. 2, 65188 Karlstad, Sweden

(Received 1 July 2016; accepted 7 September 2016; published online 26 September 2016)

The presence of copper contamination is known to cause strong light-induced degradation (Cu-LID) in silicon. In this paper, we parametrize the recombination activity of light-activated copper defects in terms of Shockley—Read—Hall recombination statistics through injection- and temperature-dependent lifetime spectroscopy (TDLS) performed on deliberately contaminated float zone silicon wafers. We obtain an accurate fit of the experimental data via two non-interacting energy levels, i.e., a deep recombination center featuring an energy level at $E_c - E_t = 0.48 - 0.62$ eV with a moderate donor-like capture asymmetry ($k = 1.7 - 2.6$) and an additional shallow energy state located at $E_c - E_t = 0.1 - 0.2$ eV, which mostly affects the carrier lifetime only at high-injection conditions. Besides confirming these defect parameters, TDLS measurements also indicate a power-law temperature dependence of the capture cross sections associated with the deep energy state. Eventually, we compare these results with the available literature data, and we find that the formation of copper precipitates is the probable root cause behind Cu-LID. *Published by AIP Publishing.*

[<http://dx.doi.org/10.1063/1.4963121>]

I. INTRODUCTION

Light-induced degradation (LID) is a current topic in silicon photovoltaics research due to its deleterious impact on solar cell efficiency upon exposure to illumination. This phenomenon has been traditionally ascribed to the formation of metastable boron-oxygen (B-O) complexes, whose composition has been intensively debated in the literature.^{1,2} However, recent results that showed severe LID in solar cells fabricated from multicrystalline silicon substrates^{3,4} with low bulk oxygen content have raised numerous discussions on alternative defect reactions, which might explain the observed degradation process. Low levels of copper contamination have been recently shown to cause a similar LID effect in both mono-⁵ and multi-crystalline silicon.^{6,7} This phenomenon is referred to as copper-related light-induced degradation (Cu-LID), and it has been suggested to arise from increased bulk recombination^{8–10} caused by copper precipitation^{11,12} or substitutional copper complexes.^{13–15} Nevertheless, the recombination mechanisms at Cu-LID defects still remain unclear, and the current literature information is lacking in an accurate parametrization of the recombination activity of such defects. Therefore, it is important to determine the recombination parameters of Cu-LID defects in order to quantify their effect on minority carrier lifetime and predict their impact on the overall solar-cell performance.

Lifetime spectroscopy (LS) has been proposed in the literature as an effective approach to characterize electrically active defects through standard minority carrier lifetime measurements.^{16,17} LS techniques are based on the analysis of the injection- and temperature dependence of the minority carrier lifetime in terms of Shockley—Read—Hall

(SRH) recombination statistics,^{18,19} such that the recombination parameters of the lifetime-limiting defect can be directly determined from least-squares fits to the experimental data. Since carrier lifetime is one of the most sensitive parameters to the presence of electrically active defects, LS methods enable the characterization of recombination active defects with concentrations well below the detection limit of other well-established characterization techniques, e.g., deep level transient spectroscopy (DLTS).

This paper aims at gaining a deeper insight into the recombination activity of the defect behind Cu-LID and the associated recombination phenomena. In this contribution, we apply LS methods to determine the SRH recombination parameters of light-activated Cu defects in deliberately contaminated float zone silicon (FZ-Si) wafers, which are free of B-O recombination due to the low bulk oxygen concentration. Since SRH parameters represent a typical fingerprint of the underlying recombination active defect, the extracted defect parameters have been compared with literature data, in order to correlate the LS results with the existing information on electrically active copper complexes.

II. EXPERIMENTAL

A. Sample preparation

The experiments were conducted on B-doped, 4-in., [100]-oriented FZ-Si wafers with the thickness of 280 μm and resistivity of 0.9, 3.4, and 18.4 $\Omega\cdot\text{cm}$. After standard RCA-1 and RCA-2 cleanings, the wafer surfaces were passivated by growing a 15 nm thick thermal oxide layer, which was formed during 40 min of dry oxidation at 900 °C followed by annealing in nitrogen ambient at the same temperature for 20 min. Some wafers were then kept as reference samples, while the rest of the batch was subjected to intentional copper

^{a)}E-mail: alessandro.inglese@aalto.fi

contamination, performed by spinning a 1 ppm copper sulfate solution and subsequently annealing the samples in a nitrogen atmosphere at 800 °C for 20 min. This procedure resulted in bulk interstitial copper contamination, whose concentration is estimated to be in the range of 10^{14} cm^{-3} . Next, an external corona charge was deposited on both wafer sides (+0.3 $\mu\text{C}/\text{cm}^2$) to prevent Cu out-diffusion and decrease the surface minority carrier recombination through the formation of an inversion layer near the surface. The samples were then exposed to room temperature illumination under a 0.5 Sun LED lamp for up to 130 h in order to induce LID until the achievement of complete lifetime saturation. During light soaking, the lifetime decay caused by Cu-LID was constantly recorded as a function of illumination time through automated quasi-steady state photoconductance decay (QSSPC) measurements.

B. Injection and temperature-dependent lifetime measurements

Minority carrier lifetime measurements were performed by means of a Sinton WCT 120-TS tester, which allows injection-dependent QSSPC lifetime measurements at temperatures between 20 °C and 200 °C. The measurement setup consists of an inductive RF coil incorporated within a thermocouple-controlled measurement stage. Temperature-dependent measurements were performed by initially heating the measurement stage up to the maximum temperature and subsequently measuring the lifetime after predefined temperature steps of the cooling transient. Since carrier mobility strongly depends on the temperature, a correction based on Dorkel-Leturcq's mobility model²⁰ was applied to ensure the optimal calibration of the instrument over the whole temperature range. Furthermore, as the QSSPC technique is prone to trapping artifacts at low injection conditions,²² measurement points featuring abnormal lifetime increase at excess carrier concentrations below 10^{14} cm^{-3} were excluded from the analysis of the experimental data.

III. MODELING OF THE EXPERIMENTAL DATA

The SRH theory provides a well-established statistical model for describing charge carrier recombination at single energy levels within the bandgap, and it constitutes the conceptual framework behind lifetime spectroscopy methods. The determination of defect parameters through lifetime spectroscopy is thus performed under the assumption that the unknown recombination active defect introduces discrete energy levels. Supposing negligible trapping and, hence, equal excess electron and hole concentration ($\Delta n = \Delta p$), the SRH lifetime τ_{SRH} associated with a single-level defect is given by the following well-known equation:²¹

$$\tau_{SRH}(\Delta n, T) = \frac{\tau_{n0}(p_0 + p_1 + \Delta n) + \tau_{p0}(n_0 + n_1 + \Delta n)}{p_0 + n_0 + \Delta n}, \quad (1)$$

where n_0 and p_0 , respectively, represent the equilibrium electron and hole concentrations and the capture time constants τ_{n0} and τ_{p0} are related to the defect density N_t , the thermal

velocity v_{th} , and the electron and hole capture cross sections σ_n and σ_p via $\tau_{n0} = (N_t v_{th} \sigma_n)^{-1}$ and $\tau_{p0} = (N_t v_{th} \sigma_p)^{-1}$. The quantities n_1 and p_1 are often referred to as SRH densities and represent the electron and hole concentrations when the defect energy level E_t coincides with the Fermi level, i.e.,

$$n_1(E_t, T) = N_c \exp\left(-\frac{E_c - E_t}{kT}\right) \quad \text{and} \\ p_1(E_t, T) = N_v \exp\left(-\frac{E_v - E_t}{kT}\right), \quad (2)$$

where E_c and E_v are the energetic positions of the conduction and valence bands and N_c and N_v are the effective densities of states in the conduction and valence bands, respectively. The recombination center is, thus, defined via three fundamental parameters, i.e., τ_{n0} , τ_{p0} , and E_t , which must be simultaneously fitted from the injection and temperature-dependent experimental data. When the effect of two or more energy levels is taken into account, the total SRH lifetime is calculated as a reciprocal sum of the inverse lifetimes given by each recombination center.

The injection-dependent lifetime spectroscopy (IDLS) consists of the determination of the defect parameters by fitting Eq. (1) to the injection-dependent lifetime curves. Since the IDLS alone often yields ambiguous results, the analysis must be complemented with the temperature-dependent lifetime spectroscopy (TDLS). In this case, Eq. (1) is fitted to the temperature-dependent lifetime data measured at fixed injection level. The major contribution to the overall temperature dependence arises from the exponential dependence of n_1 and p_1 . However, since Eq. (2) includes the state density N_c and N_v , the variation of these two parameters as a function of temperature must also be taken into account, i.e.,

$$N_C(T) = N_C^{300K} \left(\frac{T}{300K}\right)^{1.5} \quad \text{and} \\ N_V(T) = N_V^{300K} \left(\frac{T}{300K}\right)^{1.5}, \quad (3)$$

where the effective densities of states are taken as $N_c^{300K} = 2.86 \times 10^{19} \text{ cm}^{-3}$ and $N_v^{300K} = 3.1 \times 10^{19} \text{ cm}^{-3}$.²³ Additional temperature-dependence is imposed by the capture time constants τ_{n0} and τ_{p0} via the capture cross sections σ_n and σ_p , whose variation mainly depends on the recombination mechanisms at the defect, and the carrier thermal velocity v_{th} , which has been parametrized as follows:

$$v_{th}(T) = v_{th}^{300K} \left(\frac{T}{300K}\right)^{0.5} \quad (4)$$

with $v_{th}^{300K} = 1.1 \times 10^7 \text{ cm/s}$ being the thermal velocity of carriers at 300 K. As a first approximation, σ_n and σ_p are assumed to be temperature independent. Since a single set of defect parameters must provide an optimum fit to all the temperature- and injection-dependent lifetime curves, the temperature-dependence of σ_n and σ_p has been subsequently introduced in order to resolve possible inconsistencies between the fit results obtained from IDLS and TDLS analyses.

IV. RESULTS

A. Degradation process and determination of Cu-related lifetime

Figure 1 presents the effective lifetime measured during room-temperature illumination in an intentionally Cu-contaminated $3.4 \Omega\text{-cm}$ FZ sample. The absence of LID in the reference sample indicates that the lifetime decay observed with intentionally contaminated specimens is solely caused by copper impurities. The Cu-related degradation process in FZ-Si occurs via a single asymptotical degradation process, which leads to complete lifetime saturation after at least 50 h of uninterrupted illumination. In this work, defect characterization has been carried out after complete lifetime saturation, such that the characterization of the defect is performed during its most harmful and recombination active state.

In order to obtain reliable spectroscopic results, the bulk lifetime limited by recombination at copper defects must always be separated from the effect of other recombination mechanisms, e.g., Auger, radiative, and surface recombination. Since no LID is observed in the reference sample, it can be reasonably assumed that light soaking solely activates Cu-LID defects while leaving the other recombination mechanisms unchanged. Therefore, the effective Cu-related lifetime ($\tau_{Cu\text{-eff}}$) can be calculated as follows:

$$\tau_{Cu\text{-eff}} = \left(\frac{1}{\tau_{Cu\text{-deg}}} - \frac{1}{\tau_{ref}} \right)^{-1}, \quad (5)$$

where $\tau_{Cu\text{-deg}}$ and τ_{ref} are the minority carrier lifetimes measured after light soaking in the intentionally Cu-contaminated and the clean reference sample, respectively.

Figure 2 shows the lifetime values of $\tau_{Cu\text{-deg}}$, τ_{ref} , and $\tau_{Cu\text{-eff}}$ plotted against the excess carrier densities. The superposition of the curves representing $\tau_{Cu\text{-deg}}$ and $\tau_{Cu\text{-eff}}$ over a broad injection range proves that the measured lifetime is largely dominated by carrier recombination through light-activated copper defects. Note that, in Eq. (5), the lifetime measured before illumination τ_{init} can, in principle, be used

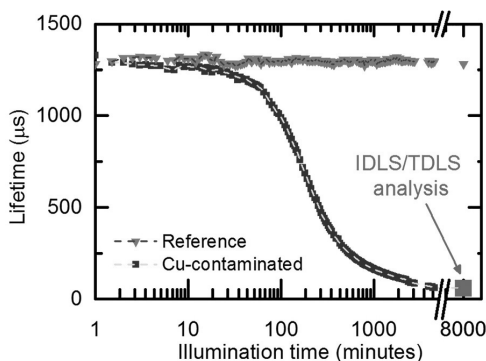


FIG. 1. Minority carrier lifetime measured at a fixed injection level ($\Delta n = 1 \times 10^{14} \text{ cm}^{-3}$) as a function of the illumination time measured in a clean reference (magenta) and 1 ppm Cu-contaminated (blue) FZ-Si sample with the resistivity of $3.4 \Omega\text{-cm}$.

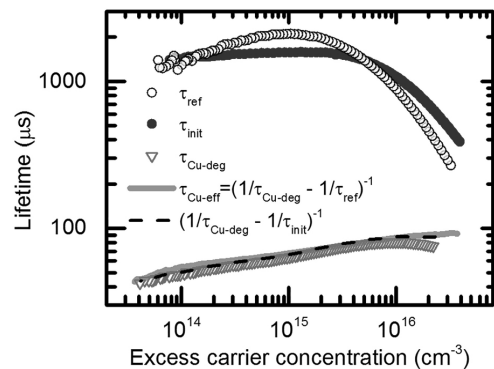


FIG. 2. Minority carrier lifetime measured after degradation ($\tau_{Cu\text{-deg}}$ —open red triangles) with an intentionally Cu-contaminated $3.4 \Omega\text{-cm}$ FZ wafer and in an analogous clean reference specimen (τ_{ref} —open white circles). The image also reports the lifetime curve measured in the contaminated specimen before light soaking (τ_{init} —filled blue circles) and the effective copper-related SRH lifetime calculated by compensating $\tau_{Cu\text{-deg}}$ with τ_{ref} (solid pink line) and τ_{init} (dashed black line). The slight shift between τ_{init} and τ_{ref} does not significantly affect the calculation of the effective Cu-related lifetime, as indicated by the superposition of the dashed black curve with the effective lifetime values calculated with (5).

in lieu of τ_{ref} for the determination of the effective Cu-related lifetime. The figure also displays the Cu-related lifetime calculated by means of τ_{init} and τ_{ref} . Despite the slight shift between τ_{init} and τ_{ref} , which is probably caused by the effect of the contamination procedure on surface and Auger recombination, the superposition of the lifetime curves obtained from these two methods indicates that both of them can be used to determine the actual Cu-related lifetime. Since the latter approach would require the accurate measurement of τ_{init} at varying temperatures, which may turn interstitial copper into a recombination active state before light soaking,^{9,13,24} in this work, τ_{Cu} has been calculated by compensating the lifetime measured after degradation with temperature-dependent lifetime data obtained from a separate non-contaminated reference specimen.

B. Parametrization of the Cu-related lifetime in terms of SRH statistics

Figure 3 shows the injection-dependent lifetime curves in the temperature range from 25 to 195°C and the corresponding SRH fit to the measured lifetime data. The SRH fit of the entire set of injection- and temperature dependent lifetime curves requires the assumption of two non-interacting energy states, i.e., a deep recombination center, which mostly dominates the lifetime curve at a low injection level, and an additional shallow energy level affecting the carrier lifetime only at high injection conditions.

Since the coexistence of two defect centers unavoidably increases the number of parameters that must be simultaneously determined from each fit, the fit procedure was divided into several steps. As it will be discussed below in Fig. 4, the optimum fit of the low-injection part of each lifetime curve is achieved through a wide range of the defect parameters associated with the deep recombination center. Therefore, in an initial step, the defect parameters of the

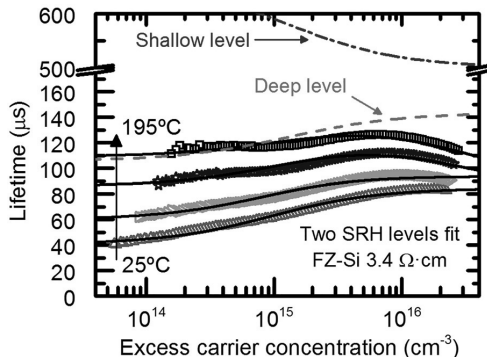


FIG. 3. SRH fit (solid lines) of the injection-dependent lifetime data (symbols) measured at varying temperatures with an intentionally Cu-contaminated p-type FZ-wafer. The lifetime data have been modeled assuming a deep (dashed red line) recombination center with the defect parameters determined in Figure 5 and a shallow (dashed-dotted blue line) recombination center located at $E_c - E_t = 0.15 \text{ eV}$ with $k = 0.1$.

shallow recombination center were initially optimized to fit the high injection part of the whole set of lifetime curves and the parameters associated with the deep level were arbitrarily chosen from the ranges that guarantee the optimum fit to the experimental data. Subsequently, the parameters of the shallow energy level were kept on fixed values ($E_c - E_t = 0.15 \text{ eV}$ with $k = 0.1$) and the true parameters associated with the deep recombination center were determined through the defect parameter solution surface (DPSS) method proposed by Rein *et al.*^{25,26} This approach consists of a fit routine which calculates the optimal fit values of the symmetry factor $k = \frac{\tau_{p0}}{\tau_{n0}} = \frac{\sigma_n}{\sigma_p}$ and τ_{n0} associated with the deep recombination center, while varying the values of the defect energy level E_t across the whole bandgap. Figure 4 shows an example of DPSS analysis applied to a single IDLS curve measured at room temperature, where the fitted k -factors are plotted together with the

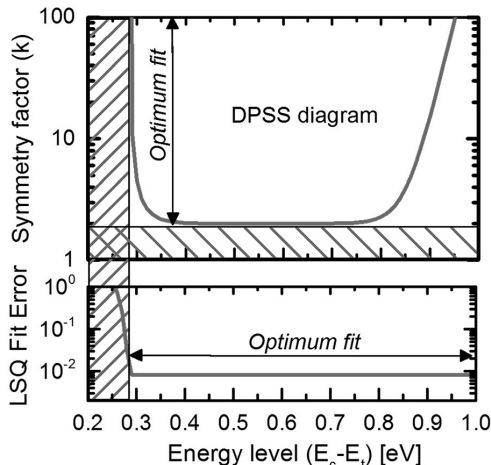


FIG. 4. DPSS diagram of a single IDLS curve measured at room temperature. The fit error is assessed by calculating the optimal fit parameters for each energy level. The fit result shown in the diagram sets a lower bound for the energy level ($E_c - E_t > 0.28 \text{ eV}$) and the symmetry factor ($k > 2$).

least-squares fit error for each energy level E_t . It results clear that the analysis of a single injection-dependent lifetime curve leads to rather ambiguous fit results, as the least squares fit error is minimized by a broad range of different defect parameters. Such ambiguity can be overcome by extending the DPSS to the whole set of temperature-dependent lifetime curves and superposing the corresponding DPSS curves in the same graph, as shown in Figure 5(a). In this case, the optimal values of the defect parameters are identified by the convergence of all DPSS curves into a common intersection point. The displacement between the DPSS curves has been quantified in terms of relative standard deviation of the DPSS- k values at each energy level E_t , which is plotted in Figure 5(b). The relative standard deviation presents two distinct minima located at $E_c - E_t = 0.48 \pm 0.01 \text{ eV}$ and $E_c - E_t = 0.62 \pm 0.02 \text{ eV}$. Hence, the large ambiguity arising from the SRH fit of a single IDLS curve results to be confined to a relatively narrow energy range located across the mid-bandgap, whose boundaries represent the optimal fit parameters. The minima of the calculated relative standard deviation also allow us to estimate the value of the symmetry factor, which results to be unambiguously determined as $k = 1.7 \pm 0.4$.

As discussed in Ref. 25, the superposition of all the temperature-dependent DPSS curves significantly reduces the ambiguity of the fit result obtained from a single IDLS curve. However, this method does not allow us to determine which of the two intersection points correspond to the exact defect parameters due to the reduced sharpness of the intersection

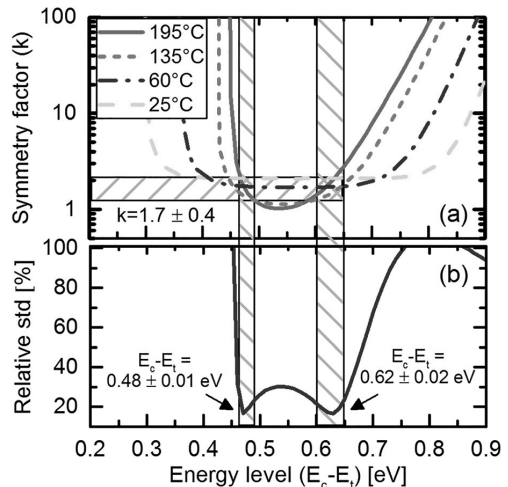


FIG. 5. DPSS analysis of the injection-dependent lifetime curves measured at varying temperatures. (a) Superposition of all DPSS- k curves in the same plot area. (b) Relative standard deviation (purple solid line) of the DPSS- k curves as a function of the energy level. The convergence of the curves to the common intersection points has been assessed in terms of relative standard deviation, whose minima define the optimal values of the energy level ($E_c - E_t = 0.48 \pm 0.01 \text{ eV}$ and $E_c - E_t = 0.62 \pm 0.02 \text{ eV}$) and symmetry factor $k = 1.7 \pm 0.4$. The error margins have been estimated from the width of the minima of the curve representing relative standard deviation, i.e., a 10% tolerance range has been defined for each plateau and the uncertainty ranges for k and the energy level have been accordingly determined.

points. This is probably a consequence of the fit errors, the moderate capture asymmetry of the defect which confines the possible solutions to a narrow range of values and the slight variation of k across the temperature range imposed by the temperature-dependence of capture cross sections.

C. Temperature dependence of $\sigma_{n,p}$ and verification of LS results

In order to analyze the temperature dependence of capture cross sections and ascertain the validity of the previous spectroscopic results, the SRH model has been applied to the TDLS lifetime data. Figure 6(a) displays the temperature-dependent lifetime measured at the excess carrier density $\Delta n = 2 \times 10^{14} \text{ cm}^{-3}$, which corresponds to the lowest injection level at which the lifetime was reliably measured by the instrument across the temperature range. Since the shallow energy level has a negligible effect on the low-injection lifetime, the TDLS curve is fully described by a single SRH energy level. If capture cross sections are assumed to be temperature-independent, the best fit is achieved with a defect located in the upper half of the bandgap with an energy level of $E_c - E_t = 0.13 \text{ eV}$ (Figure 6(b)).

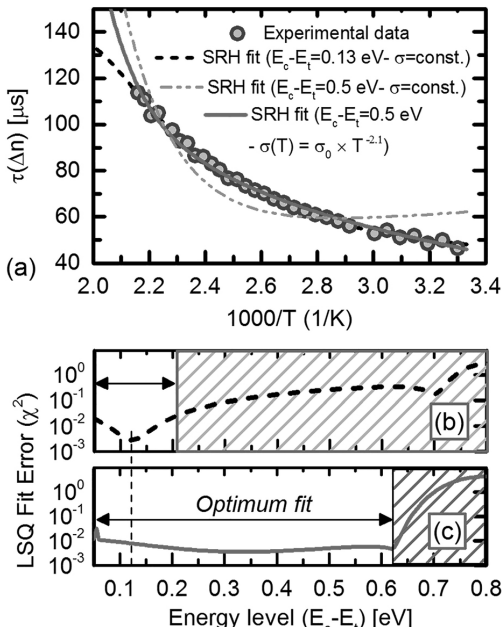


FIG. 6. Lifetime temperature dependence measured at a fixed injection level ($\Delta n = 2 \times 10^{14} \text{ cm}^{-3}$) in an intentionally Cu-contaminated p-type $3.4 \Omega \cdot \text{cm}$ FZ sample. (a) The experimental data (circles) are fitted to the SRH model assuming (i) a defect energy level $E_c - E_t = 0.13 \text{ eV}$ with temperature independent capture cross sections (black dashed line), (ii) a deep recombination center at $E_c - E_t = 0.5 \text{ eV}$ with temperature independent capture cross sections (orange dashed-dotted line), and (iii) energy level at $E_c - E_t = 0.5 \text{ eV}$ with a power law temperature dependence $\sigma(T) = \sigma_0 \times T^{-2.1}$ (red solid line). ((b) and (c)) DPSS diagrams of the least squares fit error obtained with (solid red line) and without (dashed black line) the assumption of temperature-dependent capture cross sections. In the case of temperature-dependent capture cross sections, the optimum fit to the experimental data is obtained when the energy level $E_c - E_t < 0.61 \text{ eV}$.

However, the IDLS result in Figure 4 indicates that the energy level must lie deeper in the band gap to allow a simultaneous fit to the injection- and temperature-dependent lifetime data, such that the spectroscopic information gained under the assumption of temperature-independent capture cross sections has to be rejected for reasons of inconsistency. As can be seen from Figure 6(a), if the defect energy level is assumed to be located near the mid-bandgap, the supposition of temperature independent capture cross sections leads to the overestimation of the LLI lifetime at room temperature. This suggests that the SRH model must be complemented with an appropriate parametrization that accounts for the enlargement of $\sigma_{n,p}$ at decreasing temperatures.²⁵ The optimum fit to the experimental data is obtained under the assumption of a power-law temperature dependence of the capture cross sections,²⁵ i.e., $\sigma(T) = \sigma_0 \times T^{-\alpha}$ with $\alpha = 2.1$. The identified $\sigma(T)$ -dependence will be further discussed in Sec. V.

Concerning the defect energy levels, the DPSS diagram in Figure 6(c) shows that the fitting error is minimized within the energy range between the conduction band edge and $E_c - 0.61 \text{ eV}$, thus excluding most of the lower half of the bandgap from the possible energy levels associated with the deep recombination center. The domain of possible defect parameters that provide a consistent fit to both injection- and temperature-dependent curves is further restricted if the spectroscopic result from the IDLS curve in Figure 4 and the result of the TDLS analysis (Figure 6(c)) are superposed in the same graph, as indicated in Figure 7. The DPSS- k diagrams in Figure 7(a) show two specific intersection points located at $E_c - 0.49 \text{ eV}$ and $E_c - 0.61 \text{ eV}$ with a common symmetry factor $k=2$, resulting in good agreement with the spectroscopic result that was previously discussed in Sec. IV B.

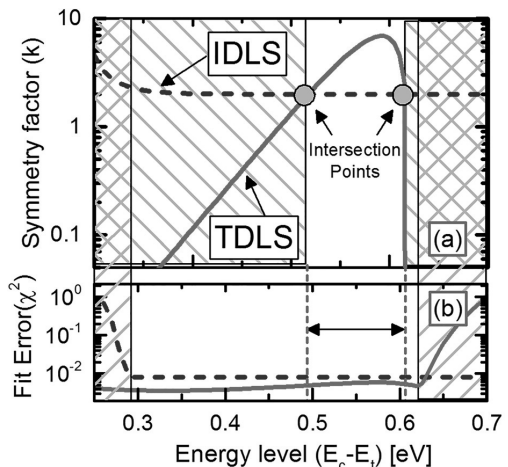


FIG. 7. Superposition of the DPSS diagrams extracted from the TDLS (solid red lines) and IDLS (dashed blue lines) lifetime data shown in Figures 4 and 6(c). (a) The intersection points of the DPSS- k curves (grey circles) indicate the defect parameters that provide an optimum fit to both IDLS and TDLS curves. (b) The fit error of both IDLS and TDLS is minimized within the energy range between $E_c - 0.28 \text{ eV}$ and $E_c - 0.63 \text{ eV}$, thus confining the defect energy level within this energy interval.

D. LS results obtained with different specimens

In order to cross-check the spectroscopic results obtained thus far, LS analyses have been applied to a set of FZ wafers with varying doping concentrations. For all samples, the SRH fit required the assumption of two independent recombination centers, one of them being a shallow energy state located between $E_c - 0.1$ eV and $E_c - 0.2$ eV with $k = 0.1$.

Concerning the deep recombination center, Table I summarizes the SRH parameters fitted from the lifetime data of all samples, and the SRH fit of the lifetime data obtained at room temperature is shown in Fig. 8. It is possible to notice that the spectroscopic analysis led to the identification of similar values for both k and $E_c - E_t$, thus confirming the existence of energy states near the mid-bandgap with a moderate capture asymmetry. Furthermore, the SRH fit of all TDLS curves confirms the aforementioned $\sigma(T)$ -dependence, which was modeled in terms of $\sigma(T) = \sigma_0 \times T^{-\alpha}$ with the exponent α varying between 1.2 and 2.1.

V. COMPARISON WITH LITERATURE DATA AND DISCUSSION

The spectroscopic analysis of the injection- and temperature-dependent lifetime data indicated the coexistence of at least two energy levels, i.e., a deep energy state located near the mid-bandgap and a shallow level in the upper bandgap half. Copper is known to give rise to a variety of complexes in silicon, some of which have been correlated with previously reported DLTS spectra. Interstitial copper (Cu_i^+) atoms and copper-boron (CuB) pairs are unlikely to affect the minority carrier lifetime, as no recombination activity has been related to such complexes.^{27,28} Moreover, the concentration of Cu_i^+ has been observed to decrease during illumination,²⁹ thus indicating the transformation of Cu_i^+ into a different recombination-active defect. The formation of substitutional copper defects (Cu_s) during light soaking has been intensively discussed in the literature. Early contributions attributed Cu-LID to the dissociation of a recombination inactive pure copper complex, which was long presumed to be Cu_sCu_i pair, and the subsequent formation of highly recombination active Cu_s complexes.^{14,30} However, this reaction does not explain the aforementioned decrease of Cu_i^+ concentration during light-soaking. Moreover, DLTS studies on intentionally Cu contaminated material revealed the existence of two acceptor energy states located at $E_v + 0.41\ldots0.45$ eV³¹⁻³⁴ and $E_c - 0.16$ eV²⁴ and a donor energy level at $E_v + 0.22$ eV,^{24,35} which were later associated with the substitutional copper defect.³⁵ While the energy state at $E_c - 0.16$ eV seems to be in good agreement with LS results reported in this study,

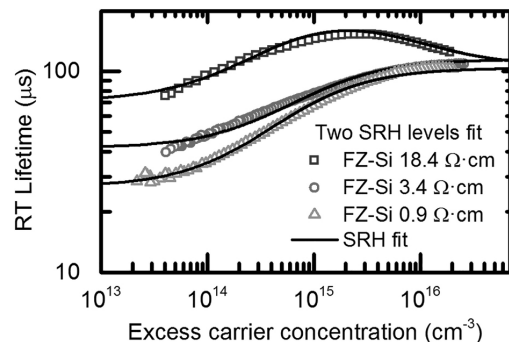


FIG. 8. Injection dependent lifetime curves measured at room temperature in Cu-contaminated samples featuring different doping concentrations. The solid line represents the fit obtained with two non-interacting SRH levels (deep and shallow).

no strong evidence of the other energy states can be found. The acceptor-like behavior of the deep energy state at $E_v + 0.41\ldots0.45$ eV would impose a large capture cross section for majority carriers, and hence $k \ll 1$, which is in disagreement with the spectroscopic result that was shown in Sections IV B and IV C. Furthermore, the energy level of this recombination center seems not to match the result of the TDLS fit and the temperature-dependent DPSS analysis (Figures 5 and 6(c)), which set the energy level at least 100 meV deeper into the bandgap.

Copper is also known to form electrically active copper silicides ($\eta'' - Cu_3Si$)³⁶ stemming from the precipitation of Cu_i^+ atoms. Such extended defects introduce a continuous band of energy states in the upper half of the bandgap, from $E_c - 0.15$ eV to $E_c - (0.4\ldots0.5)$ eV^{37,38} with an estimated electron capture cross-section $\sigma_n = 3 \times 10^{-16} \text{ cm}^2$.³⁹ Macdonald *et al.* showed through LS methods that the impact of this distributed energy band can be approximated via two non-interacting SRH defects with energy levels located at $E_c - 0.15$ eV and $E_c - 0.58$ eV, which approximately correspond to the extremes of the aforementioned energy band.^{40,41} Though some uncertainty on the actual energy levels exists, the spectroscopic result obtained in this work appears to be in good agreement with the IDLS and TDLS analysis presented by Macdonald *et al.* for thermally induced Cu precipitates. Considering that Cu precipitates introduce a continuous band of energy states rather than individual states due to their extended nature, it must be pointed out that a rigorous study of carrier recombination through distributed energy states would require more complex recombination models. This may explain the slight displacement

TABLE I. Overview of the defect parameters associated with the deep recombination center in Cu-contaminated FZ-Si samples with varying resistivity. The optimal defect parameters have been obtained by superposing the DPSS diagrams associated with all the temperature-dependent lifetime curves, as illustrated in Figure 5. The $\sigma(T)$ -dependence was determined by fitting the SRH model to the TDLS lifetime data, as described in Sec. IV C.

Resistivity [$\Omega\cdot\text{cm}$]	p_0 [cm^{-3}]	DPSS solution 1 $E_c - E_t$ [eV]	DPSS solution 2 $E_c - E_t$ [eV]	$k^{DPSS-1,2}$	$\sigma(T)$
0.9	1.65×10^{16}	0.51 ± 0.02	0.61 ± 0.02	2.6 ± 0.4	$\propto T^{-1.2}$
3.4	4×10^{15}	0.48 ± 0.01	0.62 ± 0.02	1.7 ± 0.4	$\propto T^{-2.1}$
18.4	7.13×10^{14}	0.51 ± 0.03	0.59 ± 0.03	1.9 ± 0.3	$\propto T^{-1.9}$

between the experimental data and the fitted SRH lifetime, which is visible in Figures 3 and 8. Nevertheless, the results shown in this contribution indicate that the description of the lifetime data via the assumption of single point-like SRH energy states still provides a satisfactory approximation of the underlying recombination activity over the measurable injection range.

Based on the above defect identification, it is possible to relate the recombination mechanisms at metal precipitates to the aforementioned $\sigma(T)$ -dependence and speculate on the effect of the degradation conditions (e.g., light intensity or temperature during LID) on the recombination activity of such defects. The $\sigma(T)$ -dependence described in Sec. IV C is likely to arise from the temperature dependence of the thermionic recombination currents at the Schottky junction formed near the precipitate-semiconductor interface.⁴² The aforementioned $\sigma(T)$ -dependence has also been associated with the excitonic Auger capture process, which has been reported for defects introducing deep energy states.⁴³

In addition to the doping concentration, the degradation kinetics of Cu-LID have been found to significantly dependent on other parameters, such as illumination intensity, temperature, and the presence of bulk defects (e.g., vacancies or dislocations).^{7,15} All these parameters are likely to affect the precipitate size distribution and, therefore, result in a different recombination activity of such defects. In addition to providing further evidence of the existence of such precipitates, advanced recombination models that correlate the injection-dependent lifetime with the precipitate radius⁴⁴ may also provide additional information on the formation mechanisms.

VI. CONCLUSION

In this work, injection- and temperature-dependent lifetime spectroscopy analysis has been applied to intentionally Cu-contaminated *p*-type FZ silicon for characterizing the recombination activity of the defects activated under room-temperature illumination. In order to verify the accuracy and repeatability of the spectroscopic result, the analysis has been applied to a set of similarly processed wafers of different resistivities. For all samples, IDLS and TDLS methods revealed that the recombination activity of light-activated copper defects is well described by two non-interacting energy levels, i.e., a shallow energy level at $E_c - E_t = 0.1 - 0.2 \text{ eV}$ and a deep recombination center at $E_c - E_t = 0.48 - 0.51 \text{ eV}$ or $E_c - E_t = 0.59 - 0.62 \text{ eV}$ with k varying between 1.7 and 2.6 and a strong power-law temperature dependence of the capture cross sections. The defect energy levels coincide with the edges of the energy band associated with Cu-precipitates, thus indicating this defect as the possible culprit behind the observed LID process. Since lifetime spectroscopy methods are mostly sensitive to the defects that impact the recombination lifetime to a greater extent, the result shown in this work does not rule out the coexistence of other less-recombination active defects, which might be pinpointed by DLTS measurements.

ACKNOWLEDGMENTS

This research was performed at the Micronova Nanofabrication Centre of Aalto University. The authors

acknowledge the support from the European Research Council under the European Union's FP7 Programme ERC Grant Agreement No. 307315. A.I. acknowledges the support of the Aalto ELEC doctoral school. J.L. acknowledges the Characterization and Modeling of Materials (CMM) Group at Karlstad University and Walter Ahlström Foundation.

- ¹J. Schmidt and K. Bothe, "Structure and transformation of the metastable boron- and oxygen-related defect center in crystalline silicon," *Phys. Rev. B* **69**(2), 024107 (2004).
- ²V. V. Voronkov and R. Falster, "Light-induced boron-oxygen recombination centres in silicon: Understanding their formation and elimination," *Solid State Phenom.* **205–206**, 3–14 (2013).
- ³F. Fertig, K. Krauß, and S. Rein, "Light-induced degradation of PECVD aluminium oxide passivated silicon solar cells," *Phys. Status Solidi -Rapid Res. Lett.* **9**(1), 41–46 (2015).
- ⁴K. Ramspeck, S. Zimmermann, H. Nagel, A. Metz, Y. Gassenbauer, B. Brikmann, and A. Seidl, "Light induced degradation of rear passivated mc-Si solar cells," in *Proceedings of the 27th EUPVSEC*, 2012, pp. 861–865.
- ⁵H. Savin, M. Yli-Koski, and A. Haarahlitunen, "Role of copper in light induced minority-carrier lifetime degradation of silicon," *Appl. Phys. Lett.* **95**(15), 152111 (2009).
- ⁶J. Lindroos, Y. Boulfad, M. Yli-Koski, and H. Savin, "Preventing light-induced degradation in multicrystalline silicon," *J. Appl. Phys.* **115**(15), 154902 (2014).
- ⁷A. Ingelse, A. Focareta, F. Schindler, J. Schön, J. Lindroos, M. C. Schubert, and H. Savin, "Light-induced degradation in multicrystalline silicon: The role of copper," *Energy Proc.* **92C**, 808–814 (2016).
- ⁸J. Lindroos and H. Savin, "Formation kinetics of copper-related light-induced degradation in crystalline silicon," *J. Appl. Phys.* **116**(23), 234901 (2014).
- ⁹Y. Boulfad, J. Lindroos, M. Wagner, F. Wolny, M. Yli-Koski, and H. Savin, "Experimental evidence on removing copper and light-induced degradation from silicon by negative charge," *Appl. Phys. Lett.* **105**(18), 182108 (2014).
- ¹⁰Y. Boulfad, J. Lindroos, A. Ingelse, M. Yli-Koski, and H. Savin, "Reduction of light-induced degradation of boron-doped solar-grade Czochralski silicon by Corona charging," *Energy Proc.* **38**, 531–535 (2013).
- ¹¹H. Väinölä, M. Yli-Koski, A. Haarahlitunen, and J. Sinkkonen, "Sensitive copper detection in P-type CZ silicon using μ PCD," *J. Electrochem. Soc.* **150**(12), G790 (2003).
- ¹²M. Yli-Koski, H. Väinölä, A. Haarahlitunen, J. Storgårds, E. Saarnilehto, and J. Sinkkonen, "Light activated copper defects in P-type silicon studied by PCD," *Phys. Scr.* **114**, 69–72 (2004).
- ¹³D. A. Ramappa, "Surface photovoltaic analysis of phase transformation of copper in p-type silicon," *Appl. Phys. Lett.* **76**(25), 3756 (2000).
- ¹⁴W. B. Henley, D. A. Ramappa, and L. Jastrezbski, "Detection of copper contamination in silicon by surface photovoltaic diffusion length measurements," *Appl. Phys. Lett.* **74**(2), 278 (1999).
- ¹⁵A. Ingelse, J. Lindroos, and H. Savin, "Accelerated light-induced degradation for detecting copper contamination in p-type silicon," *Appl. Phys. Lett.* **107**(5), 052101 (2015).
- ¹⁶S. Rein, T. Rehrl, W. Warta, and S. W. Glunz, "Lifetime spectroscopy for defect characterization: Systematic analysis of the possibilities and restrictions," *J. Appl. Phys.* **91**(4), 2059 (2002).
- ¹⁷D. Macdonald and A. Cuevas, "Validity of simplified Shockley-Read-Hall statistics for modeling carrier lifetimes in crystalline silicon," *Phys. Rev. B* **67**, 075203 (2003).
- ¹⁸W. Shockley and W. T. Read, "Statistics of the recombinations of holes and electrons," *Phys. Rev.* **87**(5), 835–842 (1952).
- ¹⁹R. N. Hall, "Electron-hole recombination in germanium," *Phys. Rev.* **87**(2), 387 (1952).
- ²⁰J. M. Dorkel and P. Leturcq, "Carrier mobilities in silicon semi-empirically related to temperature, doping and injection level," *Solid State Electron.* **24**(9), 821–825 (1981).
- ²¹J. S. Blakemore, *Semiconductor Statistics* (Oxford, 1962).
- ²²D. Macdonald and A. Cuevas, "Trapping of minority carriers in multicrystalline silicon," *Appl. Phys. Lett.* **74**(12), 1710 (1999).
- ²³M. A. Green, "Intrinsic concentration, effective densities of states, and effective mass in silicon," *J. Appl. Phys.* **67**(6), 2944 (1990).

- ²⁴J. Lindroos and H. Savin, "Review of light-induced degradation in crystalline silicon solar cells," *Sol. Energy Mater. Sol. Cells* **147**, 115–126 (2016).
- ²⁵S. Rein, *Lifetime Spectroscopy* (Springer-Verlag, Berlin/Heidelberg, 2005), Vol. 85.
- ²⁶S. Rein and S. W. Glunz, "Electronic properties of interstitial iron and iron-boron pairs determined by means of advanced lifetime spectroscopy," *J. Appl. Phys.* **98**(11), 113711 (2005).
- ²⁷A. A. Istratov and E. R. Weber, "Physics of copper in silicon," *J. Electrochem. Soc.* **149**(1), G21 (2002).
- ²⁸A. A. Istratov, C. Flink, H. Hieslmair, T. Heiser, and E. R. Weber, "Influence of interstitial copper on diffusion length and lifetime of minority carriers in p-type silicon," *Appl. Phys. Lett.* **71**(15), 2121 (1997).
- ²⁹A. Belayachi, T. Heiser, J. P. Schunck, and A. Kempf, "Influence of light on interstitial copper in p-type silicon," *Appl. Phys. A* **80**(2), 201–204 (2005).
- ³⁰I. Tarasov and O. Ostapenko, "Light induced defect reactions in boron-doped silicon: Cu versus Fe," in *Proceedings of the 8th Workshop on Crystalline Silicon Solar Cell Material and Process* (1998), p. 207.
- ³¹M. Saritas and A. Peaker, "Deep states associated with oxidation induced stacking faults in RTA p-type silicon before and after copper diffusion," *Solid State Electron.* **38**(5), 1025–1034 (1995).
- ³²S. D. Brotherton, J. R. Ayres, A. Gill, H. W. van Kesteren, and F. J. A. M. Greidanus, "Deep levels of copper in silicon," *J. Appl. Phys.* **62**(5), 1826 (1987).
- ³³H. Lemke, "Substitutional transition metal defects in silicon grown-in by the float zone technique," in *Proceedings of the Fourth International Symposium on High Purity Silicon* (1996), p. 272.
- ³⁴A. Mesli and T. Héiser, "Defect reactions in copper-diffused and quenched p-type silicon," *Phys. Rev. B* **45**(20), 11632–11641 (1992).
- ³⁵K. Graff, *Metal Impurities in Silicon-Device Fabrication* (Springer, Berlin, Heidelberg, 2000), Vol. 24.
- ³⁶W. Schröter, V. Kveder, M. Seibt, H. Ewe, H. Hedemann, F. Riedel, and A. Sattler, "Atomic structure and electronic states of nickel and copper silicides in silicon," *Mater. Sci. Eng. B* **72**(2–3), 80–86 (2000).
- ³⁷M. Seibt, M. Griess, A. A. Istratov, H. Hedemann, A. Sattler, and W. Schröter, "Formation and properties of copper silicide precipitates in silicon," *Phys. Status Solidi* **166**(1), 171–182 (1998).
- ³⁸A. A. Istratov, H. Hedemann, M. Seibt, O. F. Vyvenko, W. Schröter, T. Heiser, C. Flink, H. Hieslmair, and E. R. Weber, "Electrical and recombination properties of copper-silicide precipitates in silicon," *J. Electrochem. Soc.* **145**(11), 3889 (1998).
- ³⁹M. Seibt, R. Khalil, V. Kveder, and W. Schröter, "Electronic states at dislocations and metal silicide precipitates in crystalline silicon and their role in solar cell materials," *Appl. Phys. A* **96**(1), 235–253 (2009).
- ⁴⁰D. Macdonald, A. Cuevas, S. Rein, P. Lichtner, and S. W. Glunz, "Temperature- and injection-dependent lifetime spectroscopy of copper-related defects in silicon," in *Proceedings of 3rd World Conference on Photovoltaic Energy Conversion* (IEEE, 2003), Vol. 1.
- ⁴¹D. Macdonald, W. Brendle, A. Cuevas, and A. A. Istratov, "Injection-Dependent Lifetime Studies of Copper Precipitates in Silicon," in *Proceedings of the Workshop on Crystalline Silicon Solar Cell Materials and Processes* (2002), pp. 201–204.
- ⁴²M. D. Negaita and T. Y. Tan, "Metallic precipitate contribution to generation and recombination currents in p-n junction devices due to the Schottky effect," *J. Appl. Phys.* **94**(8), 5064 (2003).
- ⁴³A. Hangleiter, "Nonradiative recombination via deep impurity levels in semiconductors: The excitonic Auger mechanism," *Phys. Rev. B* **37**(5), 2594–2604 (1988).
- ⁴⁴W. Kwapił, J. Schon, W. Warta, and M. C. Schubert, "Carrier recombination at metallic precipitates in p-and n-type silicon," *IEEE J. Photovoltaics* **5**(5), 1285–1292 (2015).

Publication III

A.Inglese, H.Vahlman, W.Kwapił, J.Schön, H.Savin. Characterization of light-activated Cu defects in silicon: comparison with the recombination activity of metal precipitates. *Physica Status Solidi (c)*, 14, No. 7, 1700103, 2017.

© 2017 WILEY-VCH Verlag GmbH & Co. KGaA, Weinheim.

Reprinted with permission.

Characterization of light-activated Cu defects in silicon: Comparison with the recombination activity of metallic precipitates

Alessandro Inglese^{*1}, Henri Vahlman¹, Wolfram Kwapił², Jonas Schön², and Hele Savin¹

¹ Department of Electronics and Nanoengineering, Aalto University, 02150 Espoo, Finland

² Fraunhofer Institute for Solar Energy Systems ISE, Heidenhofstraße 2, 79110 Freiburg im Breisgau, Germany

Received 28 February 2017, accepted 7 April 2017

Published online 28 April 2017

Keywords copper impurities, Cu-LID, defect characterization, metal precipitates, silicon

* Corresponding author: e-mail alessandro.inglese@aalto.fi, Phone: +358 50 431 6367

The presence of copper contamination is known to severely degrade the minority carrier lifetime of p-type silicon upon exposure to illumination. In this contribution, we have analyzed the recombination activity of light-activated copper defects in deliberately Cu-contaminated p-type silicon by means of a recombination model that quantitatively defines the effect of metallic precipitates on minority carrier lifetime. The excellent agreement between the model and the experimental data indicates that (i) the formation of Cu precipitates is the probable

root-cause behind Cu-LID and (ii) in the samples examined in this work, the precipitate radius varies between few to several tens of nm with corresponding densities estimated to be in the range of 10^8 – 10^{10} cm⁻³. Further evidence of these results was obtained from the analysis of temperature-dependent lifetime data. While applied here to light-activated copper defects, the procedure described in this article can be applied for characterizing lifetime-limiting precipitates originated by other transition metals (e.g., Fe or Ni).

© 2017 WILEY-VCH Verlag GmbH & Co. KGaA, Weinheim

1 Introduction Copper is a common $3d$ metal impurity in silicon, which produces adverse effects on the operation of state-of-the-art solar cells [1]. Low levels of copper contamination have been shown to severely degrade the minority carrier lifetime in p-type silicon upon exposure to illumination [2–4], thereby impacting the stability of solar cell efficiency during light soaking. This phenomenon, which is referred in literature to as copper-related light-induced degradation (Cu-LID), has been associated to the transformation of recombination-inactive interstitial copper atoms (Cu_i^+) into a different lifetime limiting defect [5]. However, the mechanisms behind Cu-LID and the defect generated during the degradation process still remain a matter of investigation [6]. In a recent contribution, the recombination activity of light-activated copper defects has been studied in terms of Shockley–Read–Hall (SRH) recombination statistics through lifetime spectroscopy methods [7]. The analysis indicated the coexistence of at least two energy levels, i.e., a deep energy state located near the mid-bandgap and a shallow level in the upper bandgap

half, which approximately correspond to the boundaries of the energy range associated to Cu precipitates [8]. Nevertheless, considering the extended nature of metallic precipitates, a rigorous study of carrier recombination at these defects requires the use of more advanced models than simple SRH statistics. A more suitable approach to estimate the impact of metallic precipitates on minority carrier lifetime would be e.g., the model introduced by Plekhanov and Tan [9], which was specifically developed to describe the carrier recombination mechanisms at metallic precipitates.

In the following, the injection and temperature-dependent lifetime results have been analyzed by means of this recombination model. This contribution extends and consolidates the previous studies on the recombination activity of light-activated copper defects. In addition, this work serves as an example of application of this recombination model to complement the existing lifetime spectroscopy methods [10, 11] with the identification and characterization of metallic precipitates.

2 Sample preparation and lifetime measurements

The experiments were performed with Czochralski (Cz-) and Float-Zone (FZ-) Si wafers with resistivities of 3.4 and $1.1 \Omega \cdot \text{cm}$, respectively, and thicknesses of $380 \pm 10 \mu\text{m}$ and $250 \pm 15 \mu\text{m}$. In the Cz-Si sample, the interstitial oxygen concentration was $> 14 \text{ ppm}$.

All samples were thermally oxidized at 900°C in O_2 for 40 min, followed by a 20 min anneal in nitrogen ambient. Bulk Cu contamination was performed with the spin-on method, followed by in-diffusion at 800°C in inert ambient. The interstitial Cu concentration (N_{Cu}) after in-diffusion was estimated to be around $1.0 \times 10^{14} \text{ cm}^{-3}$ for the Cz sample and $1.6 \times 10^{14} \text{ cm}^{-3}$ for the FZ sample [12].

After a $+260 \text{ nC/cm}^2$ corona charge deposition on both wafer surfaces, the samples were degraded under 0.65 Suns illumination at room temperature (RT) for about 100 h. The lifetime decay was constantly recorded as a function of illumination time through the quasi-steady state photoconductance decay (QSSPC) method performed with a Sinton WCT 120-TS lifetime tester [13, 14]. The same technique was utilized for the temperature-dependent measurements, which were performed by heating the measurement stage up to 200°C and subsequently acquiring the data during the cooling transient.

3 Modeling of recombination at metallic precipitates

The recombination model is based upon the assumption that the dominant physical mechanism is the generation of thermionic emission currents due to a Schottky junction between the silicide (Cu precipitate – which exists in Si in the form of Cu_3Si silicides [15]) and the surrounding semiconductor [9]. In this model, the metal precipitate is assumed to be spherical and the extent of the space charge region (SCR) around the silicide is imposed by the junction electric field. Since the excess carrier concentration (Δn), the radius of the metallic precipitate (r_{prec}) and semiconductor doping (N_a) considerably influence the electric fields at the junction (and therefore the width of the SCR), all these parameters ultimately impact the precipitate-related capture cross section.

The quantitative description of precipitate-related recombination as a function of the excess carrier concentration, in general, requires the execution of finite-element simulations, where the continuity equations for holes and electrons are solved together with the Poisson equation. The carrier recombination rate is then calculated by integrating the thermionic emission currents over the silicide/semiconductor interface and averaging over the simulation domain. In order to ease the determination of the precipitate-limited lifetime, Kwapił et al. proposed a parametrization of the numerical results which allows to quickly calculate the injection-dependent lifetime, without the need of numerical simulations. This parametrization consists of a set of equations which estimate the dependence of the precipitate capture cross section (σ_{prec}) on the input parameters, i.e., N_a , Δn and the precipitate radius r_{prec} . The

precipitate-related lifetime is then calculated as follows:

$$\tau_{\text{prec}} = \frac{1}{N_{\text{prec}}(r_{\text{prec}})\sigma_{\text{prec}}(\Delta n, r_{\text{prec}}, N_a)v_{\text{th}}} \quad (1)$$

where N_{prec} is the density of precipitates with radius r_{prec} and v_{th} represents the carrier thermal velocity (10^7 cm/s [11]). Full description of the model and the associated parametrization can be found in Refs. [16] and [17].

4 Results and discussion

4.1 Degradation process

Figure 1 presents the effective lifetime measured during room-temperature illumination in intentionally Cu-contaminated samples. It can be observed that, while in the FZ-specimen the LID effect becomes visible after several tens of minutes, in the Cz-sample the degradation occurs upon exposure to illumination. In order to distinguish the effect of Cu-LID from the boron-oxygen defect (fast and slow components) [18] in the Cz-sample, an identical uncontaminated Cz-wafer has been degraded under the same light source. It turns out that in the Cu-contaminated Cz-sample the initial phase of degradation is dominated by BO-LID (up to ~ 1 min of illumination), whereas the later stages are clearly caused by the formation of light-activated Cu defects. Hence, from the data plotted in Fig. 1 the Cu-LID process in the Cz-Si specimen appears to be considerably faster than in the FZ-Si sample. In the following sections, the defect characterization by means of the Schottky model has been performed on the lifetime data measured after approximately 100 h of uninterrupted illumination, which led to the saturation of the Cu-related lifetime degradation process in both specimens.

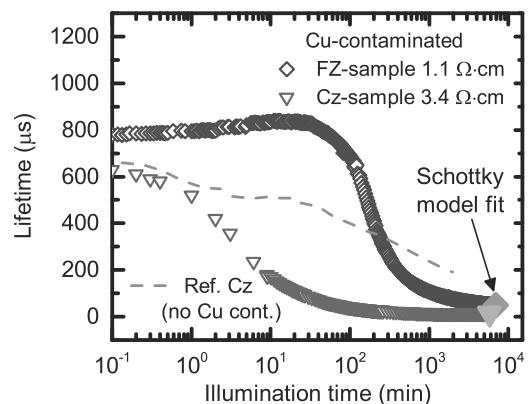


Figure 1 Effective lifetime measured as a function of illumination time at fixed injection level $\Delta n = 0.1 \times N_a$ in Cu-contaminated Cz-Si sample and the FZ-Si sample (purple squares). The dashed line represents the lifetime decay measured with a reference uncontaminated Cz-specimen, whose degradation is solely determined by the light-induced activation of the boron-oxygen complex.

4.2 Fit of injection-dependent lifetime data For the correct analysis of the injection-dependent lifetime data through the Schottky model, the Cu-related lifetime must be separated from the effect of the BO-complex and other recombination channels (e.g., Auger, intrinsic and surface recombination). Figure 2 shows the lifetime related to the light-activated Cu defects (τ_{Cu}), that was calculated by compensating the reciprocal of the effective lifetime measured after degradation (τ_{deg}) with the lifetime curve measured before light soaking (τ_{init}). In the case of the Cz-sample, an additional correction was necessary to subtract the effect of the BO-complex. This was done by compensating τ_{Cu} with the injection-dependent lifetime measured after illumination in a reference uncontaminated sample (τ_{BO}). The superposition of the curves representing ($\tau_{\text{Cu}}^{\text{FZ/Cz}}$) and τ_{deg} over the whole injection range proves that the measured lifetime is largely dominated by the recombination strength of the light-activated Cu defects.

In Fig. 3a, the parametrization of the Schottky model has been fitted to $\tau_{\text{Cu}}(\Delta n)$ with the least squares method assuming that, after LID, the interstitial Cu concentration (N_{Cu}) reported in Section 2 has fully transformed into the recombination active precipitated form. In addition, the fit has been performed under the assumption that all precipitates feature the same size. In other words, for the determination of the precipitate-related lifetime, the entire amount of interstitial Cu atoms has been presumed to transform into precipitates whose size corresponds to an average value. Given these assumptions, the precipitate density N_{prec} of Eq. (1) becomes fixed and it can be written as a function of r_{prec} as follows:

$$N_{\text{prec}}(r_{\text{prec}}) = \frac{N_{\text{Cu}}}{\rho_{\text{Cu}} V_{\text{prec}}(r_{\text{prec}})}, \quad (2)$$

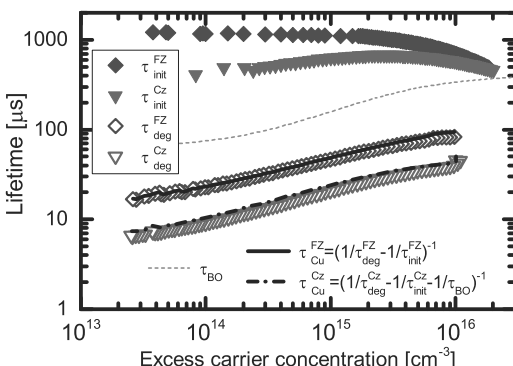


Figure 2 Injection-dependent lifetime curves measured before and after illumination (symbols). Also shown in the image are the effective Cu-related lifetime curves ($\tau_{\text{Cu}}^{\text{FZ}}$ and $\tau_{\text{Cu}}^{\text{Cz}}$) calculated by compensating τ_{deg} with τ_{init} and τ_{BO} .

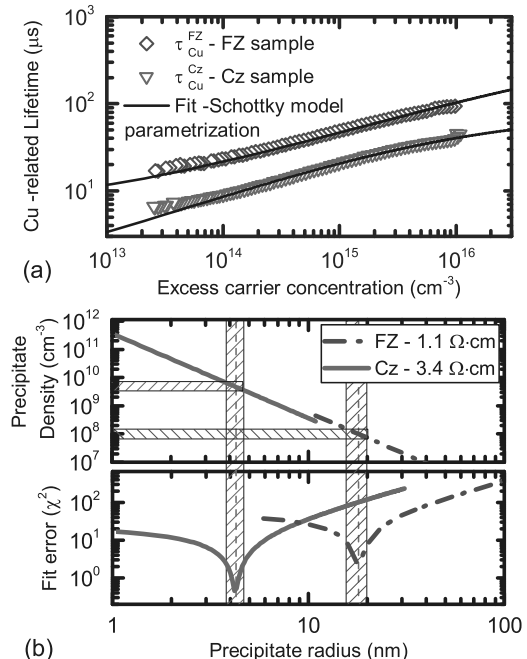


Figure 3 (a) Least squares fit of the injection-dependent Cu-related lifetime. The parameters that provide the best fit to the experimental data are shown in (b) where the precipitate density and the corresponding fit error (χ^2) have been calculated for each value of the precipitate radius. The shaded areas define the values of the precipitate radii/densities that minimize the fit error.

where $\rho_{\text{Cu}} = 6.52 \times 10^{22} \text{ cm}^{-3}$ is the density of Cu atoms in each precipitate [19, 20] and $V_{\text{prec}} = 4/3\pi r_{\text{prec}}^3$ is the precipitate spherical volume.

Although the aforementioned assumptions surely represent an approximation of the real precipitate size distributions, Fig. 3a shows that excellent agreement between the injection-dependent curves predicted by the model and the experimental data. In Fig. 3b, the goodness of fit has been quantified in terms of mean squared sum of residuals (χ^2) for predefined values of precipitate radius/density. It can be observed that in the case of the Cz-specimen with lower resistivity, the optimum fit is obtained with a precipitate radius of $\sim 20 \text{ nm}$ and a density of $\sim 1 \times 10^8 \text{ cm}^{-3}$. On the other hand, the best fit to the lifetime data acquired with the FZ-sample indicates the presence of precipitates with smaller radius ($r_{\text{prec}} \sim 4 \text{ nm}$) and higher density ($N_{\text{prec}} \sim 4 \times 10^9 \text{ cm}^{-3}$).

On the base of the results presented in Figs. 1 and 3, it can be concluded that the slower degradation rate observed in the FZ-Si sample leads to the formation of larger precipitates than the Cz-Si specimen. On the other hand, in the Cz-sample the Cu-LID process is accompanied by the formation of precipitates featuring a smaller radius and capture cross section. In this case, the considerable increase

in estimated precipitate density with respect to the FZ-sample overcompensates the weaker recombination activity of each single precipitate arising from the smaller capture cross section.

Despite the initial simplifying assumption (i.e., the same size for all precipitates), the fitted precipitate radii and densities are in good agreement with the simulated precipitate size distributions reported in Ref. [18]. Hence, the excellent fit to the experimental data in Fig. 3a and the correspondence of the fitted precipitate radii/densities with the results in Ref. [18] strengthen the hypothesis of Cu-precipitation being the root-cause behind the observed LID.

As previously mentioned, the precipitation of Cu impurities has been extensively investigated in recent contributions [12, 18] which presented a comprehensive mathematical model to describe the underlying mechanisms. According to this model, the Cu-precipitation rate is regulated by the solubility of Cu_i atoms. Higher doping concentrations decrease the supersaturation level of Cu_i atoms, which represents the main driving force for Cu precipitation kinetics. Hence, the higher doping level of the FZ-specimen imposes a lower supersaturation level of Cu_i atoms, which slows down the nucleation rate for Cu precipitates and eventually results in the formation of larger precipitates. Heavy B-doping is also known to lower the diffusivity of Cu⁺ atoms due to Cu-B pairing [19]. However, this phenomenon was shown to play a minor effect on the overall doping dependence of Cu precipitation kinetics.

Another factor that might play a role in the different Cu-related degradation rates and precipitate size/density is the possible formation of oxygen precipitates in the Cz-sample during oxidation and the subsequent thermal anneals for in-diffusing Cu impurities. Such oxygen precipitates were shown to remarkably accentuate and accelerate the Cu-LID effects [21].

4.3 Analysis of temperature-dependent lifetime data

In order to further ascertain the agreement between the model and the experimental data, the Schottky model was applied to temperature-dependent lifetime data measured at fixed injection level. As no parametrization exists for modeling the recombination at higher temperatures than 300 K, the lifetime temperature dependence must be calculated through finite element simulations based on the Schottky model [9, 16].

Figure 4 plots the simulated lifetime together with the experimental data detected across the measurable temperature range (300–470 K) at the excess carrier concentration of $2 \times 10^{14} \text{ cm}^{-3}$. The simulated points were calculated assuming the previously determined precipitate radii and densities. In the figure, it can be observed that good agreement exists between the experimental data and the simulated values.

Since all the experimental points in Fig. 3 were measured at fixed injection level and no significant dissolution of Cu precipitates is likely to occur at

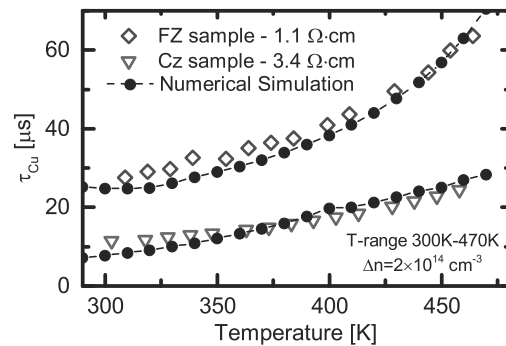


Figure 4 Experimental (open symbols) and simulated (filled circles) lifetime data plotted as a function of temperature. The experimental data were measured at the excess carrier concentration of $2 \times 10^{14} \text{ cm}^{-3}$ and numerical simulations were based on the recombination model described in Section 3.

temperatures below 200 °C [6], on the base of Eq. (1) the variation of the measured lifetime as a function of the temperature may only originate from the temperature-dependence of the minority carrier capture cross section σ_{prec} and the thermal velocity v_{th} . As v_{th} monotonically increases with temperature [11], the upward trend of the measured lifetime at higher temperatures suggests that the capture cross section becomes smaller at increasing temperatures. Specifically, the increase in measured lifetime as a function of temperature suggests that the shrinkage of the capture cross section at higher temperature overcompensates the increase in v_{th} . This result is consistent with the SRH-based analysis presented in Ref. [7], where a good fit to the experimental lifetime data could only be obtained under the assumption of a power-law temperature dependence ($\sigma \sim T^{-\alpha}$) of capture cross sections.

In addition to the effect of temperature and excess carrier concentration on capture cross sections, other phenomena, which were not taken into account in the numerical simulation, may also affect the precipitate-related recombination. For example, charge states exist at the metal/semiconductor interface [9], which increase the interface recombination velocity and, therefore, the overall precipitate-related recombination activity. The augmented thermionic emission at higher temperatures may cause the occupation of such states by the thermally generated carriers, thus reducing the recombination rate at the precipitate. It is, however, questionable whether such phenomenon plays a significant role at temperatures below 200 °C.

Another phenomenon worth mentioning is the possible occurrence of tunneling effects in sub 10 nm precipitates, which was hypothesized in Ref. [22] to define the recombination strength of molybdenum nanoprecipitates. This effect was shown to significantly enhance the majority carrier capture rate due to the increased sharpness of the band bending at the Schottky junction. However, the impact of such phenomenon on the minority capture cross sections

still needs to be quantified and, therefore, further studies are needed to determine whether such tunneling play any role in the results presented above.

5 Conclusions The results presented in this work have shed some new light on the defect causing Cu-LID. The injection and temperature-dependent lifetime data measured with intentionally contaminated wafers have been analyzed by means of a model that quantitatively calculates the carrier recombination at metallic precipitates. The excellent agreement between model and the injection/temperature-dependent lifetime data confirms that Cu precipitates are the probable root-cause behind Cu-LID. The analysis of the experimental data also provided an estimate of the size and density of these precipitates. Particularly, the fitted precipitate radii in the samples used for this study resulted to be in the range of few to several tens of nm and the corresponding density was found to vary between 10^8 and 10^{10} cm^{-3} . For further confirmation, future studies may include electrical characterization via DLTS and high resolution imaging through microscopy techniques (e.g., SIRM or TEM).

Besides providing evidence of Cu precipitates being the defect responsible of Cu-LID, this work serves as an example of application of the Schottky model for the identification and characterization of metallic precipitates. While SRH statistics are well suited for describing carrier recombination at point defects, their application to extended defects leaves behind a certain degree of ambiguity on the exact nature of the underlying defect. This contribution demonstrates that additional information can be gained by complementing SRH-based lifetime spectroscopy analyses with more advanced recombination models.

Acknowledgements The work has been funded by the European Research Council under the European Union's FP7 Programme ERC Grant Agreement No. 307315 (SolarX project). The authors acknowledge the provision of facilities and technical support by Aalto University at the Micronova Nanofabrication Centre. A.I. also acknowledges the financial support of Aalto ELEC doctoral school and Alfred Kordelin Foundation.

References

- [1] T. Turmagambetov, S. Dubois, J.-P. Garandet, B. Martel, N. Enjalbert, J. Veirman, and E. Pihan, Phys. Status Solidi (c) **11**, 1697 (2014).
- [2] H. Savin, M. Yli-Koski, and A. Haarahiltunen, Appl. Phys. Lett. **95**, 152111 (2009).
- [3] A. Inglese, J. Lindroos, and H. Savin, Appl. Phys. Lett. **107**, 052101 (2015).
- [4] A. Inglese, A. Focareta, F. Schindler, J. Schön, J. Lindroos, M. C. Schubert, and H. Savin, Energy Procedia **92**, 808–814 (2016).
- [5] A. Belayachi, T. Heiser, J. P. Schunck, and A. Kempf, Appl. Phys. A **80**, 201 (2005).
- [6] J. Lindroos and H. Savin, Sol. Energy Mater. Sol. Cells **147**, 115–126 (2016).
- [7] A. Inglese, J. Lindroos, H. Vahlman, and H. Savin, J. Appl. Phys. **120**, 125703 (2016).
- [8] M. Seibt, R. Khalil, V. Kveder, and W. Schröter, Appl. Phys. A **96**, 235 (2009).
- [9] P. S. Plekhanov and T. Y. Tan, Appl. Phys. Lett. **76**, 3777 (2000).
- [10] S. Rein, Lifetime Spectroscopy (Springer-Verlag, Berlin/Heidelberg, 2005).
- [11] S. Rein, T. Rehrl, W. Warta, and S. W. Glunz, J. Appl. Phys. **91**, 2059 (2002).
- [12] H. Vahlman, A. Haarahiltunen, W. Kwapił, J. Schön, A. Inglese, and H. Savin (submitted).
- [13] B. B. Paudyal, K. R. McIntosh, D. H. Macdonald, B. S. Richards, and R. A. Sinton, Prog. Photovoltaics Res. Appl. **16**, 609 (2008).
- [14] R. A. Sinton, A. Cuevas, and M. Stuckings, in *Conf. Rec. 25th IEEE Photovolt. Spec. Conf. – 1996* (IEEE, 1996), pp. 457–460.
- [15] W. Schröter, V. Kveder, M. Seibt, H. Ewe, H. Hedemann, F. Riedel, and A. Sattler, Mater. Sci. Eng. B **72**, 80 (2000).
- [16] W. Kwapił, J. Schon, F. Schindler, W. Warta, and M. C. Schubert, IEEE J. Photovoltaics **4**, 791–798 (2014).
- [17] W. Kwapił, J. Schon, W. Warta, and M. C. Schubert, IEEE J. Photovoltaics **5**, 1285–1292 (2015).
- [18] H. Vahlman, A. Haarahiltunen, W. Kwapił, J. Schön, A. Inglese, and H. Savin (submitted).
- [19] A. A. Istratov and E. R. Weber, J. Electrochem. Soc. **149**, G21 (2002).
- [20] M. Yli-Koski, *Optical Activation of Copper in Silicon Studied by Carrier Lifetime Measurements* (Doctoral dissertation – Helsinki University of Technology, 2004).
- [21] H. Väinölä, M. Yli-Koski, A. Haarahiltunen, and J. Sinkkonen, J. Electrochem. Soc. **150**, G790 (2003).
- [22] J. Jacobs, B. Hamilton, S. Leonard, V. P. Markevich, and A. R. Peaker, in *2015 IEEE 42nd Photovolt. Spec. Conf.* (IEEE, 2015), pp. 1–3.

Publication IV

H.Vahlman, A.Haarahiltunen, W.Kwapił, J.Schön, A.Inglese, H.Savin. Modeling of light-induced degradation due to Cu precipitation in p-type silicon. Part II: Comparison of simulations and experiments. *Journal of Applied Physics*, 121, 195704, 2017.

© 2017 American Institute of Physics Publishing LLC.
Reprinted with permission.

Modeling of light-induced degradation due to Cu precipitation in p-type silicon. II. Comparison of simulations and experiments

H. Vahlman,^{1,a)} A. Haaralahtiunen,¹ W. Kwapił,² J. Schön,² A. Inglese,¹ and H. Savin¹

¹Department of Electronics and Nanoengineering, Aalto University, Tietotie 3, 02150 Espoo, Finland

²Fraunhofer Institute for Solar Energy Systems ISE, Heidenhofstr. 2, 79110 Freiburg, Germany

(Received 30 January 2017; accepted 1 May 2017; published online 15 May 2017)

The presence of copper impurities is known to deteriorate the bulk minority carrier lifetime of silicon. In p-type silicon, the degradation occurs only under carrier injection (e.g., illumination), but the reason for this phenomenon called copper-related light-induced degradation (Cu-LID) has long remained uncertain. To clarify the physics of this problem, a mathematical model of Cu-LID was introduced in Paper I of this article. Within the model, kinetic precipitation simulations are interlinked with a Schottky junction model for electric behavior of metallic precipitates. As this approach enables simulating precipitation directly at the minority carrier lifetime level, the model is verified in this second part with a direct comparison to the corresponding degradation experiments and literature data. Convincing agreement is found with different doping and Cu concentrations as well as at increased temperature, and in the dark, both simulated degradation and measured degradation are very slow. In addition, modeled final lifetimes after illumination are very close to experimental final lifetimes, and a correlation with the final precipitate size is found. However, the model underestimates experimentally observed differences in the degradation rate at different illumination intensities. Nevertheless, the results of this work support the theory of Cu-LID as a precipitate formation process. Part of the results also imply that heterogeneous nucleation sites play a role during precipitate nucleation. The model reveals fundamental aspects of the physics of Cu-LID including how doping and heterogeneous nucleation site concentrations can considerably influence the final recombination activity. *Published by AIP Publishing.*

[<http://dx.doi.org/10.1063/1.4983455>]

I. INTRODUCTION

A complete mathematical model for simulating copper-related light-induced degradation (Cu-LID) at the minority carrier lifetime level was proposed in Paper I⁴⁵ of this two-part contribution. In the following, the contents of the first part are briefly summarized to provide a context for the results presented in this paper in which the model is verified with experiments. Based on earlier findings in the literature, reviewed in Paper I, it is conceivable that Cu-LID is a precipitation process of positively charged interstitial Cu (Cu_i^+) ions, forming metallic Cu_3Si precipitates that are highly recombination active in the Si bulk. Therefore, the model is based on a fundamental premise according to which the evolution of a supersaturated solid solution of interstitial Cu toward its thermal equilibrium precipitated state is retarded, in p-type Si, by electrostatic repulsion from the positively charged Cu_3Si precipitate nuclei. Growth and dissolution rates of a kinetic precipitation model, originally derived for electrically neutral spherical precipitates, were modified to include this electrostatic effect. In addition, a Schottky junction model^{1–4} for metallic precipitates in Si was utilized to calculate the precipitate-related electric field. Consequently, it was shown that the magnitude of the electric field can vary considerably depending on the excess electron concentration and that precipitation kinetics can change even five orders of

magnitude depending on whether the sample is illuminated or resides in the dark. This kinetic effect was interpreted to provide a possible explanation for Cu-LID. Since the mentioned Schottky model also allows the calculation of the precipitate-limited minority carrier lifetime, the full procedure for simulating lifetime degradation due to Cu precipitation with respect to illumination time was described.

Several aspects of Cu-LID have been studied experimentally in previous articles, where, for example, dependences on Cu concentration,⁵ temperature,^{5,6} bulk microdefect density,⁷ substrate growth method,^{8,9} dopant concentration,⁵ and dopant type¹⁰ have been addressed. In this article, in addition to providing new experimental data, we take another look at some of the previously published results. The fact that the proposed model works at the minority carrier lifetime level, which is one of the most accessible quantities describing the properties of a semiconductor, makes comparison to experiments particularly straightforward. Consequently, internal mechanisms of the model can be studied to understand fundamental changes imposed on the precipitation process when, for example, the above mentioned material and environmental parameters are varied. Due to the fact that a high density of small precipitates can provide a considerably larger recombination surface for minority charge carriers than a low density of large precipitates, the details of the precipitate nucleation and growth process are important from the point of view of final recombination activity of Cu-LID. Therefore, in addition to providing an estimation of the final precipitate

^{a)}Electronic mail: henri.vahlman@aalto.fi.

size, we are able to specify factors (e.g., doping and heterogeneous nucleation site concentrations) that influence recombination losses deriving from this defect mechanism.

II. MATERIALS AND METHODS

A. Experimental details

Table I summarizes the wafer types analyzed in this work. All wafer types are boron-doped $\langle 100 \rangle$ -oriented monocrystalline electronic-grade silicon. Interstitial oxygen concentrations, $[O_i]$, in Table I are given by the manufacturer for the Czochralski (Cz) wafers, and a typical (very low) value is reported for the float zone (FZ) material.

The wafers were cleaned with the standard RCA process and surface passivated by thermal oxidation at 900°C for 40 min in O_2 , followed by a 20 min anneal at 900°C in the N_2 atmosphere. Cu contamination was performed with the spin coating method using a 1 ppm (w/v) Cu solution, followed by in-diffusion at 800°C in an N_2 atmosphere for 20 min. The wafers were pulled out of the furnace at 800°C and cooled in air. Temperature ramp during cooling was measured from the wafer surface with an infrared thermometer. With the 1 ppm solution, the in-diffused bulk interstitial Cu concentration, marked $C_{\text{Cu}}^{\text{init}}$ in the text, was estimated to be $0.76 \times 10^{14} \text{ cm}^{-3}$, $1 \times 10^{14} \text{ cm}^{-3}$, and $1.6 \times 10^{14} \text{ cm}^{-3}$ in $525 \mu\text{m}$, $400 \mu\text{m}$, and $250 \mu\text{m}$ thick wafers, respectively. These estimations are based on earlier work involving transient ion drift [TID, detection limit $\sim 10^{11} \text{ cm}^{-3}$ (Ref. 11)] measurements,⁷ and assuming that the in-diffused concentration scales directly with a wafer thickness. To prevent out-diffusion of the interstitial Cu ions and improve surface passivation provided by the thermal oxide, the wafers were double-side corona charged with a surface charge of $+260 \text{ nC cm}^{-2}$.

The wafers were illuminated using either an LED lamp (illumination intensity corresponding to < 1 sun) with a peak wavelength at 540 nm or a halogen lamp (≥ 1 sun) with a slightly broader spectrum peaking at 590 nm . Illumination intensity ($0.003\text{--}1.8$ sun) was measured using a Si photodiode-based pyranometer. The wafer surface temperature was monitored with a K-type thermocouple, verifying that the wafer surface temperature remained at approximately 25°C under illumination. The minority carrier lifetime was measured with Sinton Instruments WCT-120 quasi-steady-state photoconductance (QSSPC) lifetime measurement equipment using a peak flash intensity of $\sim 5 \text{ W cm}^{-2}$ at room temperature (RT). The lifetime was measured as a function of illumination time manually (for illumination intensity ≥ 1 sun) or with an automated setup (< 1 sun) such that at preset intervals the LED lamp

TABLE I. Details of the wafer types analyzed in this work, including the growth method, resistivity, wafer thickness, and interstitial oxygen concentration $[O_i]$.

Wafer type	Growth method	Resistivity ($\Omega \text{ cm}$)	Thickness (μm)	$[O_i]$ (cm^{-3})
Low-res FZ	FZ	1.0	250	$< 1 \times 10^{16}$
Low-res Cz	Cz	3.4–3.9	400	$> 7 \times 10^{17}$
High-res Cz	Cz	18–22	525	$5.5\text{--}6.5 \times 10^{17}$

turned off for the duration of the QSSPC measurement while the sample remains on the QSSPC stage throughout the measurement of the entire LID curve. This minimizes the error from the slightly varying measurement position and inaccuracy in illumination time associated with manual measurements, which involve moving the sample between the lamp and the QSSPC stage. Unless otherwise mentioned, the lifetime is reported at an excess carrier concentration $\Delta n_e = 0.1 \times N_a$, where N_a is the acceptor concentration.

The generation rate in the wafers, required for the simulations, was determined from

$$G = \left(\int_0^{hc/E_G} \frac{E(\lambda)}{hc/\lambda} \times (1 - R(\lambda)) d\lambda \right) / w, \quad (1)$$

where λ is the wavelength of light, $E(\lambda)$ is the spectral irradiance of the light source at wavelength λ , $R(\lambda)$ is the λ -dependent front reflectance of the wafer, h is the Planck constant, c is the speed of light in air, E_G is the energy gap of Si, and w is the wafer thickness. Spectral irradiance was measured with a USB spectrometer, and the front reflectance with a ultraviolet-visible-near infrared (UV-VIS-NIR) spectrometer. Due to the thickness of the wafers and the illumination spectra of the LED and the halogen light sources lacking wavelengths above 860 nm , transmittance through the wafer was considered negligible.

B. Details of calculating the effective minority carrier lifetime

The simulated effective lifetime, τ_{eff} , was calculated assuming five different recombination channels, including the Cu precipitates, fast recombination center (FRC) and slow recombination center (SRC) of the boron-oxygen (BO) defect, Auger/radiative recombination, and background/surface recombination. Instead of the full model, the precipitate-limited lifetime at RT was calculated using a parametrization based on the Schottky junction model.⁴ Nevertheless, at the relevant excess carrier concentration interval of $\Delta n_e = 10^{12}\text{--}10^{16} \text{ cm}^{-3}$, the full model has been found to provide results that are practically independent of the exact value of the Schottky barrier height as measured from the conduction band edge, Φ_{Bn} , in a range from 0.45 to 0.7 eV. Therefore, lifetimes determined from the parametrization do not significantly differ from the results provided by the full model in the mentioned Φ_{Bn} range.⁴

Initial injection-dependent τ_{eff} , assumed to be limited by background, surface, Auger, and radiative recombination, was taken from experimental QSSPC data separately for each sample. If this experimental information was unavailable (in the case of LID data from the literature), an injection-independent background/surface recombination-limited lifetime was assigned, which was corrected for Auger and radiative recombination with the parametrization of Richter *et al.*¹² This simplification was found to have negligible effects on simulation results at intensities exceeding 0.1 sun.

Since the Cz wafers in Table I have a high O_i concentration, they are, in addition to Cu-LID, also susceptible to LID

due to the BO defect.¹³ The effect of the BO defect was calculated via the Shockley–Read–Hall (SRH) statistics using parametrized models of injection-dependent lifetime and recombination activity for both FRC¹⁴ and SRC,^{15–17} where the rate constants were taken from Schön *et al.*¹⁸ Based on a comparison between experimental lifetime data and the lifetime given by the BO parametrization, the FRC defect concentration was found to vary between a value defined by the parametrization and a lower value, most likely due to uncontrolled degradation between sample processing and the first lifetime measurement. Therefore, to obtain good fits to experimental data, the FRC stage defect concentration was adjusted for each sample separately. However, the FRC defect considerably affects the lifetime only in the beginning of degradation, whereas its influence decreases toward the end, and the effect on the final lifetime is negligible (seen later, e.g., in Fig. 1). In the case of high-res Cz, the defect concentration of the slow SRC stage was calculated based on the parametrization of Bothe *et al.*¹⁷ using $[O_i] = 6 \times 10^{17} \text{ cm}^{-3}$ as given by the manufacturer. In the case of low-res Cz, however, with the minimum $[O_i] = 7 \times 10^{17} \text{ cm}^{-3}$ given by the manufacturer the parametrization resulted in too low BO defect-limited lifetime ($\sim 75 \mu\text{s}$ at $\Delta n_e = 0.1 \times N_a$) as compared to experimental data (130–180 μs) obtained with reference wafers without Cu contamination. To improve agreement between experiments and parametrization in this case, the SRC defect concentration given by the parametrization with $[O_i] = 7 \times 10^{17} \text{ cm}^{-3}$ was multiplied by a fixed factor of 0.43, and the obtained defect concentration value was then used in the case of all low-res Cz samples of this work (seen later e.g., Fig. 1).

In addition to Cu-LID and the BO defect, another possible source of light-induced changes in τ_{eff} comes from possible parasitic iron contamination from the Cu contamination

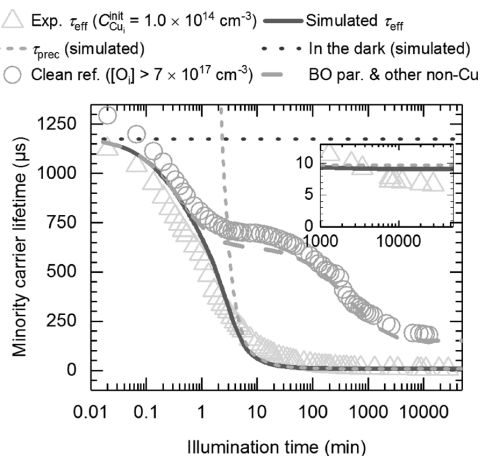


FIG. 1. Experimental Cu-LID ($[\text{Cu}] = 1 \times 10^{14} \text{ cm}^{-3}$) and BO-LID (clean reference) under 0.65 sun intensity at RT compared to simulated τ_{eff} , τ_{prec} , and BO defect-limited minority carrier lifetime according to the modified parametrization (with $[O_i] = 7 \times 10^{17} \text{ cm}^{-3}$, see Sec. II B) corrected for other mechanisms including background, surface, Auger, and radiative recombination. The blue dotted curve shows how the simulated lifetime remains high in the dark. Lifetimes are reported at an excess carrier concentration $\Delta n_e = 0.1 \times N_a$. The inset is a zoom from 1000 min to the end of the time scale.

process and consequent dissociation of Fe–B pairs to the interstitial species, Fe_i , during QSSPC measurements. Macdonald *et al.*¹⁹ reported that a threshold flash intensity of 5 W cm^{-2} is required for Fe–B dissociation. We use this exact QSSPC flash intensity, meaning that Fe–B dissociation may occur. The influence of iron on LID curves is analyzed in Sec. III A using SRH statistics with Fe-related capture cross sections from Ref. 20.

III. COMPARISON BETWEEN MODEL AND EXPERIMENTS

A. Minority carrier lifetime evolution under illumination and in the dark

In Fig. 1, experimental LID data are compared with simulations and divided into components due to Cu precipitation and BO-LID. Here, we first discuss only the experimental result, and the simulations are treated separately below. Triangles show the experimental minority carrier lifetime evolution of a low-res Cz wafer with an in-diffused interstitial Cu concentration of $C_{\text{Cu}}^{\text{init}} = 1 \times 10^{14} \text{ cm}^{-3}$, illuminated under 0.65 sun at RT. The experimental curve shows several distinct phases of LID, the first one taking place on a time-scale of few minutes. The first phase can be closely associated with the FRC stage of the BO defect, as can be seen by comparing with the non-contaminated (clean) reference wafer in Fig. 1 (gray circles) and the lifetime given by the BO parametrization modified as described in Sec. II B (gray dashed line), corrected for the background, surface, Auger, and radiative recombination. The second degradation phase in the experimental curve causes a steep decline after a few minutes of illumination. Based on the BO parametrization, this phase cannot be explained with the BO defect and must therefore be caused by Cu. In addition, the samples of this work exhibit an asymptotic degradation phase with very slow degradation even after thousands of minutes of illumination, which was earlier observed in Ref. 5.

The experimental initial τ_{eff} of the Cu contaminated wafer in Fig. 1 is high and equal in magnitude to that in the clean reference wafers of this and earlier work,⁵ which implies that at the beginning the lifetime is not limited by Cu precipitates. In addition, it has earlier been confirmed with TID measurements that the slower cooling ramp of air cooling (on average $\sim 4 \text{ K/s}$ from 800°C to 100°C as measured in this work) compared to fast quenching (comparable to a typical $60\text{--}100 \text{ K/s}$ after solar cell metallization firing in the industry²¹) does not influence the interstitial Cu concentration after in-diffusion.⁷ This implies that a negligible fraction of Cu precipitates during cooldown in both cases. This result is further supported by another study in which complete out-diffusion of Cu was observed after a pull-out from 800°C and removal of surface oxide with similar Cu contamination levels as used in current work.²² Therefore, since also the dark storage time of the wafers was kept brief (on the order of days) in comparison to several months it takes for any visible degradation to occur,^{7,23} the simulations of this work were performed assuming that the initial interstitial Cu concentration, $C_{\text{Cu}}^{\text{init}}$, is the same as the in-diffused concentration, and no significant precipitation has occurred prior to illumination.

The possibility that Fe could influence the LID behavior was tested with a Cu-contaminated ($C_{\text{Cu}}^{\text{init}} = 0.8 \times 10^{14} \text{ cm}^{-3}$) and partially degraded low-res FZ sample ($N_a = 1.6 \times 10^{16} \text{ cm}^{-3}$) by subjecting it to repeated flashes from the QSSPC setup after first keeping it in the dark for several days. A τ_{eff} increase from $317 \mu\text{s}$ (at $\Delta n_e = 0.1 \times N_a$) after the first flash to a saturated value of $\sim 348 \mu\text{s}$ after 20 flashes was observed, which did not increase further despite 150 flashes being recorded in total. According to SRH statistics, this increase in τ_{eff} corresponds to [Fe] of $\sim 2 \times 10^{10} \text{ cm}^{-3}$ assuming that all Fe–B pairs dissociate. Since measuring a single point in the LID curve involves two flashes, it is likely that in the beginning of the LID curve with short measurement intervals the majority of Fe exists as Fe_i , whereas at the end when the intervals are longer ($\geq 120 \text{ min}$) Fe–B pairs dominate since the majority of Fe_i is expected to re-associate.²⁴ Nevertheless, the effect of Fe is small at low τ_{eff} when Cu precipitates are the main limiting defects (maximum increase of τ_{eff} upon full Fe–B dissociation to Fe_i diminishes to $\sim 0.7 \mu\text{s}$ at $\tau_{\text{eff}} = 50 \mu\text{s}$). In lower doped low-res Cz in Fig. 1 ($N_a = 3.8 \times 10^{15} \text{ cm}^{-3}$), the maximum increase with similar [Fe] is even smaller, $\sim 0.4 \mu\text{s}$ at $\tau_{\text{eff}} = 50 \mu\text{s}$ and $\sim 0.01 \mu\text{s}$ at $\tau_{\text{eff}} = 10 \mu\text{s}$ (at $\Delta n_e = 0.1 \times N_a$). Since Fe does not notably affect analysis of Cu precipitation, dissociation and re-association kinetics of Fe-related defects was not considered in simulated LID curves of this work.

The results of simulations are reported in Fig. 1 as a solid line representing the effective lifetime, τ_{eff} (simultaneously due to Cu precipitates, the BO defect, and background, surface, Auger, and radiative recombination). The simulated τ_{eff} has been reproduced by setting the energetic terms of Eq. (2) in Paper I to $\Delta G_S = 0$ and $\gamma = 0.615 \times 10^{-4} \text{ J cm}^{-2}$, corresponding to the free energy change per precipitate volume due to strain and the interface energy, respectively, and the kinetics-related chemical activation barrier of Eq. (14) in Paper I to $\Delta G_{\text{act}} = 0$ (note that these values will be used throughout this study, and a physical interpretation will be given later in the text). Hence, the precipitate-limited lifetime, τ_{prec} , given by the Schottky model and shown in Fig. 1 as a yellow dashed line, starts limiting τ_{eff} at a similar illumination time ($\sim 2 \text{ min}$) as in the experimental data. The simulated τ_{eff} shows two separate degradation stages that are similar to the first two phases in the experimental data, and the final lifetimes are close to each other (i.e., $9.1 \mu\text{s}$ according to the simulation and $6.7 \mu\text{s}$ experimentally). However, the model does not reproduce the asymptotic degradation phase extending beyond thousands of minutes that was visible in the experimental data.

An important aspect to confirm with the fitted values of ΔG_S , γ , and ΔG_{act} is that precipitation in the dark should be very slow, as previously experimentally shown for Cu concentrations notably lower than N_a such as used in this work.^{7,11,23,25,26} The blue dotted curve in Fig. 1 shows simulated τ_{eff} (BO defect omitted) of a low-res Cz wafer as a function of time when $\Psi_n^S = 0.31 \text{ V}$, corresponding to the thermal equilibrium built-in voltage when Φ_{BH} is set to 0.59 eV (a value associated with the Si– Cu_3Si interface²⁷). In this case, the model predicts very slow precipitation, and τ_{eff} remains at the value limited by the background, surface, Auger-, and

radiative recombination for ~ 3 weeks (500 h). However, the simulated degradation is faster than experimentally, where Cu contaminated wafers have been observed to preserve degradation-free over several months.^{7,23} Therefore, it is possible that the model somewhat overestimates the degradation rate in thermal equilibrium conditions. Nonetheless, in the dark at RT, after 3 months the simulated lifetime is still $\sim 360 \mu\text{s}$, and full degradation does not occur until ~ 2.5 years. In this context, it was also verified that few days of simulated darkness before modeling the LID behavior under illumination does not influence the results in any visible way.

B. Cu concentration dependence

The response of the model on a change in Cu concentration was tested with published data from Lindroos and Savin,⁵ obtained with similar wafers which also underwent the same processing steps as the low-res Cz material in Table I. Figure 2 shows experimental LID curves with two different $C_{\text{Cu}}^{\text{init}}$ of $0.5 \times 10^{14} \text{ cm}^{-3}$ and $1 \times 10^{14} \text{ cm}^{-3}$, both illuminated under 1 sun. Note that Fig. 2 is divided into two subfigures, where the only difference is that in (a) the minority carrier lifetime scale is linear, whereas in (b) the scale is logarithmic. The sample with the higher Cu concentration degraded faster and saturated to a lower lifetime than the sample with the lower Cu concentration, that is, $7.6 \mu\text{s}$ and $21 \mu\text{s}$, respectively. Simulation results are shown as lines on top of the experimental LID data, and the BO defect-limited lifetime according to the parametrization (where the FRC defect concentration was adjusted to fit the $C_{\text{Cu}}^{\text{init}} = 0.5 \times 10^{14} \text{ cm}^{-3}$ data) is shown for comparison as a dashed gray line. During the simulations, the energetic and kinetic terms were kept fixed at the same values as above ($\Delta G_S = 0$, $\gamma = 0.615 \times 10^{-4} \text{ J cm}^{-2}$, and $\Delta G_{\text{act}} = 0$). The LID behavior is approximately reproduced with simulated final τ_{eff} of $9.3 \mu\text{s}$ and $29 \mu\text{s}$ in the case of the higher and the lower Cu concentration, respectively. Comparing the linear scale of Fig. 2(a) to the logarithmic scale of Fig. 2(b), the latter reveals more clearly that the slope of the effective lifetime is overestimated by the model in comparison to experiments, which derives from excessively steep descent of τ_{prec} . Therefore, the model deviates from experiments in either the lower ($10\text{--}100 \mu\text{s}$) or the higher ($>100 \mu\text{s}$) lifetime range. A possible reason for this deviation will be discussed in Sec. IV E. Nevertheless, despite less than perfect agreement between simulations and experiments, the degradation rates and final degraded lifetimes between different samples are in qualitative correlation.

C. Intensity dependence

As discussed in Paper I of this article, injection conditions can considerably influence the precipitation kinetics. It is therefore relevant to investigate how well the modeled lifetime evolution agrees with experimental data at different illumination intensities. A comparison of experimental and simulated LID at intensities from 0.003 to 1.8 sun is presented in Fig. 3, where the samples correspond to low-res Cz wafers with $C_{\text{Cu}}^{\text{init}} = 10^{14} \text{ cm}^{-3}$. Note that the difference in initial lifetime between 0.003 sun and 0.11 sun data derives from a difference in the initially recombination active FRC

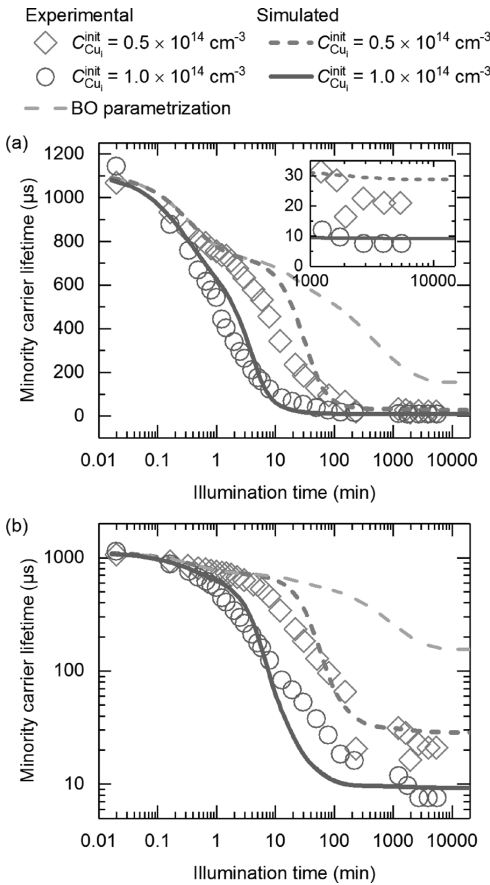


FIG. 2. Comparison of simulated LID curves with experimental data at two different Cu concentrations illuminated under 1 sun. Experimental data are from Ref. 5, and BO-limited lifetime was calculated with the modified parametrization assuming $[O_i] = 7 \times 10^{17} \text{ cm}^{-3}$ (see Sec. II B). The same graph is shown with both linear (a) and logarithmic (b) minority carrier lifetime-scales. Lifetimes are reported at an excess carrier concentration $\Delta n_e = 0.1 \times N_a$. The inset in (a) is a zoom from 1000 min to the end of the time scale.

defect concentration, whereas the low initial lifetime of the 1.8 sun data may be related to a poorer surface oxide quality since this sample was processed in a separate batch in which low initial lifetimes were measured also in other samples. It was verified with the BO parametrization used in this work that the considerable intensity dependence of the experimental data differs from the limited intensity dependence of BO-LID²⁸ and therefore derives from Cu-LID. At the lowest intensity of 0.003 sun, the degradation continued even after 65 000 min (45 days). To speed up the degradation in this case, intensity was increased to 0.65 sun at a point marked with the asterisk (*) symbol, after which the lifetime degraded to a similar value ($6.7 \mu\text{s}$) as with higher intensities.

The intensity dependence of Cu-LID was modeled using the same energetic and kinetic terms as above ($\Delta G_S = 0$, $\gamma = 0.615 \times 10^{-4} \text{ J cm}^{-2}$, and $\Delta G_{\text{act}} = 0$) and the generation rate G was redetermined for each intensity using Eq. (1). The results, shown in Fig. 3 as lines on top of the experimental

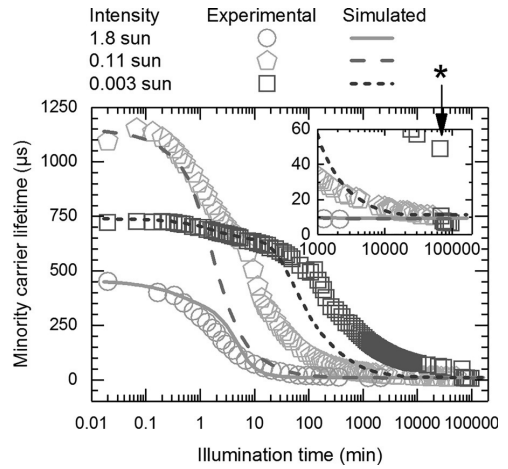


FIG. 3. Intensity dependence of Cu-LID according to experiments and simulations, taking also the BO-LID into account. Lifetimes are reported at an excess carrier concentration $\Delta n_e = 0.1 \times N_a$. The inset is a zoom from 1000 min to the end of the time scale. In the case of the 0.003 sun data, the intensity was increased to 0.65 sun after the point marked with an asterisk (*).

data, show that while the highest intensity is reproduced by the model relatively well, at lower intensities the rate of degradation is clearly overestimated. This discrepancy will be further discussed in Sec. IV C.

D. Temperature dependence: Accelerated LID

Temperature dependence of the model was tested with published data from Inglese *et al.*⁶ In the mentioned study, similar samples as used in this work (low-res Cz wafers with $C_{\text{Cu}}^{\text{init}} = 10^{14} \text{ cm}^{-3}$) were degraded at an elevated temperature of 120°C and found to exhibit so called accelerated LID (ALID) behavior, that is, a considerable increase in the degradation rate of Cu-LID was observed in comparison to Cu-LID at RT (RT-LID). A comparison of Cu-related ALID and RT-LID under 0.5 sun illumination is presented in Fig. 4. Experimentally, the degradation rate is considerably higher in ALID conditions, while the final lifetime remains in a similar order of magnitude as in the case of RT-LID. The degradation behavior cannot be explained by the BO defect in either case, as can be seen by comparing the experimental data with the brown and gray dashed lines in Fig. 4, which show the BO- and background/surface-limited lifetime in conditions corresponding to ALID and RT-LID, respectively. Simulated τ_{eff} curves are shown as lines on top of the experimental data (with the same values of the energetic and kinetic terms as above). It is noteworthy that, in comparison to experiments, the rate of degradation is overestimated by the simulations in both cases. This overestimation of the degradation rate most likely derives from the fact that, as discussed above in Sec. III C, the model seems to overestimate the degradation rate when the intensity is lowered (from 0.65 sun in Fig. 1 to 0.5 sun in this case). However, the main experimental characteristics of Cu-related ALID, namely, the increased rate of degradation and the similar final

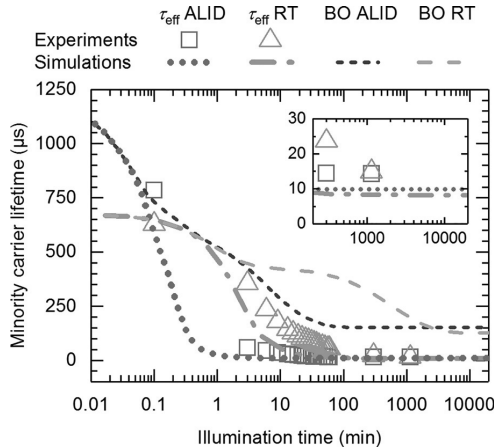


FIG. 4. Cu-related accelerated LID as predicted by the model and compared to experimental data from Ref. 6. The illumination intensity was 0.5 sun, and both samples were low-res Cz wafers with $C_{\text{Cu}_i}^{\text{init}} = 10^{14} \text{ cm}^{-3}$. Consistent with Ref. 6, the lifetimes are reported at an excess carrier concentration of $\Delta n_e = 3 \times 10^{14} \text{ cm}^{-3}$. The inset is a zoom from 200 min to the end of the time scale.

lifetime as in the case of RT-LID, are clearly visible in the simulated curves of Fig. 4.

E. Doping dependence

To investigate the effect of doping, samples with different resistivities were studied. First, Fig. 5 shows the LID curve of a low-res FZ wafer ($N_a = 1.5 \times 10^{16} \text{ cm}^{-3}$) with $C_{\text{Cu}_i}^{\text{init}} = 1.6 \times 10^{14} \text{ cm}^{-3}$ under 0.65 sun, together with the LID curve of a low-res Cz wafer ($N_a = 3.8 \times 10^{15} \text{ cm}^{-3}$) with $C_{\text{Cu}_i}^{\text{init}} = 1 \times 10^{14} \text{ cm}^{-3}$, also under 0.65 sun, and earlier shown in Fig. 1. In the case of the low-res FZ sample, the FRC stage of the BO defect is absent due to an O_i concentration typically two orders of magnitude lower than in Cz wafers. Although illumination-induced minority carrier lifetime instabilities not related to the BO defect have been earlier reported in the FZ material,^{29,30} our non-contaminated

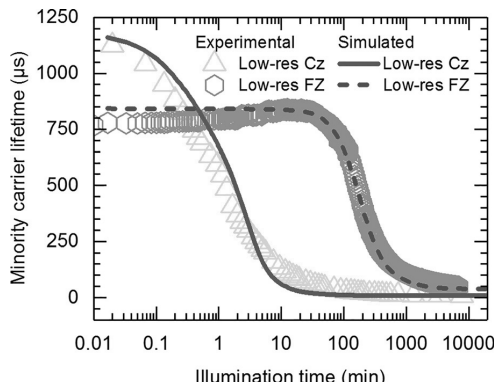


FIG. 5. Experimental and modeled Cu-LID in low-res FZ and low-res Cz samples illuminated under 0.65 sun at RT. Lifetimes are reported at an excess carrier concentration $\Delta n_e = 0.1 \times N_a$.

reference samples (not shown) showed no degradation under 0.65 sun illumination at RT for 10^4 min. It is therefore clear that, similarly to Ref. 31, the observed LID of the FZ sample in Fig. 5 arises solely from Cu-LID. On the other hand, as it was shown in Fig. 1 that the effective lifetime of the low-res Cz sample becomes heavily limited by Cu-LID after only few minutes of illumination, it can be concluded that Cu-LID is considerably slower in the low-res FZ than in the low-res Cz sample even despite the higher $C_{\text{Cu}_i}^{\text{init}}$ in the former. Simulated τ_{eff} (with the same energetic and kinetic terms $\Delta G_S = 0$, $\gamma = 0.615 \times 10^{-4} \text{ J cm}^{-2}$, and $\Delta G_{\text{act}} = 0$ as above), shown as lines, are in agreement with the experiments with coinciding degradation rates and final lifetimes. The final lifetime was $48 \mu\text{s}$ experimentally and $40 \mu\text{s}$ according to the simulation in the case of low-res FZ, which are notably higher than the respective values of $6.7 \mu\text{s}$ and $9.1 \mu\text{s}$ in the case of low-res Cz. Therefore, the experimentally observed difference between degradation rates and final lifetimes can be fully explained by the effect of differing doping concentrations on Cu-LID. The reason why doping can influence the results so heavily will be further discussed in Sec. IV.

In order to widen the doping range studied in this work, experimental data of a high-res Cz wafer ($N_a = 6.0 \times 10^{14} \text{ cm}^{-3}$) with $C_{\text{Cu}_i}^{\text{init}} = 0.76 \times 10^{14} \text{ cm}^{-3}$ from Ref. 5, illuminated under 1 sun, are shown in Fig. 6 with red pentagons. Comparison with the BO defect-limited lifetime for the high-res Cz sample (gray dashed line) confirms that degradation of this sample derives from Cu-LID rather than BO-LID. Also shown for comparison are the experimental and modeled τ_{eff} of the 1 sun-illuminated low-res Cz wafer with $C_{\text{Cu}_i}^{\text{init}} = 1 \times 10^{14} \text{ cm}^{-3}$, reported in Fig. 2. In Fig. 5, a fourfold increase in N_a

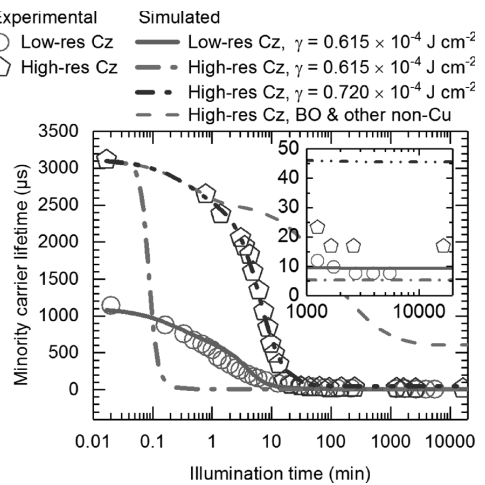


FIG. 6. Experimental and modeled Cu-LID in high-res Cz and low-res Cz samples with $C_{\text{Cu}_i}^{\text{init}}$ of $0.76 \times 10^{14} \text{ cm}^{-3}$ and $1 \times 10^{14} \text{ cm}^{-3}$, respectively, under 1 sun at RT. High-res Cz samples were simulated separately with two values of γ , $0.615 \times 10^{-4} \text{ J cm}^{-2}$ and $0.720 \times 10^{-4} \text{ J cm}^{-2}$. Also shown is the BO defect-limited lifetime for the low-res Cz sample under 1 sun at RT. Experimental data are from Refs. 5 and 32, and the lifetimes are reported at an excess carrier concentration $\Delta n_e = 0.1 \times N_a$. The inset is a zoom from 1000 min to the end of the time scale.

from $3.8 \times 10^{15} \text{ cm}^{-3}$ (low-res Cz) to $1.5 \times 10^{16} \text{ cm}^{-3}$ (low-res FZ) caused an approximately two orders of magnitude decrease in the degradation rate. In the high-res Cz case in Fig. 6, the decrease in N_a compared to low-res Cz is even greater (six-fold), and based on the modeling result (with the same energetic and kinetic terms $\Delta G_S = 0$, $\gamma = 0.615 \times 10^{-4} \text{ J cm}^{-2}$, and $\Delta G_{\text{act}} = 0$ as above), shown as a red dashed-dotted line, an increase of the degradation rate of almost two orders of magnitude is expected. Instead, the high-res Cz sample shows slower degradation than the low-res Cz sample, and the experimental final lifetime of $17 \mu\text{s}$ is notably higher than $7.6 \mu\text{s}$ of the low-res Cz wafer, or $5.4 \mu\text{s}$ obtained for high-res Cz with modeling.

To improve the agreement between simulated τ_{eff} and experiments, the value of the surface energy term, γ , was increased from $0.615 \times 10^{-4} \text{ J cm}^{-2}$ to $0.720 \times 10^{-4} \text{ J cm}^{-2}$ as shown by the dashed-double dotted line in Fig. 6. With this higher value of γ , not only does the degradation rate decrease to coincide with the experimental high-res Cz data but also the final lifetime increases from $5.4 \mu\text{s}$ to $45 \mu\text{s}$, qualitatively reproducing the experimentally observed reduction in the degradation rate and increase in the final lifetime in comparison to low-res Cz. A physical interpretation for this adjustment of γ is provided in Sec. IV.

F. Injection dependence

While Secs. III A–III E focused on minority carrier lifetime at a single excess carrier concentration ($\Delta n_e = 0.1 \times N_a$) as a function of illumination time, here simulation results are compared to experimental final degraded lifetimes measured over a broad range of excess carrier concentrations. The samples included in this analysis are the low-res Cz wafer in Fig. 1 (degraded at RT), the low-res Cz wafer in Fig. 4 (degraded under ALID conditions), and the low-res FZ wafer in Fig. 5. Since the measured lifetime is affected by many recombination processes (e.g., radiative, Auger, surface, and BO defect recombination), the Cu-related lifetime, τ_{Cu} , has been separated from the other recombination channels through the relation

$$\tau_{\text{Cu}}(\Delta n_e) = \left(\frac{1}{\tau_{\text{deg}}} - \frac{1}{\tau_{\text{init}}} - \frac{1}{\tau_{\text{BO}}} \right)^{-1}, \quad (2)$$

where τ_{deg} and τ_{init} are the injection-dependent lifetimes measured before and after degradation, and τ_{BO} is the BO-related lifetime in the final degraded state, calculated with the BO parametrization used in this work. Here, we note that Fe is expected to be approximately in the same state (mostly existing as Fe–B, see Sec. III A) both before and after degradation, and its (small) effect is therefore accounted for by Eq. (2). Figure 7 reports τ_{Cu} and simulated injection-dependent lifetime curves that were calculated using the final precipitate size and density distributions resulting from the simulation of the LID curves (discussed further in Sec. IV D) and the parametrization of Ref. 4. Good agreement between simulated and experimental lifetime curves can be observed in all cases. Importantly, the overall shape of the modeled curves is in substantial agreement with the experimental data.

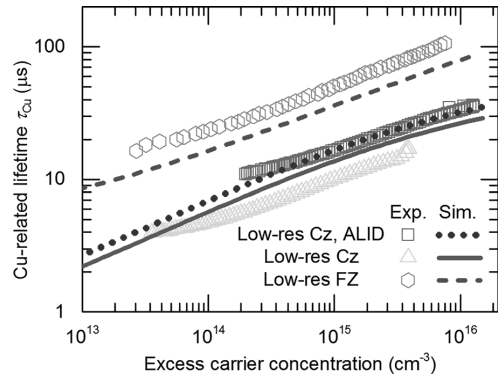


FIG. 7. Experimental and simulated injection-dependent minority carrier lifetimes in the final degraded state in the case of low-res Cz and FZ samples of Figs. 1, 4, and 5. The experimental lifetime data were corrected for other mechanisms unrelated to Cu-LID, including radiative, Auger, surface, and BO defect recombination.

IV. ANALYSIS AND DISCUSSION

In Secs. IV A–IV E, the internal mechanisms of the model are investigated further. Considering the good qualitative agreement that was found between simulations and experiments in Sec. III, we believe that this analysis can be extended to real-life samples and can help improve the general understanding of the physical phenomena that take place during Cu-LID. To summarize, the correlation between the energetic barrier of nucleation and precipitate density is illustrated in Sec. IV A. In addition, the connection between the degradation rate of Cu-LID and nucleation rate (NR) is examined in Sec. IV B, followed by a discussion on the kinetics of Cu-LID in Sec. IV C. Furthermore, a clear link is drawn between the final lifetime and precipitate size in Sec. IV D. Finally, in Sec. IV E, the physical significance of the above fitted energetic parameters, γ and ΔG_S , is discussed together with considerations regarding the nucleation mode of Cu-LID.

A. Precipitate density

Precipitate density is considerably dependent on the energetics of the nucleation process. While growth of existing nuclei larger than critical size occurs spontaneously, the nucleation stage demands external energy.³³ In case the interstitial Cu ions do not have sufficient energy for nucleation to continue, the precipitation process continues only with the growth of existing nuclei, and the precipitate density remains constant. Energistics of nucleation can be examined by solving the effective nucleation barrier (NB) height, corresponding to the total energy required to grow a precipitate from an interstitial atom to the critical size (including electrostatic effects), based on Eq. (1) in Paper I using the above fitted values of γ and ΔG_S .

In Fig. 8, the effective NB height at the start of illumination, when the interstitial Cu concentration is still at its initial value, is correlated with final precipitate density obtained from the simulations in the different cases described in Figs. 2, 4, 5, and 6. The initial NB height reduces in the order of

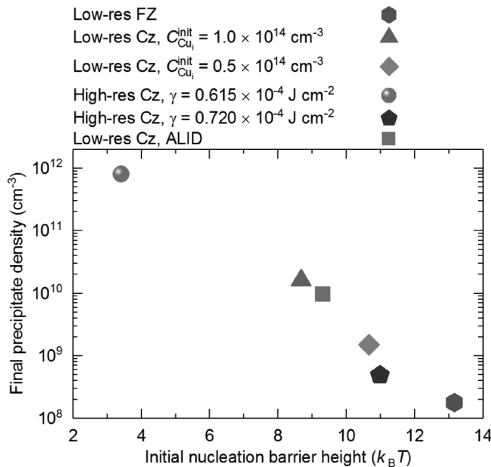


FIG. 8. Final precipitate density after illumination obtained from the simulations as a function of the initial NB height.

decreasing doping due to declining solid solubility, which can be associated with a clear trend of increasing precipitate density. On the other hand, halving the interstitial Cu concentration from 1 × 10¹⁴ cm⁻³ to 0.5 × 10¹⁴ cm⁻³ (low-res Cz) increases the NB height from 8.7 × k_BT to 11 × k_BT, which also illustrates how the energetics changes as interstitial Cu ions are consumed as precipitation progresses. Moreover, the rise in NB height when γ is increased from 0.615 × 10⁻⁴ J cm⁻² to 0.720 × 10⁻⁴ J cm⁻² in the high-res Cz case not only reduces the degradation rate of Cu-LID in Fig. 6 but also considerably decreases the precipitate density (increasing final τ_{eff}).

B. Nucleation rate

The degradation rate of Cu-LID can be closely correlated with the initial rate of nucleation. To illustrate this dependence, Fig. 9 shows the nucleation rate (NR) for different experimental cases in Figs. 2, 4, and 5, describing how many stable nuclei (above critical size) are formed under illumination per unit volume and time.

In the case of the low-res Cz sample with C_{Cu}^{init} = 1 × 10¹⁴ cm⁻³, the initial NR starts from a stable value of ~10⁷ cm⁻³ s⁻¹. After ~20 min of illumination, there is a steep descent in NR, which can be associated with a decrease in the level of supersaturation due to consumption of interstitial Cu (or increased fraction of precipitated Cu shown on the right axis of Fig. 9). The effect of decreased interstitial Cu concentration is further illustrated by the low-res Cz sample case with C_{Cu}^{init} = 0.5 × 10¹⁴ cm⁻³, in which the initial NR is two orders of magnitude lower than with C_{Cu}^{init} = 1 × 10¹⁴ cm⁻³, only ~10⁵ cm⁻³ s⁻¹, which explains the lower degradation rate of this sample in Fig. 2.

Also shown in Fig. 9 is the nucleation rate in low-res FZ, whose low value explains the slow degradation in Fig. 5. The difference between the NRs of low-res Cz and low-res FZ derives mostly from the greater NB height in the latter (see Fig. 8), and in a smaller part from the ~3.5 times lower

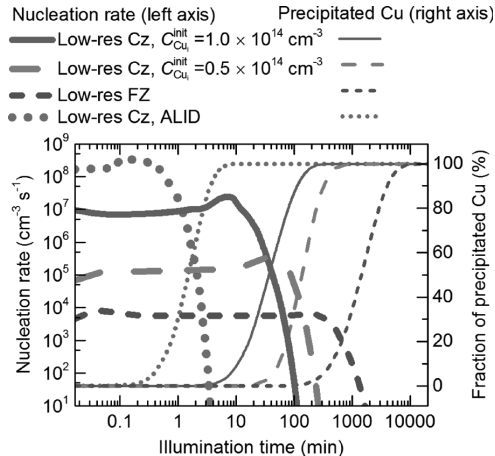


FIG. 9. Simulated nucleation rate (left axis) and precipitated Cu fraction (right axis) as a function of illumination time in the different cases described by Figs. 2, 4, and 5.

diffusivity in the low-res FZ material, which is due to the higher N_a and Cu-B pairing. In the case of ALID, on the other hand, the initial NB height in Fig. 8 is 9.3 × k_BT, that is, only slightly higher than 8.7 × k_BT of the similar low-res Cz wafer at RT. This means that energetics cannot explain the greatly increased nucleation rate of ALID (blue dotted curve in Fig. 9), but kinetics, that is, precipitate surface effects limiting the growth process, must be considered.

C. Kinetics of Cu-LID

Kinetics is affected first by the interface reaction rate [see Eq. (14) in Paper I] and second by depletion of interstitial Cu at the precipitate surface in comparison to the general bulk concentration in the sample. Considering that the best agreement between experiments and simulations was obtained by assuming a negligible activation barrier of the interface reaction ($\Delta G_{\text{act}} = 0$), it follows that factors influencing the kinetics are mainly the same as those affecting the depletion of interstitial Cu at the precipitate surface, including the built-in voltage (drift) and diffusion. Comparing the kinetics of ALID and RT-LID, diffusivity of interstitial Cu in the low-res Cz sample is 1.5 × 10⁻⁶ cm² s⁻¹ at 120 °C, whereas it is only 4.1 × 10⁻⁸ cm² s⁻¹ at RT. On the other hand, built-in voltages according to the Schottky model are similar at these two temperatures under illumination. Consequently, the faster NR of ALID compared to RT-LID is directly attributable to the increased diffusivity. This result confirms the hypothesis of Ref. 6, where the increased degradation rate of Cu-related ALID was tentatively attributed to the high diffusivity at 120 °C. In addition, correlation between the temperature-dependent diffusivity and NR on one hand and precipitate growth rate on the other hand explain why Cu-LID defect activation was observed to be diffusion-limited in Ref. 5 (where the activation energy is extracted from the temperature dependence of the degradation rate and was therefore observed to reflect the diffusivity of interstitial Cu).

Similar to ALID, the acceleration of the degradation rate with increasing illumination intensity (see Fig. 3) follows almost entirely out of kinetic considerations, with only a minor energetic contribution from the effect of illumination on the effective solubility [through E_{fp} , see Eq. (28) in Paper I]. The fact that the illumination intensity did not significantly affect the final lifetime in Fig. 3 supports this interpretation, since a change in energetics is expected to alter the precipitate size and density, and consequently the final τ_{eff} . Regarding the difference between experiments and simulations at different intensities, there is almost two orders of magnitude change in the kinetic growth factor, λ_{kin} (see Fig. 2 in Paper I), when intensity is decreased from 1.8 sun to 0.003 sun. However, this change in λ_{kin} does not result in a sufficient decrease in the simulated degradation rate to fully comply with experiments. Nevertheless, the simulation results shown in Fig. 3 can be seen as qualitative evidence that a change in illumination conditions and consequent effects on precipitate charging can theoretically considerably influence the timescale of precipitation and the associated degradation of τ_{eff} .

D. Precipitate size

As mentioned above, the final density and size of precipitates are expected to have a direct impact on the final degraded τ_{eff} . On the other hand, the precipitate densities of Fig. 8 are directly linked to the final precipitate size through the total density of in-diffused Cu atoms in the sample. Figure 10(a) shows a comparison of experimental and simulated final τ_{eff} in the four different experimental cases described in Figs. 2, 4, and 5 (the same samples as in Fig. 9). Consequently, the trend in the final τ_{eff} is explained by the simulated final size distribution of the precipitates, shown in Fig. 10(b). For the low-res Cz sample with $C_{\text{Cu}}^{\text{init}} = 1 \times 10^{14} \text{ cm}^{-3}$, corresponding to the lowest simulated final degraded τ_{eff} of $9.3 \mu\text{s}$, the model predicts a dominant precipitate radius of $2\text{--}3 \text{ nm}$. On the other hand, with the lower $C_{\text{Cu}}^{\text{init}} = 0.5 \times 10^{14} \text{ cm}^{-3}$, associated with a higher simulated final degraded τ_{eff} of $29 \mu\text{s}$, the dominant radius is higher, $4\text{--}5 \text{ nm}$. Since the precipitate size decreases with increasing $C_{\text{Cu}}^{\text{init}}$, the recombination activity of Cu-LID increases superlinearly with respect to the impurity Cu concentration. In the ALID case, both the simulated final degraded τ_{eff} and the precipitate radius reside in-between the two first mentioned, at $10 \mu\text{s}$ and $3\text{--}4 \text{ nm}$, respectively. Finally, the high final simulated lifetime of $40 \mu\text{s}$ in the case of the low-res FZ sample can be explained by large precipitates with a dominant radius of $14\text{--}16 \text{ nm}$.

Comparing the experimental and simulated τ_{eff} of Fig. 10(a) in general, the qualitative trend between simulation and experiment is in agreement, which is important evidence for the precipitation theory of Cu-LID. The agreement between experimental and simulated injection-dependent final degraded lifetimes in Fig. 7 strengthens this conclusion and the link between the final lifetime and the precipitate size. The deviations between the experimental and modeled final lifetimes are so small that they may, in principle, derive for example from uncertainties in the

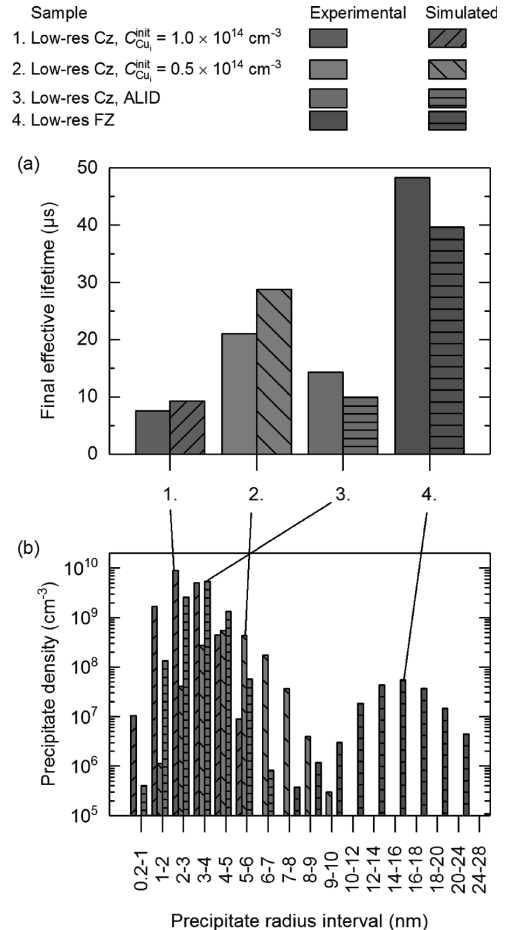


FIG. 10. (a) Experimental and modeled final effective lifetimes, τ_{eff} , of different samples after illumination. Lifetimes are reported at an excess carrier concentration $\Delta n_e = 0.1 \times N_a$. (b) Simulated precipitate radius and density distributions after illumination.

initial Cu concentration, or ambiguity related to the shape of the precipitates. Nevertheless, the assumption of spherical precipitates seems to reproduce the final lifetimes accurately in all four cases with the estimated total Cu concentration.

E. Energetic parameters and nucleation mode

As described in Sec. III, the best agreement between simulations and experiments was obtained with energy terms $\Delta G_S = 0$, and $\gamma = 0.615 \times 10^{-4} \text{ J cm}^{-2}$. The fitted value of γ is in the same order of magnitude as data of Li,³⁴ who determined a dependence between γ and Φ_{Bn} . The value obtained interpolating Li's data is $\gamma = 0.76 \times 10^{-4} \text{ J cm}^{-2}$ for $\Phi_{\text{Bn}} = 0.59 \text{ eV}$, which is in a good agreement considering, for example, uncertainty concerning the exact precipitate shape. Regarding the free energy change per precipitate volume due to strain, ΔG_S , it was found that deviating the value of this quantity from zero always deteriorates the fit. This fact stands in contradiction with the premise of homogeneously nucleating

spherical precipitates, under which the elastic lattice strain would be expected to play a significant role. Possible reasons include either a considerable deviation of the actual precipitate shape from spheres or a sufficient amount of heterogeneous nucleation sites in the studied materials, such as vacancies, dislocations, and/or oxygen precipitate/Si phase boundaries, which minimize the effects of lattice strain. However, with the given total Cu concentration, assuming a strain-minimizing shape such as very thin plates^{35–38} would result in a great increase in precipitate radius and/or density. This would cause a substantial increase in the available recombination surface, decreasing the precipitate-limited lifetime up to several orders of magnitude.^{4,39} The fact that the spherical shape was shown above to reproduce the experimental results well implies that the shape is closer to spherical than plate-like.

Degradation rate and final lifetime of Cu-LID have been earlier shown to be correlated with density of intentionally grown oxygen precipitates in the bulk.⁷ In addition, the spherical precipitate shape has earlier been associated only with heterogeneous nucleation on extended defects that reduce the energetic barrier of nucleation.^{35,36} Therefore, the unexpectedly slow degradation of the high-res Cz sample in Fig. 6, and the increase in γ that was necessary to reproduce experiments, can be interpreted to follow from a reduced density of low-energy nucleation sites, such as strained oxygen precipitates,⁴⁰ in comparison to low-res Cz. This difference may follow for example from a dissimilar thermal history and/or from the lower O_i concentration (see Table I).^{41–43} On the other hand, in low-res FZ reported in Fig. 5, vacancies in the wafer center⁴⁴ provide another type of nucleation sites. The same γ in the case of both low-res Cz and low-res FZ implies that the density of heterogeneous nucleation sites does not limit the precipitation process in these materials even though nucleation sites were not intentionally created. Nevertheless, due to simplifications of the model (i.e., spherical precipitate shape and homogeneous nucleation), the energy terms should be considered as effective values. Since final τ_{eff} increased with higher γ , the above conclusion also implies that a part of the negative effects of Cu-LID can be avoided by using Si with a very low density of extended defects.

It should be noted that the assumption that the energy terms remain constant throughout the whole precipitation process might be one source of error in this study. For example, filling of space available on suitable precipitation sites in the Si lattice during precipitate growth could gradually increase the average energy required to include Cu atoms into the precipitates. This effect would lead to a progressive increase in effective solubility [see Eq. (28) in Paper I] during precipitation, which would consequently slow down Cu-LID at longer illumination times. This could be one explanation why the negative slope of Cu-LID curves was shallower in the case of experimental data than simulations (see Fig. 2), and why asymptotic degradation was observed in the experiments at long illumination times.

V. CONCLUSIONS

The comprehensive mathematical model that was proposed for Cu-related light-induced degradation (Cu-LID) in

Paper I of the article was compared with experiments in this second part. The fact that the model works directly at the minority carrier lifetime level enabled a straightforward comparison to experimental LID data, against which considerable agreement was found. Both the Cu concentration and doping dependence of Cu-LID can be explained based on the level of supersaturation influencing the nucleation rate and precipitate density. On the other hand, the temperature dependence of Cu-LID follows from the effect of temperature on the diffusivity of interstitial Cu. Although the intensity dependence was reproduced only qualitatively, the simulated degradation rate was very low in the dark due to the dependence of electrostatic repulsion between Cu₃Si precipitates and interstitial Cu on excess carrier concentration. The unexpectedly low nucleation rate in the high resistivity material may be an indication that heterogeneous nucleation sites influence the precipitation process even in Cz and FZ silicon in which these sites have not been intentionally introduced. The simulations revealed a correlation between experimental final degraded lifetime and precipitate size which was found to vary between 2 and 16 nm. This correlation provides a natural theoretical explanation for total recombination activity of Cu-LID increasing superlinearly with increasing interstitial Cu concentration and decreasing with increasing doping concentration and reducing low-energy nucleation site density.

ACKNOWLEDGMENTS

The work has been funded through the European Research Council under the European Union's FP7 Programme ERC Grant Agreement No. 307315. A.I. acknowledges the financial support of Aalto ELEC doctoral school and Alfred Kordelin Foundation. The authors also acknowledge Professor J. Sinkkonen, whose notes are the base for the derivation in Sec. III E of Paper I, and Dr. Chiara Modanese for valuable comments during manuscript writing.

- ¹P. S. Plekhanov and T. Y. Tan, *Appl. Phys. Lett.* **76**, 3777 (2000).
- ²M. D. Negoita and T. Y. Tan, *J. Appl. Phys.* **94**, 5064 (2003).
- ³W. Kwapił, J. Schön, F. Schindler, W. Warta, and M. C. Schubert, *IEEE J. Photovoltaics* **4**, 791 (2014).
- ⁴W. Kwapił, J. Schön, W. Warta, and M. C. Schubert, *IEEE J. Photovoltaics* **5**, 1285 (2015).
- ⁵J. Lindroos and H. Savin, *J. Appl. Phys.* **116**, 234901 (2014).
- ⁶A. Inglesle, J. Lindroos, and H. Savin, *Appl. Phys. Lett.* **107**, 052101 (2015).
- ⁷H. Väinölä, E. Saarnilehto, M. Yli-Koski, A. Haarahiltunen, J. Sinkkonen, G. Berenyi, and T. Pavelka, *Appl. Phys. Lett.* **87**, 032109 (2005).
- ⁸H. Savin, M. Yli-Koski, and A. Haarahiltunen, *Appl. Phys. Lett.* **95**, 152111 (2009).
- ⁹J. Lindroos, Y. Boufrad, M. Yli-Koski, and H. Savin, *J. Appl. Phys.* **115**, 154902 (2014).
- ¹⁰J. Lindroos, M. Yli-Koski, A. Haarahiltunen, M. C. Schubert, and H. Savin, *Phys. Status Solidi RRL* **7**, 262 (2013).
- ¹¹T. Heiser, S. McHugo, H. Hieslmair, and E. R. Weber, *Appl. Phys. Lett.* **70**, 3576 (1997).
- ¹²A. Richter, S. W. Glunz, F. Werner, J. Schmidt, and A. Cuevas, *Phys. Rev. B* **86**, 165202 (2012).
- ¹³J. Schmidt, A. G. Aberle, and R. Hezel, in *Conference Record of the Twenty Sixth IEEE Photovoltaic Specialists Conference - 1997*, Anaheim, California, USA, 29 September–3 October 1997 (Institute of Electrical and Electronics Engineers, New York, 1997), pp. 13–18.
- ¹⁴V. V. Voronkov, R. Falster, K. Bothe, B. Lim, and J. Schmidt, *J. Appl. Phys.* **110**, 063515 (2011).

- ¹⁵T. Niewelt, J. Schön, J. Broisch, W. Warta, and M. Schubert, *Phys. Status Solidi RRL* **9**, 692 (2015).
- ¹⁶J. D. Murphy, K. Bothe, R. Krain, V. V. Voronkov, and R. J. Falster, *J. Appl. Phys.* **111**, 113709 (2012).
- ¹⁷K. Bothe, R. Sinton, and J. Schmidt, *Prog. Photovoltaics: Res. Appl.* **13**, 287 (2005).
- ¹⁸J. Schön, T. Niewelt, J. Broisch, W. Warta, and M. C. Schubert, *J. Appl. Phys.* **118**, 245702 (2015).
- ¹⁹D. H. Macdonald, L. J. Geerligs, and A. Azzizi, *J. Appl. Phys.* **95**, 1021 (2004).
- ²⁰S. Rein, *Lifetime Spectroscopy—A Method of Defect Characterization in Silicon for Photovoltaic Applications* (Springer-Verlag, Berlin, Heidelberg, 2005), pp. 375–377.
- ²¹F. J. Bottari, W. Montanez-Ortiz, D. C. Wong, P. J. Richter, F. C. Dimock, M. Bowers, and T. Bao, in *2010 35th IEEE Photovoltaic Specialists Conference*, Honolulu, Hawaii, USA, 20 June–25 June (Institute of Electrical and Electronics Engineers, New York, 2010), pp. 001315–001317.
- ²²M. B. Shabani, T. Yoshimi, and H. Abe, *J. Electrochem. Soc.* **143**, 2025 (1996).
- ²³H. Väinölä, M. Yli-Koski, A. Haarahiltunen, and J. Sinkkonen, *J. Electrochem. Soc.* **150**, G790 (2003).
- ²⁴C. Möller, T. Bartel, F. Gibaja, and K. Lauer, *J. Appl. Phys.* **116**, 024503 (2014).
- ²⁵C. Flink, H. Feick, S. A. McHugo, W. Seifert, H. Hieslmair, T. Heiser, A. A. Istratov, and E. R. Weber, *Phys. Rev. Lett.* **85**, 4900 (2000).
- ²⁶A. Belayachi, T. Heiser, J. P. Schunck, and A. Kempf, *Appl. Phys. A* **80**, 201 (2005).
- ²⁷M. O. Abolafotoh, A. Cros, B. G. Svensson, and K. N. Tu, *Phys. Rev. B* **41**, 9819 (1990).
- ²⁸P. Hamer, B. Hallam, M. Abbott, and S. Wenham, *Phys. Status Solidi RRL* **9**, 297 (2015).
- ²⁹N. E. Grant, F. E. Rougier, D. MacDonald, J. Bullock, and Y. Wan, *J. Appl. Phys.* **117**, 055711 (2015).
- ³⁰D. Sperber, A. Heilemann, A. Herguth, and G. Hahn, *IEEE J. Photovoltaics* **7**, 463 (2017).
- ³¹A. Inglese, J. Lindroos, H. Vahlman, and H. Savin, *J. Appl. Phys.* **120**, 125703 (2016).
- ³²J. Lindroos, Ph.D. thesis, Aalto University, Espoo (2015).
- ³³D. Kashchiev, *Nucleation - Basic Theory with Applications* (Butterworth-Heinemann, Oxford, 2000) pp. 17–44.
- ³⁴J. G. Li, *Mater. Chem. Phys.* **47**, 126 (1997).
- ³⁵M. Seibt, M. Griess, A. A. Istratov, H. Hedemann, A. Sattler, and W. Schröter, *Phys. Status Solidi A* **166**, 171 (1998).
- ³⁶M. Seibt, H. Hedemann, A. A. Istratov, F. Riedel, A. Sattler, and W. Schröter, *Phys. Status Solidi A* **171**, 301 (1999).
- ³⁷A. A. Istratov, H. Hedemann, M. Seibt, O. F. Vyvenko, W. Schröter, T. Heiser, C. Flink, H. Hieslmair, and E. R. Weber, *J. Electrochem. Soc.* **145**, 3889 (1998).
- ³⁸H. W. Guo and S. T. Dunham, *Appl. Phys. Lett.* **89**, 182106 (2006).
- ³⁹C. Donolato, *Semicond. Sci. Technol.* **8**, 45 (1993).
- ⁴⁰R. Falster, V. V. Voronkov, V. Y. Resnik, and M. G. Milvidskii, *High Purity Silicon VIII: Proceedings of the International Symposium*, Honolulu, Hawaii, USA, 3–8 October 2004, edited by C. L. Claeys, M. Watanabe, L. Falster, and P. Stallhofer (The Electrochemical Society, Pennington, NJ, USA, 2004), pp. 188–201.
- ⁴¹A. Borghesi, B. Pivac, A. Sassella, and A. Stella, *J. Appl. Phys.* **77**, 4169 (1995).
- ⁴²H. Takeno, T. Otogawa, and Y. Kitagawara, *J. Electrochem. Soc.* **144**, 4340 (1997).
- ⁴³J. D. Murphy, M. Al-Amin, K. Bothe, M. Olmo, V. V. Voronkov, and R. J. Falster, *J. Appl. Phys.* **118**, 215706 (2015).
- ⁴⁴T. Abe and T. Takahashi, *J. Cryst. Growth* **334**, 16 (2011).
- ⁴⁵H. Vahlman, A. Haarahiltunen, W. Kwapił, J. Schön, A. Inglese, and H. Savin, “Modeling of light-induced degradation due to Cu precipitation in p-type silicon. I. General theory of precipitation under carrier injection,” *J. Appl. Phys.* **121**, 195703 (2017).

Publication V

A.Inglese, J.Lindroos, H.Savin. Accelerated light-induced degradation for detecting copper contamination in *p*-type silicon. *Applied Physics Letters*, 107, 052101, 2015.

© 2015 American Institute of Physics Publishing LLC.

Reprinted with permission.

Accelerated light-induced degradation for detecting copper contamination in p-type silicon

Alessandro Inglese,^{1,a)} Jeanette Lindroos,^{1,2} and Hele Savin¹

¹Department of Micro- and Nanosciences, Aalto University, Tietotie 3, 02150 Espoo, Finland

²Department of Engineering and Physics, Karlstad University, Universitetsg. 2, 65188 Karlstad, Sweden

(Received 29 March 2015; accepted 23 July 2015; published online 3 August 2015)

Copper is a harmful metal impurity that significantly impacts the performance of silicon-based devices if present in active regions. In this contribution, we propose a fast method consisting of simultaneous illumination and annealing for the detection of copper contamination in p-type silicon. Our results show that, within minutes, such method is capable of producing a significant reduction of the minority carrier lifetime. A spatial distribution map of copper contamination can then be obtained through the lifetime values measured before and after degradation. In order to separate the effect of the light-activated copper defects from the other metastable complexes in low resistivity Cz-silicon, we carried out a dark anneal at 200 °C, which is known to fully recover the boron-oxygen defect. Similar to the boron-oxygen behavior, we show that the dark anneal also recovers the copper defects. However, the recovery is only partial and it can be used to identify the possible presence of copper contamination. © 2015 AIP Publishing LLC.

[<http://dx.doi.org/10.1063/1.4927838>]

Copper contamination is a serious issue in both solar-cell¹ and semiconductor technologies² because of its detrimental effect on minority carrier lifetime and diffusion length. Due to the high copper diffusivity and solubility,³ the avoidance of copper contamination is rather challenging during the growth of silicon ingots and the subsequent solar-cell fabrication steps. Furthermore, additional copper contamination may result from recently introduced copper contacts in both integrated circuits and solar cells, despite the use of specific copper diffusion barriers. The presence of copper contamination in silicon can be detected by quantitative methods, such as transient ion drift (TID)⁴ and total reflection x-ray fluorescence (TXRF).⁵ However, the former method requires immediate measurements after contact formation, while the latter is limited to measuring only near-surface concentrations. Furthermore, both TID and TXRF methods are destructive and time-consuming methods.⁶

Recently, copper has been observed to reduce the minority carrier lifetime during prolonged annealing in the dark or illumination at room temperature. The activation of recombination-active defects during light soaking is commonly referred to as copper-related light-induced degradation (Cu-LID). The Cu-LID has been confirmed to originate from bulk recombination,⁵ which is proposed to be caused by copper precipitation⁷ or substitutional copper release through copper complex dissociation during illumination.^{8,9} The formed defects have been found to be stable at 200 °C in wafers with initial interstitial copper concentration of 10^{14} cm^{-3} .¹⁰

In addition to copper defects, the involvement of boron and oxygen in the formation of a metastable recombination-active defect (BO-LID) has been extensively reported as the major cause of degradation in low-resistivity boron-doped Czochralski (Cz) silicon.¹¹ BO-LID is typically observed as a

two-exponential lifetime decay within 24 h of illumination, which is fully recoverable at 200 °C.¹² The lifetime decrease and the normalized defect density can easily be measured for both BO-LID and Cu-LID by contactless and non-destructive characterization methods, such as quasi-steady-state photoconductance (QSPPC),¹³ microwave photoconductive decay (μ -PCD),¹⁴ and surface photovoltage (SPV).¹⁵ Since the normalized Cu-LID defect has been found proportional to the initial interstitial copper concentration,⁷ lifetime measurements before and after degradation provide an estimate for the interstitial copper concentration. The main drawback of this copper-detection technique is the long illumination time needed for a saturation of the observed lifetime decay.

In order to decrease the BO-LID detection time, a new method called accelerated light-induced degradation (ALID) has been recently developed.¹⁶ The method relies on illumination at elevated temperatures (120 °C), achieving full degradation within only 10 min.¹⁷ In this letter, our goal is to deepen the understanding of the formation kinetics of light-activated copper defects by analyzing the impact of the ALID method on Cu-LID. Second, we also want to determine whether this ALID method can be employed for rapidly detecting the presence of copper contamination in silicon.

The experiments were performed on ⟨100⟩ oriented, 4-in., boron-doped, electronic-grade Cz-silicon with resistivity of 3.4–3.9 Ω cm, thickness of $\sim 380 \mu\text{m}$, and an oxygen concentration higher than 14.5 ppm. After standard RCA cleanings, the wafers were passivated through the growth of a 15 nm thick thermal oxide layer, formed during 40 min of dry oxidation at 900 °C, followed by annealing in nitrogen at the same temperature for 20 min. A contamination solution containing 1 ppm of copper sulfate solution was then spinneed onto the front surface of each wafer, which quickly turned into interstitial copper bulk contamination during annealing in nitrogen atmosphere at 800 °C. Next, an external corona

^{a)}E-mail: alessandro.inglese@aalto.fi

charge ($+0.3 \mu\text{C}/\text{cm}^2$) was deposited onto both sides of the wafer, in order to prevent copper out-diffusion⁶ and reduce the surface minority carrier recombination through the creation of an inversion layer near the surface.

Before illumination, the samples were annealed in the dark at 200°C for 2 min to deactivate any metastable active complex formed during sample preparation. Since annealing reduces the surface corona charge, $+0.06 \mu\text{C}/\text{cm}^2$ was added onto each side of the wafer.¹⁰ The samples were then divided into two separate batches that underwent different degradation treatments. The first batch went through illumination at room temperature for 24 h under a 0.5 Sun Xenon lamp, i.e., a RT-LID treatment. The second batch of wafers was subjected to the ALID procedure, consisting of illumination with the same Xenon light source and simultaneous heating at the temperature of 120°C .¹⁷ During the ALID and the RT-LID treatments, the effective minority carrier lifetime was monitored with QSSPC measurements at the injection level of $\Delta n = 0.1 \cdot N_{dop}$, ensuring that the measured lifetime is dominated by Schockley-Read-Hall recombination.

Figure 1 presents the minority carrier lifetime measured in identical Cu-contaminated wafers during ALID and RT-LID. The ALID method clearly accelerates the formation kinetics of light-activated copper defects compared with RT-LID, which is in analogy with previous ALID data reported for the B-O complex. This result hence raises the question whether the possible effect of copper has been ignored in previous publications on ALID.¹⁶

Figure 1 also shows that during ALID a large portion of the lifetime decay takes place during the first few minutes, suggesting that the degradation kinetics are initially very fast and progressively slow down until a saturation is reached. By comparing the lifetime values measured during ALID and RT-LID after identical degradation time steps, it becomes evident that ALID results in almost complete lifetime saturation within 1 h, whereas RT-LID requires almost a whole day to reach similar degradation. Note that the Cu-related degradation rate depends on the annealing temperature,¹⁰ light intensity,^{9,14} and impurity concentration,⁷ enabling probably even faster lifetime saturation at higher temperatures, illumination intensities, or copper concentrations.

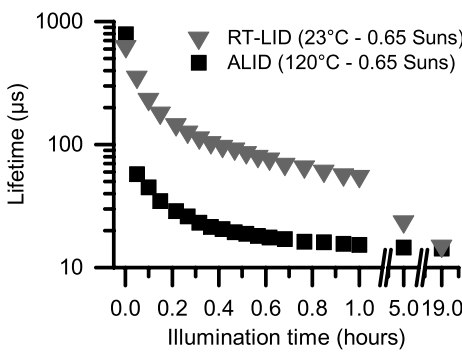


FIG. 1. Minority carrier lifetime as a function of the illumination time measured in identical Cu-contaminated Cz-wafers during ALID and conventional room-temperature degradation (RT-LID). The lifetime was measured with QSSPC at the injection level of $3 \times 10^{14} \text{ cm}^{-3}$.

The strong impact of 120°C annealing on the degradation kinetics can be explained by the higher copper diffusivity at increasing temperatures.^{18,19} Since copper is known to form unstable CuB complexes that constantly pair and dissociate even at room temperature, the diffusivity of interstitial copper is further increased by the complete dissociation of Cu-B pairs at 120°C in $3.4\text{--}3.9 \Omega \text{ cm}$ silicon.²⁰ This result is in accordance with recent studies proving that Cu-LID is a bulk phenomenon⁵ limited by copper diffusion.¹⁰

In order to further study the applicability of ALID for measuring copper in silicon, we intentionally contaminated only a small portion of the wafer by depositing a 20 ppb copper sulfate solution droplet ($\approx 7 \text{ cm}^2$) on the wafer front surface. This was followed by the same in-diffusion anneal and ALID/RT-LID treatments as previously described. The minority carrier diffusion length was then analyzed in both clean and intentionally contaminated areas with the SPV technique, which allows a detailed minority carrier diffusion length mapping at low injection level (excess carrier concentration of $\sim 10^{12} \text{ cm}^{-3}$). Some of the wafers were also measured by μ -PCD that allows the mapping of minority carrier lifetime at higher injection level ($\sim 10^{15} \text{ cm}^{-3}$).

After illumination, the copper spot becomes visible in both SPV and μ -PCD maps. Hence, light-activated copper defects are highly recombination active at both high and low injection level. This is a different behavior compared to iron impurities. Indeed, the recombination activity of interstitial iron (Fe_i) is known to be strongly injection dependent, so that the lifetime measured after exposure to illumination (dissociation of Fe-B pairs) significantly increases at high injection and decreases at low excess carrier concentrations.^{21,22} There is thus a clear advantage of using high injection (μ -PCD) for copper detection, as the effect of copper contamination can be easily separated from iron impurities. Note that in this letter, we have dissociated Fe-B pairs before any degradation experiments through an initial dark anneal step, so that the possible presence of iron contamination cannot influence our low-injection measurements.

Figure 2(a) shows a μ -PCD lifetime map after 10 min of ALID. Stronger degradation is detected in the center of the

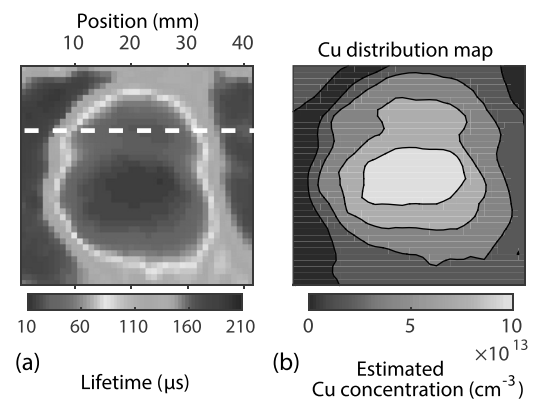


FIG. 2. (a) μ -PCD map after ALID (10 min), (b) spatial distribution map of copper calculated through Eq. (1). The dashed white line in (a) shows the line-scan position used for the data reported in Figure 3.

contaminated region, suggesting that copper tends to accumulate in the middle of the spot and its concentration progressively decreases towards the spot edges. This is in accordance with previous studies on Cu-LID, where the initial interstitial copper concentration N_{Cu} was found to be proportional to the degradation strength through the following empirical equation:⁶

$$N_{Cu} = C \left(\frac{1}{\tau_{deg}} - \frac{1}{\tau_{init}} \right)^{0.5}, \quad (1)$$

where C is a pre-factor fitted in Ref. 6 from μ -PCD lifetime results, τ_{init} is the lifetime value before degradation, and τ_{deg} represents the lifetime measured after ALID.

Figure 2(b) displays the copper concentration in each point of the copper spot shown in Fig. 2(a), obtained by inserting the μ -PCD lifetime maps before and after ALID into Eq. (1). Note that this calculation provides only an estimate of the copper concentration, as the numerical values given by Eq. (1) hold only under the conditions specified in Ref. 6. However, by combining ALID with a lifetime mapping technique, it is possible to achieve within only 10 min a qualitative copper distribution map, which allows to distinguish the different levels of contamination. Although complete degradation might not be reached within 10 min, Eq. (1) provides a reasonable estimation of Cu concentration, since, even in the most sensitive case, longer illumination time increases the estimated Cu concentration at most by a factor of 2. Therefore, it can be concluded that ALID provides a fast, non-contact, and non-destructive technique for measuring the interstitial copper concentration in silicon wafers.

Since both copper and B-O defects lead to lifetime degradation during light soaking, we want to separate the effect of the light-activated copper defects from the other metastable complexes in low-resistivity Cz-Si. Unlike Cu-related defects, it is well-known that B-O defects can be fully recovered by annealing at 200 °C in the dark, during which these complexes are thought to transform into a metastable inactive state.²³ After ALID, we thus annealed the samples at 200 °C for 3 min in the dark. To minimize the injection level dependence, the wafers were measured again at low-injection with SPV. Figure 3(a) shows the line-scan of the diffusion length map across the line-scan shown in Fig. 2(a) measured before degradation, after 10 min of ALID and a subsequent dark annealing at 200 °C. After annealing, Figure 3(a) shows a negligible lifetime increase in the middle of the copper spot, which is expected to be highly contaminated, whereas a larger but not complete recovery is detected near the edge of the copper spot. In order to determine whether this lifetime recovery is solely caused by the dissociation of B-O complexes, the experiment was repeated with an intentionally Cu-contaminated 250 μ m thick, low resistivity (1.5 Ω cm) p-type FZ-Si wafer, which is free of B-O recombination due to its low oxygen concentration.

Figure 3(b) shows the results obtained in the FZ wafer, i.e., diffusion length measured before and after degradation, and the subsequent dark annealing at 200 °C across a similar line-scan of the copper spot. Surprisingly, after annealing a diffusion length increase is detected over the whole line-scan

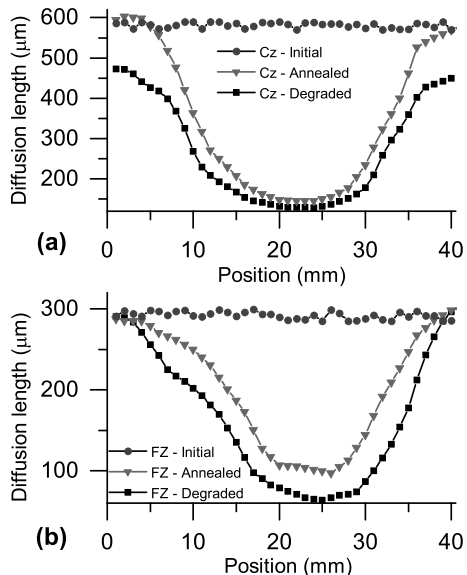


FIG. 3. Diffusion length measured with SPV before degradation (initial), after 10 min of ALID (degraded) and a subsequent 200 °C dark annealing (annealed) in spot Cu-contaminated Cz-Si (a) and FZ-Si (b).

of the copper spot. The uncontaminated reference area remains unaffected by the dark anneal, as the wafer is free of BO-LID. Any unintentional iron contamination would not affect the copper spot or the reference lifetime, since iron exists as Fe_i^+ both during degradation and annealing. Therefore, the measured lifetime recovery is clearly related to copper.

Possible copper-related reactions at 200 °C in FZ-Si include CuB dissociation, copper complex dissociation, substitutional copper (Cu_s) formation, and Cu-LID defect dissolution. CuB dissociation does not affect the lifetime, as no recombination activity has been related to CuB nor Cu_i^+ . Recombination-free four-copper-atom complexes start dissociating at 150 °C²⁴ releasing three Cu_i^+ ions and an unknown Cu_{DLA} center,²⁵ which might be Cu_s .^{26,27} Nevertheless, as substitutional copper is recombination active,² any Cu_s release would cause a lifetime decrease at 200 °C instead of the observed lifetime increase. Correspondingly, any other Cu_s formation at 200 °C would cause a further lifetime decrease, such as Cu_i^+ reaction with a vacancy,²⁸ a silicon self-interstitial,²⁹ or an oxygen-vacancy center.³⁰ Hence, the observed lifetime increase is concluded to be a result of Cu-LID defect dissolution. If Cu-LID were caused by recombination at substitutional copper, annealing at 200 °C might diffuse some copper from a substitutional lattice site into an interstitial, partly recovering the degraded lifetime. In case of copper precipitation being responsible for Cu-LID, the lifetime increment might be a result of precipitate dissolution, i.e., decrease of the precipitate size and/or density.

In the recent literature, only partial recovery has been observed in solar cells after LID but the reason has remained unclear.^{31–33} Our results suggest that the partial recovery could be a fingerprint of copper contamination and the dark

anneal could be used to determine whether the observed degradation is caused by copper.

In this letter, we have shown that the formation kinetics of recombination active copper defects can be significantly accelerated through simultaneous annealing and illumination. A qualitative copper distribution map has been calculated through the μ -PCD lifetime values measured before and after degradation. Such method can thus be used for the rapid detection of copper contamination.

While applied to low resistivity monocrystalline Cz- and FZ-material here, this method can, in principle, be extended to quasi-mono and multicrystalline silicon. In low-resistivity Cz-silicon, however, one needs to distinguish copper-related defects from metastable BO-complexes and, for this purpose, we investigated the effect of dark annealing after degradation. Interestingly, we observed a noticeable lifetime increase in lowly Cu-contaminated wafers that cannot be solely attributed to the dissociation of BO-complex, since a similar phenomenon was observed in oxygen-free FZ-silicon. This finding led us to conclude that the observed lifetime recovery results from the dissolution of Cu-LID defects. However, since the recovery seems not to be complete in the copper contaminated regions, the dark anneal can be used to determine whether the observed degradation is caused by copper contamination.

This research was performed at the Micronova Nanofabrication Centre of Aalto University. The experimental activity leading to these results has received funding from the European Research Council under the European Union's FP7 Programme ERC Grant Agreement No. 307315. A.I. acknowledges the support of the Aalto ELEC doctoral school, and J.L. acknowledges the support of Walter Ahlström Foundation.

- ¹J. R. Davis, A. Rohatgi, R. H. Hopkins, P. D. Blais, P. Rai-Choudhury, J. R. McCormick, and H. C. Mollenkopf, IEEE Trans. Electron Devices **27**, 677 (1980).
- ²K. Graff, *Metal Impurities in Silicon-Device Fabrication* (Springer, New York, 2000).
- ³A. A. Istratov and E. R. Weber, J. Electrochem. Soc. **149**(1), G21–G30 (2002).
- ⁴T. Heiser, S. McHugo, H. Hieslmair, and E. R. Weber, Appl. Phys. Lett. **70**, 3576 (1997).

- ⁵Y. Boulfrad, J. Lindroos, M. Wagner, F. Wolny, M. Yli-Koski, and H. Savin, Appl. Phys. Lett. **105**, 182108 (2014).
- ⁶H. Väinölä, E. Saarnilehto, M. Yli-Koski, A. Haarahiltunen, and J. Sinkkonen, Appl. Phys. Lett. **87**, 032109 (2005).
- ⁷H. Savin, M. Yli-Koski, and A. Haarahiltunen, Appl. Phys. Lett. **95**, 152111 (2009).
- ⁸W. B. Henley, D. A. Ramappa, and L. Jastrebski, Appl. Phys. Lett. **74**, 278 (1999).
- ⁹D. Ramappa, Appl. Phys. Lett. **76**, 3756 (2000).
- ¹⁰J. Lindroos and H. Savin, J. Appl. Phys. **116**, 234901 (2014).
- ¹¹S. W. Glunz, S. Rein, J. Y. Lee, and W. Warta, J. Appl. Phys. **90**, 2397 (2001).
- ¹²K. Bothe and J. Schmidt, J. Appl. Phys. **99**, 013701 (2006).
- ¹³D. Macdonald, A. Cuevas, S. Rein, P. Lichtner, and S. W. Glunz, in *Proceedings of 3rd World Conference on Photovoltaic Energy Conversion* (2003), Vol. 1, pp. 87–90.
- ¹⁴H. Väinölä, M. Yli-Koski, A. Haarahiltunen, and J. Sinkkonen, J. Electrochem. Soc. **150**(12), G790–G794 (2003).
- ¹⁵M. Yli-Koski, H. Savin, E. Saarnilehto, A. Haarahiltunen, J. Sinkkonen, G. Berenyi, and T. Pavelka, Solid State Phenom. **108–109**, 643 (2005).
- ¹⁶M. Wilson, P. Edelman, A. Savitchouk, J. D'Amico, A. Findlay, and J. Lagowski, J. Electron. Mater. **39**, 642 (2010).
- ¹⁷M. Tayyib, J. Theobald, K. Peter, J. O. Odden, and T. O. Saetre, Energy Procedia **27**, 21–26 (2012).
- ¹⁸R. N. Hall and J. H. Racette, J. Appl. Phys. **35**, 379 (1964).
- ¹⁹T. Heiser, A. A. Istratov, C. Flink, and E. R. Weber, Mater. Sci. Eng., B **58**, 149–154 (1999).
- ²⁰A. A. Istratov, C. Flink, H. Hieslmair, E. R. Weber, and T. Heiser, Phys. Rev. Lett. **81**, 1243–1246 (1998).
- ²¹D. Macdonald, J. Tan, and T. Trupke, J. Appl. Phys. **103**, 073710 (2008).
- ²²H. Savin, M. Yli-koski, A. Haarahiltunen, H. Talvitie, and J. Sinkkonen, ECS Trans. **11**(3), 319–329 (2007).
- ²³K. Bothe and J. Schmidt, Appl. Phys. Lett. **87**, 262108 (2005).
- ²⁴S. Koveshnikov, Y. Pan, and H. C. Mollenkopf, in *Proceedings of the Fourth International Symposium on High Purity Silicon* (1996), pp. 473–480.
- ²⁵M. Nakamura, S. Murakami, and H. Udon, J. Appl. Phys. **112**, 063530 (2012).
- ²⁶K. Shirai, H. Yamaguchi, A. Yanase, and H. Katayama-Yoshida, J. Phys.: Condens. Matter **21**, 064249 (2009).
- ²⁷S. K. Estreicher and A. Carvalho, Physica B **407**, 2967–2969 (2012).
- ²⁸S. K. Estreicher, Phys. Rev. B **60**, 5375–5382 (1999).
- ²⁹D. West and S. K. Estreicher, Phys. Rev. B **68**, 035210 (2003).
- ³⁰V. P. Markevich, A. R. Peaker, I. F. Medvedeva, V. E. Gusakov, L. I. Murin, and B. G. Svensson, Solid State Phenom. **131–133**, 363–368 (2008).
- ³¹C. Fahrland, Y. Ludwig, F. Kersten, and K. Petter, in *IEEE 40th Photovoltaic Specialist Conference (PVSC) (2014)*, pp. 135–139.
- ³²F. Fertig, K. Krauß, and S. Rein, Phys. Status Solidi RRL **9**(1), 41–46 (2015).
- ³³B. Sopori, P. Basnyat, S. Shet, and V. Mehta, IEEE Photovoltaic Specialists Conference, 2012.



ISBN 978-952-60-8041-3 (printed)
ISBN 978-952-60-8042-0 (pdf)
ISSN 1799-4934 (printed)
ISSN 1799-4942 (pdf)

Aalto University
School of Electrical Engineering
Department of Electronics and Nanoengineering
www.aalto.fi

**BUSINESS +
ECONOMY**

**ART +
DESIGN +
ARCHITECTURE**

**SCIENCE +
TECHNOLOGY**

CROSSOVER

**DOCTORAL
DISSERTATIONS**